

MODELING AND CONTROLLING THERMOCHEMICAL NANOLITHOGRAPHY

A Thesis
Presented to
The Academic Faculty

by

Keith M. Carroll

In Partial Fulfillment
of the Requirements for the Degree
Doctor of Philosophy in the
School of Physics

Georgia Institute of Technology
December 2013

Copyright © 2013 by Keith M. Carroll

MODELING AND CONTROLLING THERMOCHEMICAL NANOLITHOGRAPHY

Approved by:

Professor Jennifer E. Curtis,
Committee Chair
School of Physics
Georgia Institute of Technology

Professor Jennifer E. Curtis, Advisor
School of Physics
Georgia Institute of Technology

Professor Elisa Riedo
School of Physics
Georgia Institute of Technology

Professor Seth R. Marder
School of Chemistry and Biochemistry
Georgia Institute of Technology

Professor Lawrence A. Bottomley
School of Chemistry and Biochemistry
Georgia Institute of Technology

Professor Harold D. Kim
School of Physics
Georgia Institute of Technology

Date Approved: 4 October 2013

To my wife and family,

ACKNOWLEDGEMENTS

I want to start out by thanking my wife and my family. Marrying my wife is the best decision I ever made, and this is as much my work as it is hers. She put up with a lot of long nights only to prove how supportive and loving she is. She is my best friend, and I cannot even begin to imagine how my life would be without her. I want to thank my Mom and Dad; without their guidance and support I would not be where I am today. They have taught more than I can ever repay and I am eternally grateful. I want to thank Toni and Jerry for welcoming me into their family. I will never forget how wonderful and extraordinarily supportive they have been. I want to thank all my siblings. They were inspirations even when they did not know it. They kept me grounded the entire time, and they taught me what family means. They have blessed me with three wonderful nieces who always make me smile. Kevin, Kelly, Dave, Nichol, Jenny, Ryan, Juliana, Annie, thank you all. I want to thank the rest of my family as well; they have always been supportive. Thank you.

I want to thank my adviser, Professor Jennifer E. Curtis. Without her advice, I would not be half the researcher I am today. She taught me how to think about science but not forget the perspective of everything else. I also want to thank my fellow lab members (past and present): Vamsi, Louis, Mauricio, Dan, Patrick, Maitri, Karl, and Wenbin; without them, I do not know if I would have survived. I also want to thank our former Post-Doc Jan; his successes were always an encouragement.

I want to thank Professor Elisa Riedo and Professor Seth R. Marder. They were always happy and willing to discuss problems and possible solutions. They were an incredible source of advice, and I consider myself lucky to have worked so closely with them. I also want to thank my other committee members, Professor Lawrence

Bottomley and Professor Harold Kim. Your work and successes are an inspiration.

I want to thank Anthony, without whom much of this work would not have happened. He is a good friend who, as I have said before, is as smart as is his nice.

I also want to thank everyone from the Riedo lab (past and present); they have been an inspiration. In particular thank you to Debin, Deborah, Suenne, Lucy, Edoardo, Alex, and Gao.

Finally, I want to thank all my friends, who have been supportive. They have taught me what it means to be a loyal friend.

TABLE OF CONTENTS

DEDICATION	iii
ACKNOWLEDGEMENTS	iv
LIST OF TABLES	x
LIST OF FIGURES	xi
SUMMARY	xvii
I INTRODUCTION	1
1.1 Introduction	1
1.2 Lithographic Techniques	2
1.2.1 Microcontact Printing	2
1.2.2 Light Based Lithographies	4
1.2.3 Micro-Fluidics	5
1.2.4 Electron Beam Lithography	5
1.2.5 Nano-shaving/Nano-grafting	7
1.2.6 Electric and Conductive SPM techniques	8
1.2.7 Dip-Pen Nanolithography	9
1.2.8 Thermal or Thermomechanical Lithography	10
1.2.9 Thermal Dip-Pen Nanolithography	11
1.2.10 ThermoChemical Nanolithography	11
1.3 Chemical and Topographic Gradients	12
1.3.1 ThermoChemical Nanolithography: Evidence of Chemical Gradients	14
II CHEMICAL KINETICS MODEL	18
2.1 Introduction/Motivation	18
2.2 Chemical Kinetics Model	19
2.2.1 Static Tip Solution	21
2.2.2 Effects of Multiple Points	26

2.2.3	Extension to a Moving Tip	28
2.2.4	Effects of Speed on TCNL	29
2.3	Expanding to the Surface and 3-D	31
2.4	Discussion of the Assumed Temperature Profile	33
2.5	Final Word	34
III	CHEMICAL KINETICS MODEL	35
3.1	Introduction	35
3.2	Review of Thermal Cantilevers and Instrumentation	36
3.2.1	Thermal Cantilevers: Fabrication and Design	36
3.2.2	Electronic Properties	37
3.2.3	Instrumentation	38
3.3	ThermoChemical NanoLithography: Temperature Dependence	41
3.3.1	Methods and Description of Experiments	42
3.3.2	ThermoChemical NanoLithography: Speed Dependence	48
3.4	Controlling Chemical Reactions	50
3.4.1	Controlling Chemical Reactions with Temperature	50
3.4.2	Resolution Measurements	54
3.4.3	Controlling Chemical Reactions with Speed	56
3.4.4	Comparison of Temperature and Speed	59
3.5	Controls	59
3.6	Final Word	60
IV	EXTENSION OF TCNL TO 3D	62
4.1	Introduction	62
4.2	Simulations of Chemical Kinetics in 3-D	64
4.3	Conversion of PXT to PPV	71
4.3.1	Chemical Transformation and Properties of PPV	71
4.3.2	Film Preparation	72
4.4	Measurements of PXT/PPV Transformation	73

4.5	Using Topography to Demonstrate Extensions of TCNL	80
4.5.1	Nano-Scale Control	81
4.5.2	Z-Dependence	82
4.6	Final Word	87
V	PARALLELIZATION OF TCNL	89
5.1	Introduction	89
5.2	Description of Thermal Arrays	90
5.3	Leveling	91
5.3.1	Interaction between a Thermal Tip and a Substrate	91
5.3.2	Array Leveling	93
5.4	Thermal Patterning with Arrays	93
5.5	Thermal Imaging	96
5.5.1	Thermal Imaging with a Single Tip	97
5.5.2	Thermal Imaging with Arrays	98
5.6	Complications with Arrays	100
5.7	Final Word	100
VI	CONCLUSIONS AND FUTURE WORKS	101
6.1	Introduction	101
6.2	Review	101
6.3	Future Works and Improvements	102
6.3.1	Experiments to Verify Assumptions	104
6.4	Applications of Chemical Gradients	105
6.4.1	Surface Energy Gradients	105
6.4.2	Biophysical Applications	106
6.5	Applications of Topographic Gradients	107
6.5.1	Transfer PPV Patterns to PDMS	107
6.5.2	Colloidal Patterning	109
6.5.3	Nano-Fluidics	110

6.6 Final Word	110
APPENDIX A — DERIVATION OF EQUATION 4.13	111
REFERENCES	112
VITA	126

LIST OF TABLES

1.1	Comparison of Lithographic Techniques.	13
3.1	Computer Circuit Components	40

LIST OF FIGURES

1.2.1 (a) Schematic for μ CP. Reprinted with permission from [17] ©2000 John Wiley and Sons. (b) Example of DNA patterned with μ CP. Reprinted with permission from [18] ©2007 John Wiley and Sons. . .	3
1.2.2 (a) Schematic showing photo-activated chemical reactions in LAPAP. Reprinted with permission from [29] ©2003 American Chemical Society. (b) Example of a photo-chemical pattern (scale bar 500 μ m). Reprinted with permission from [30] ©2012 John Wiley and Sons. . .	4
1.2.3 (a) Schematic showing microfluidic setup to generate spatial gradients (b) and (c) Two examples of spatial gradients. Reprinted with permission from [31] ©2001 American Chemical Society.	6
1.2.4 (a) Schematic of nanoshaving. Reprinted with permission from [39] ©2008 American Chemical Society. (b) Example of bound nano-graft patterned DNA patterns. Reprinted with permission from [40] ©2002 American Chemical Society.	7
1.2.5 Schematic showing electro-conduction based lithography. Reprinted with permission from [42] ©2004 American Chemical Society.	8
1.2.6 (a) Schematic of DPN. Reprinted with permission from [45] ©1999 AAAS. (b) Example of DPN pattern made. Reprinted with permission from [50] ©2006 John Wiley and Sons.	9
1.2.7 (a) Schematic showing thermomechanical lithography. Reprinted with permission from [52] ©2002 IEEE. (b) Example of 3-D patterning. Reprinted with permission from [55] ©2010 AAAS.	10
1.2.8 Schematic of tDPN. Reprinted with permission from [63] ©2009 American Chemical Society.	11
1.3.1 Schematic of a thermal cantilever inducing a local temperature profile. The profile spread (a) laterally and (b) into the substrate.	14
1.3.2 (a) Experimental setup to verify the ability to create chemical gradients with TCNL. The left rectangle is written starting with a high temperature at the top and finishing with a low temperature at the bottom; the middle starts with a high temperature at the bottom and finishes with a low temperature on the top; the right rectangle is a superposition of the two. (b) Fluorophore labeled pattern corresponding to (a). (c) Plot of the intensity signal versus distance of the left rectangle. The direction is indicated by the arrow in (a). The change in the intensity signal is indicative that TCNL is capable of patterning chemical gradients.	16

2.2.1 Thermal reaction for the Cinnamate Polymer.	19
2.2.2 Time Dependence of equation 2.5 with equation 2.6.	23
2.2.3 Temperature Dependence of equation 2.5 with equation 2.6.	24
2.2.4 Decay length dependence of equation 2.5 with equation 2.6. The lines represent the extent of the chemical reaction, while the dots represent the decaying temperature profile.	25
2.2.5 Interaction between two contact points described in equation 2.10.	27
2.2.6 Plot of equation 2.13 with decay length of 100 nm.	29
2.2.7 Plot of equation 2.15 and higher order variants; the reference speed is 10 $\mu\text{m/s}$ and the reference transformation percentage is 0.99.	30
2.3.1 Schematic for equation 2.17.	32
2.3.2 Rastering image to pattern a substrate.	32
3.2.1 (a) Graph of thermal cantilever resistance versus power dissipated across the cantilever; 90% of the power is dissipated in the heater region. (b) Scanning Electron Microscope (SEM) image of a thermal cantilever. Image [104] reprinted with copyright permission © 2008 Taylor and Francis.	37
3.2.2 (a) Shown is an image of the Agilent 5600 LS series mounted with a thermal cantilever. (b) Shown is the nose cone adaptor used to mount the printed circuit board chip (PBC) shown in (c). (c) This is the PCB for mounting the thermal cantilever (mounted with a thermal cantilever). The silver paint connect the contacts to the legs of the thermal cantilever to complete the circuit. (d) This is one example of a circuit used to measure and compute all the electrical properties of the thermal cantilever according to Table 3.1.	39
3.3.1 Chemical structure of polymer.	41
3.3.2 (a) Typical experiment to test the chemical kinetics model. The numbers indicate typical dissipated powers for these experiments. (b) AFM image of the polymer substrate prior to patterning. (c) AFM image of the pattern detailed in (a).	43
3.3.3 Fluorescence image from the experiment shown in Figure 3.3.2. Scale bar is 5 μm	45
3.3.4 (a) Theoretical fluorescence image measured with an uneven illumination field. (b) Theoretical background image indicating the uneven illumination field. (c) Corrected fluorescence image resulting from dividing (a) by (b). The cyan square indicates an inscribed to measure a squares intensity level.	46

3.3.5 Comparison of the insets measured intensity (equation 3.2) (inset same as Figure 3.3.4) with the chemical kinetics model (equation 3.3). There is good agreement between the experiment and the model. The error bars represent the standard deviation from the measured intensity signal.	47
3.3.6 Comparison of the model with four different speeds (1 $\mu\text{m/s}$, 10 $\mu\text{m/s}$, 100 $\mu\text{m/s}$, 1 mm/s). The results show the curves shift to the right as predicted in chapter two.	48
3.3.7 (a) Experimental setup in which the temperature is fixed, but the speed is varied across 3 orders of magnitude. (b) Fluorophore labeled image corresponding to the experiment in (a). (c) Comparison of the measured fluorescence intensity to the chemical kinetics model with a fixed temperature and varying speed.	49
3.4.1 Schematic explaining how to create controlled chemical concentration profiles with TCNL. First, a calibration of the parameter E_a is combined with the intended pattern. This combination gives the peak temperature, T_{peak} , as function of position. Using methods described in the literature along with the measured eta, T_{peak} is translated into the spatial distribution of dissipated power. More details are provided in the text.	51
3.4.2 (a) User-defined concentration profile. (b) Map describing the power distribution as a function of position. This is obtained by following the procedures displayed in Figure 3.4.1. (c) Fluorescence image corresponding to the pattern defined in (a) and (b). (d) Plots comparing the user-defined (intended) concentration profiles against the experimentally measured values seen in (c).	52
3.4.3 (a) (Left) Original <i>Mona Lisa</i> image; (Right) $\approx 30 \times 40 \mu\text{m}^2$ reproduction of the <i>Mona Lisa</i> (commonly referred to as the <i>Mini Lisa</i>). (b) (Left) <i>Rose and Driftwood</i> , 1932, photograph by Ansel Adams, copyright 2012 The Ansel Adams Publishing Rights Trust. (Right) $44 \times 34 \mu\text{m}^2$ reproduction of <i>Rose and Driftwood</i> . Scale bars are 10 μm	53
3.4.4 (a) Friction measurement of consecutive TCNL patterned lines spaced by 125 nm. Cyan square indicates the average profile shown in (c); scale bar (red) is 1 μm . (b) FWHM measured with FFM for lines written at different powers. (c) Profile showing a smooth variation of the friction signal over a topographically flat area. The friction shows a measurable change over distance of 20 nm.	55
3.4.5 Experimental results showing controlled changes in chemical concentrations using variable speed. The plots indicate good agreement between the user-defined profiles and the experimentally measured values. Scale bar is 5 μm	57

3.4.6	Plots showing how errors can be amplified in equation 3.6. See text for details.	58
3.4.7	Comparison of fixed temperature versus fix speed designed patterns. (a) Fluorescence image with fixed temperature on the left and fixed speed on the right. The normalization factor is not shown. (b) Plots of the intensity signals versus intended (solid line).	59
4.2.1	(a) Simulation of the surface transformation for a decay length (λ) of 100 nm for four different speeds. Simulations at four different speed for the body transformation for three different z-decay lengths: (b) $\lambda = 50$ nm, (c) $\lambda = 100$ nm, (d) $\lambda = 25$ nm. The assumed film thickness is 50 nm.	66
4.2.2	Simulation showing that at larger z-decay lengths ($\lambda = 400$ nm), the body transformations temperature range starts to overlap with the surfaces transformation temperature range.	67
4.2.3	Simulation showing that at small z-decay lengths ($\lambda = 1$ nm), activation of individual layers can be observed.	69
4.2.4	(a) Simulations (circles) and fits (lines) of $k_{eff}(z)$ based on equation 4.6 and equation 4.11 for six different z-decay lengths ($\lambda = 25$ nm, 50 nm, 100 nm, 150 nm, 200 nm, and 500 nm). (b) Comparisons of the z-decay length (λ) to the effective decay length (κ) for the same six λ decay lengths in (a). Inset shows how this ratio change for a fix λ of 100 nm and variable T_{peak}	70
4.3.1	(a) Chemical transformation of PXT to PPV. (b) Excitation (solid line) and Emission (dashed line) of PPV.	71
4.3.2	(a) Raman measurements indicated an increase in the 1180 cm^{-1} and 1600 cm^{-1} peaks; this indicates the transformation from PXT to PPV. (b) Fluorescence image of PPV patterns before Raman measurements. (c) Fluorescence image of the same PPV pattern after Raman measurement. The circled region indicates the invasive nature of the Raman probing laser.	73
4.4.1	(a) Experimental schematic for the measuring the change in the photoluminescence signal with changing heater temperature. Red squares indicate patterns written at $1\ \mu\text{m/s}$, while blue squares are at $10\ \mu\text{m/s}$. (b) Photoluminescent image of the pattern corresponding to the experiment in (a). (c) Semi-quantitative measurements of the signals in (b). (d) Zoomed in version of Figure 4.2.1 (d) to indicate that the at low peak temperatures, the data forms agree. ($\lambda = 25$ nm, film thickness = 50 nm).	75

4.4.2 (a) Friction measurement for a series of squares written at heater temperatures of $\approx 150^\circ\text{C}$ up to $\approx 550^\circ\text{C}$. (b) Plots of the friction signal versus heater temperature seen in (a). Above 400°C the friction signal is seen to level off; this is indicative the surface transformation has completely taken place. (c) Plot of the fluorescence signal for the pattern in (a). The signal continues to increase pass the 400°C heater temperature; this suggests the body has not undergone the complete transformation, while the surface has.	77
4.4.3 (a) AFM measurements of squares patterned into PPV. The heater temperature range is $T_1 \approx 160^\circ\text{C}$ (lower right) up to $T_{25} \approx 550^\circ\text{C}$ (upper left). (b) Fluorescence signal of the pattern in (a). (c) Comparison of the change in PPV height (depth) (a) versus the intensity signal in (b). The two are approximately linear.	79
4.5.1 (a) Spatial distribution of applied voltage to create a $30\ \mu\text{m} \times 40\ \mu\text{m}$ reproduction of the <i>Mona Lisa</i> . (b) Fluorescence image of the patterned PPV. (c) AFM image of the patterned PXT/PPV film. Diffraction in (b) limits our ability to see the added details. (d) FFM measurements that qualitatively detail the reproduction.	83
4.5.2 (a) AFM image showing $\approx 20\ \mu\text{m} \times 33\ \mu\text{m}$ reproduction of the <i>Mona Lisa</i> in PXT/PPV film (<i>Mona Lisa 2.0</i>). (b) Fluorescence image corresponding to the pattern in (a). Diffraction makes the image look blurry as compared with the high resolution AFM image.	84
4.5.3 Measurements of FWHM of lines made in PXT/PPV film (a) AFM image of lines at different temperatures. (b) Measurements of the FWHM as a function of power and heater temperature.	84
4.5.4 (a) Schematic showing an experiment in which the heater temperature is kept constant and the speed is varied as a function of position. (b) AFM image corresponding to the experiment in (a). (c) Plot of the fluorescence signal of the PXT/PPV pattern. (d) Fit of equation 4.13 with experimental results in (b). The measured effective decay length is ≈ 3.0 ; we approximate the temperature decay length as $\approx 40\ \text{nm}$	86
5.2.1 (a) Optical image of thermal cantilever array with numbering. (b) Schematic showing a thermal cantilever array inducing a temperature profile in a substrate.	91
5.3.1 (a) Resistance measurement as a thermal tip is brought into contact with a surface; also shown in blue is the optical measured force displacement curve. (b) and (c) Schematics showing that at far distance from a substrate (a) the thermal cantilever transfers less heat than close to the surface (b).	92

5.3.2	Resistance measurements of individual cantilevers in an array versus distance. (a) Measurement and schematic showing misalignment between the thermal cantilever array and the substrate. (b) Measurement and schematic showing all five tips in contact with the substrate near simultaneously after indicated correction made (a).	94
5.4.1	Thermal patterning in a PPV-precursor film made with thermal cantilever array. (a) Raman measurements indicating the transformation from precursor to PPV. (b) Fluorescence image of pentagon PPV patterns made with thermal array. (c) Zoom-in version of patterns from (b).	95
5.4.2	Measurements of lines made in PPV-precursor film made with thermal cantilever array (a) Fluorescence image of patterns of lines made with thermal cantilever array. (b) AFM image of patterns imaged in (a). (c) Topography profile for Tip 1 (indicated in blue in (a)), inset indicates a resolution of about 68 nm.	96
5.5.1	(a) Thermal imaging of a z-calibration grating with a single tip (b) AFM image of the same area measured in (a).	98
5.5.2	Thermal image obtained from a z-calibration grating with a thermal cantilever array.	99
6.5.1	Schematic showing transfer of PPV topographic pattern to PDMS.	108
6.5.2	Experimental evidence showing the transfer of (a) PXT/PPV topographic patterns to (b) PDMS.	109

SUMMARY

This thesis presents and develops a systematic approach to ThermoChemical NanoLithography (TCNL). TCNL is a scanning probe microscope based lithographic technique which uses a localized temperature profile to induce chemical transformations. The intent of this work is to extend our understanding of TCNL to be able to model and control chemical reactions taking place at the nano-scale.

This work is broken up into four parts. The first part adapts a chemical kinetics model to predict and explain some of TCNLs features. By looking at different parameters, we gain insight into how TCNL can be used to control surface chemical reactions. The second part of this work focuses on studying only surface reactions. As part of this, we use fluorescent microscopy to quantify the chemical transformation, and after successfully verifying the adapted chemical kinetics model, we apply the model to control the chemical transformation process and demonstrate excellent precision down to the sub-micron length scales.

Having verified the chemical kinetics model for surface reactions, this thesis focuses on extending the model beyond surface effects and studying the penetration of the reaction into the substrate. We also develop analysis for using other TCNL induced material property changes to measure different aspects of the substrates chemical transformation. Finally, the last part of this work focuses on parallelization of TCNL. We demonstrate nano-scale resolution can be extended to multiple tips simultaneously.

CHAPTER I

INTRODUCTION

1.1 Introduction

Micro and nano-lithographic techniques are extraordinarily important to everyday life and in many research fields. Lithographic techniques make possible circuits for computer and microchips [1], the parallelization of medical diagnostics [2], and the control of interactions between materials and the environment [3, 4]. With much research trending towards nanotechnology [5], nano-lithographic techniques are becoming particularly important; nano-lithographic techniques have been used to introduced band gaps in graphene nano-ribbons [6] and for the development of protein nano-arrays [7]. A fundamental challenge to these micro and nano-scale applications is the need to strategically and intentionally position molecules in an organized fashion.

For the most part, lithographic techniques have been developed to meet a particular requirement; soft lithography, for example, was developed as an alternative to photolithography for a variety of different materials and surfaces [8]. While many techniques have been developed, one characteristic lacking in many lithographic techniques is the ability to control the local concentration levels of different molecules or chemistries. Succinctly, many researchers aim for lithographic techniques to be binary in nature. There already exist many research fields which would benefit from a systematic technique which can control surface concentrations. For example, controlled variations in concentration (hereto referred as gradients) of the protein laminin have directed axonal growth [9, 10]; chemical gradients have also induced droplet motion against gravity because of the controlled variations in surface energy [11, 12]. By changing a surfaces topography, researchers have altered how a surface interacts with

the environment; in particular, increasing surface roughness induces a transition from hydrophobic to super-hydrophobic regimes on some materials [3, 13]. Electronic heat sinks are often designed with corrugated ridges to allow for more cooling from the increased surface area [14].

Surface design is essential to many nano and micro-scale applications because they control the foundations and in some case the intrinsic properties of devices. Lithographic techniques are used to alter both topography and chemistry [2, 15, 16]. Lacking, however, is a technique capable of controlling these variations (hereto referred as chemical and topographic gradients) down to the nano-scale. The focus of this thesis is to overcome these limitations using the promising technique Thermo-Chemical Nanolithography. In the rest of this chapter, many state of the art lithographic techniques are reviewed, and the focus is on their advantages, disadvantages, and limitations as they relate to gradient patterning. The chapter concludes with an overview of TCNL's potential to create chemical gradients, and finally an outline is provided to show how to go about doing this in the remainder of this thesis.

1.2 Lithographic Techniques

1.2.1 Microcontact Printing

Microcontact printing (μ CP) is a lithographic technique which uses a stamp to pattern areas [8]. Usually the stamp is formed out of an elastomeric material, such as Polydimethyl siloxane (PDMS) [17]; the standard procedures are shown in Figure 1.2.1, where first a mold is filled with un-cured elastomeric material. The uncured polymer fills the mold, and after the stamp is cured and released, the mold imprint remains in the solid elastomer. After incubating the stamp with chemical materials, such as proteins, DNA, or organic molecules, the stamp transfers the materials to a target surface. The key advantage to μ CP is the high-speed and high-throughput patterning [8]; there is also a vast amount of literature on the diverse materials that have been

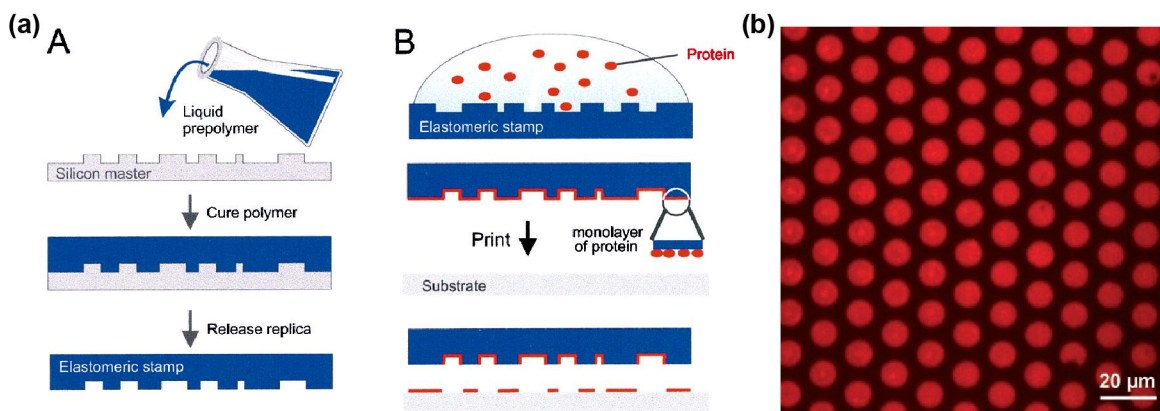


Figure 1.2.1: (a) Schematic for μ CP. Reprinted with permission from [17] ©2000 John Wiley and Sons. (b) Example of DNA patterned with μ CP. Reprinted with permission from [18] ©2007 John Wiley and Sons.

transferred [18, 19, 20, 21], as well as the number of substrates with which this technique has been used. One of the disadvantages is that micro-contact printing requires new molds and new stamps whenever different pattern sizes and shapes are needed.

Typically, this technique is used for micro-scale patterning, but there are modifications, such as using elastomeric materials with higher elastic coefficients [22, 23], allowing for 100 nm scale devices to be printed. The later is sometimes referred to as nano-contact printing.

For the most part, the technique is binary; however, there has been some research dedicated to making chemical gradients by using stamps with variable thickness [24]. These specialized stamps are infused with a chemical molecule (such as an alkanethiol). When the stamp is brought into contact with a surface (for example gold), molecules at the stamp-substrate interface covalently attach to the surface. As time elapses, the molecules in the stamp diffuse and attach to the substrate, and a chemical gradient forms analogous to the stamps variable thickness. Results with alkanethiols have shown variable chemical concentrations over distances of ≈ 10 mm, but given the ratios between the length and heights, it would be difficult to extend this technique down to the micro-scales.

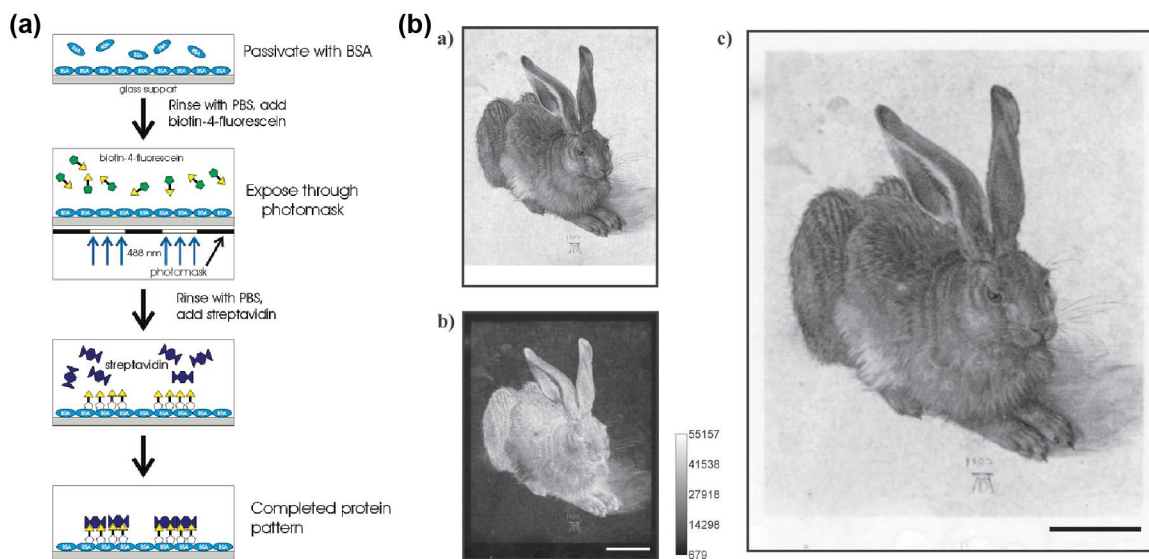


Figure 1.2.2: (a) Schematic showing photo-activated chemical reactions in LAPAP. Reprinted with permission from [29] ©2003 American Chemical Society. (b) Example of a photo-chemical pattern (scale bar 500 μm). Reprinted with permission from [30] ©2012 John Wiley and Sons.

1.2.2 Light Based Lithographies

Light based lithographies are omnipresent throughout research and industrial applications [25]. Briefly, they are any set of techniques which use light as a means to pattern a substrate; the patterning comes in different forms such as cross-linking photo-resists and inducing radical states to induce a chemical reaction. Photolithographic techniques are generally robust, fast, and easy to do on large scales, hence their ubiquity particularly in semi-conducting industries. Typically, they employ positive or negative resists to protect patterned areas from wet and dry etch based techniques. Despite being diffraction limited, resist based photolithographies have achieved nanometer scales by employing materials with high indices of refraction and two photon dependent materials to narrow the diffraction limit [26, 27].

Other light based techniques are also available. Of particular note is a technique known as laser-assisted adsorption by photobleaching (LAPAP) [9, 28], which uses light to induce radical excited states which react with surface bound molecules [29]

(see Figure 1.2.2a). This technique has demonstrated an impressive ability to pattern chemical gradients such as those seen in Figure 1.2.2b. The technique is relatively easy to implement, but is limited by a combination of diffusion and the diffraction limit down to about a micron. The ability to introduce spatial light modulators and digitally controlled micro-mirror devices makes this technique attractive for high speed pattern production [30].

1.2.3 Micro-Fluidics

Micro-fluidic devices are used as a viable lithographic technique with the ability to create chemical gradients. Usually micro-fluidic patterning is used to create spatial gradients [31], but the technique has been applied to produce surface gradients [10]. Different concentrations of intended molecules are flown through different connected configurations of Y shaped fluid devices, such as those shown in Figure 1.2.3a, to create controlled spatial chemical concentrations, such as those seen in Figure 1.2.3b,c. The diverse forms made, however, are on several hundred microns to millimeters wide, and the technique is limited in its ability to fabricate complex patterns since only 1-D patterns are currently available rather than 2-D.

1.2.4 Electron Beam Lithography

Though primarily developed for the semi-conducting industry [2], electron beam lithography (E-beam) has also been used to pattern substrates [32, 33] and is well known for its high resolution from the focused electron beam. The resolution is not determined by the electron beam, but rather by the interaction of the electrons with the material [2, 34]. Materials that scatter electrons more tend to have lower resolutions. Generally the resolutions are sub-100 nm, and in some cases have been shown to go down to 5-10nm [35, 36]. Typically for nano-patterning, E-beam will use different forms of electron sensitive resists and uses techniques similar to photolithography to pattern areas [37, 38]. The disadvantage is the time, expense, and the high vacuum

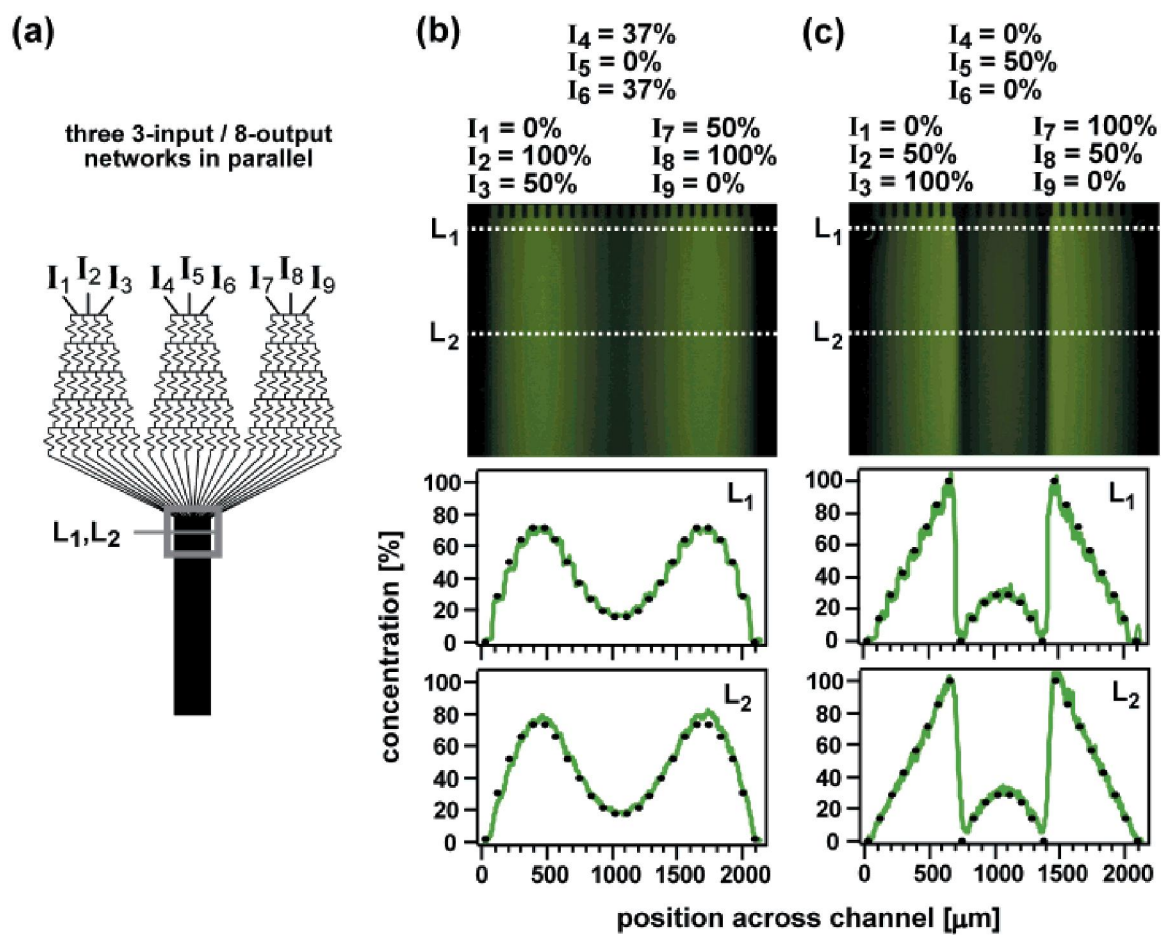


Figure 1.2.3: (a) Schematic showing microfluidic setup to generate spatial gradients (b) and (c) Two examples of spatial gradients. Reprinted with permission from [31] ©2001 American Chemical Society.

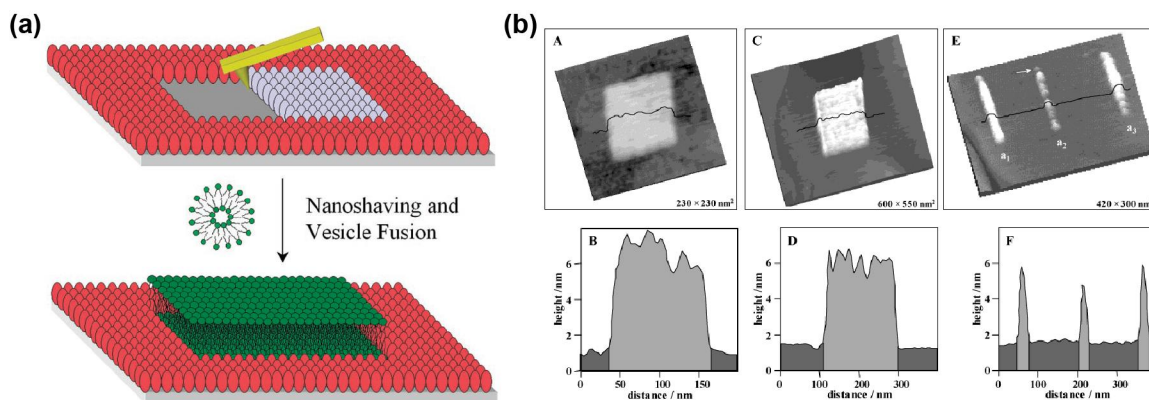


Figure 1.2.4: (a) Schematic of nanoshaving. Reprinted with permission from [39] ©2008 American Chemical Society. (b) Example of bound nano-graft patterned DNA patterns. Reprinted with permission from [40] ©2002 American Chemical Society.

associated with e-beam [35].

1.2.5 Nano-shaving/Nano-grafting

Nano-grafting and nano-shaving are similar techniques, which use a stiff AFM cantilever to scratch molecules off a surface, which is usually a self assembled monolayer (SAM) [39, 40]. Figure 1.2.4a shows a schematic and example. With the plowed area now exposing a different chemistry than the unscathed area, different molecule types can be site-specifically attached. An example is shown in Figure 1.2.4b. This technique can be performed in a solution containing the secondary molecule (nano-grafting), or else molecules are attached serial to patterning (nano-shaving). The resolution varies slightly from about 100 nm to 5-10 nm depending on the radius of curvature of the tip and the interactions between the tip and surface [35, 40].

Both processes are rather aggressive in nature, and usually require a large loading force to chemically break bonds and remove molecules from the surface. One of the advantages to this technique is that because the removal force is so large, the same probe can image the sample with a lower contact load (or even in AC mode).

Other forms of this technique have used oscillating AFM tips to remove molecules

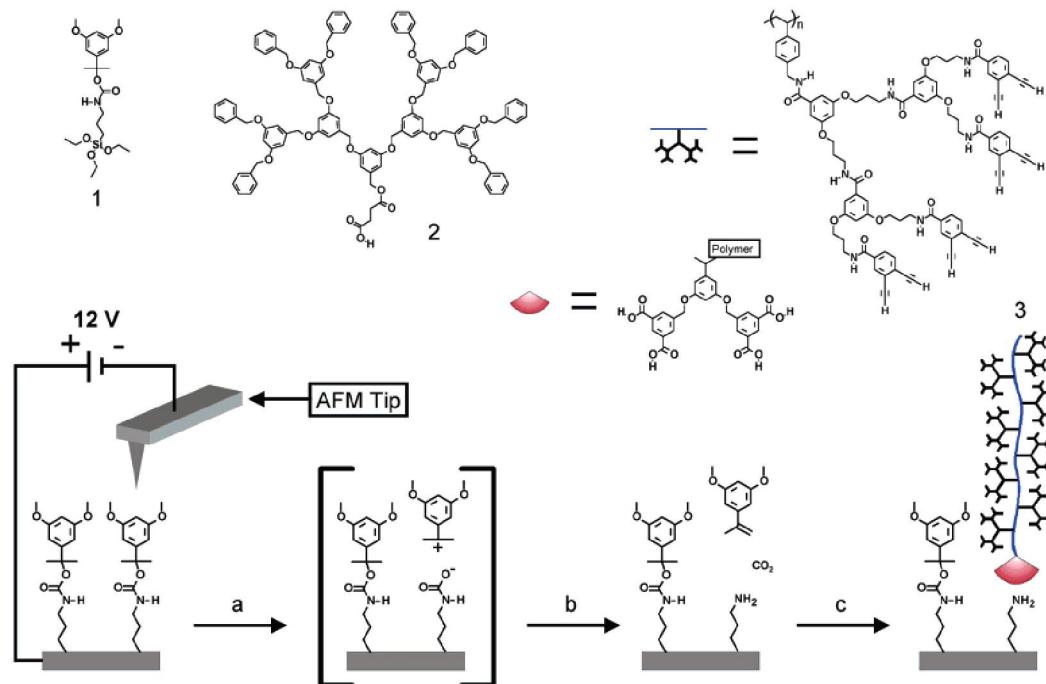


Figure 1.2.5: Schematic showing electro-conduction based lithography. Reprinted with permission from [42] ©2004 American Chemical Society.

from a surface [41]. By using actuated tips, different flexure modes can write or re-write patterned areas. This particular adaptation has been shown to have resolutions down to 50 nm.

1.2.6 Electric and Conductive SPM techniques

Some SPM based techniques use localized electric fields and currents to pattern substrates with a conductive SPM probe. Electro-chemical techniques induce redox reactions on a substrate to introduce chemically varying substrates such as those seen in Figure 1.2.5 [42, 43]. A similar technique [44] has demonstrated chemical gradients, but the speed (≈ 50 nm/s) associated with this particular application is fairly slow. In general electro-chemical techniques are slow (≈ 10 $\mu\text{m/s}$), and the resolutions are on the order of 25 nm.

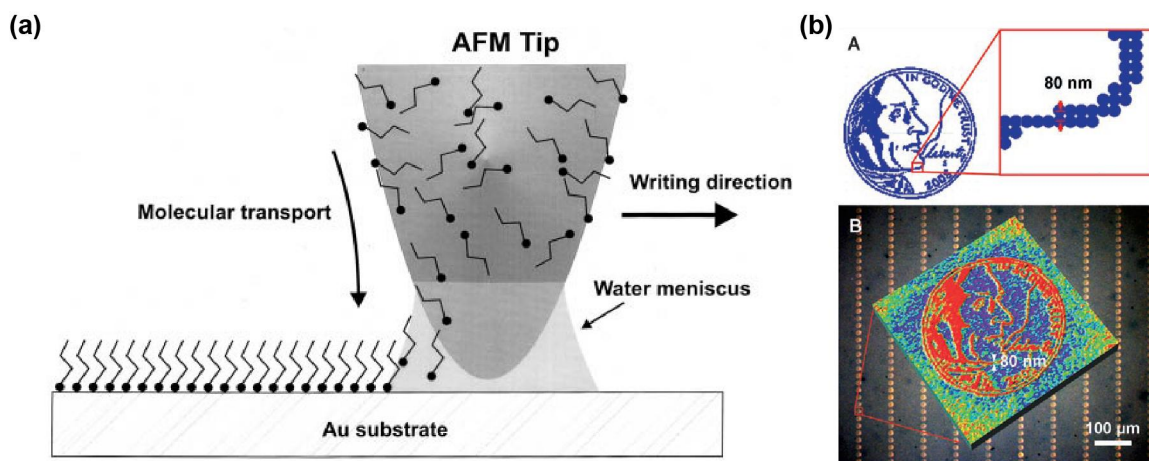


Figure 1.2.6: (a) Schematic of DPN. Reprinted with permission from [45] ©1999 AAAS. (b) Example of DPN pattern made. Reprinted with permission from [50] ©2006 John Wiley and Sons.

1.2.7 Dip-Pen Nanolithography

Dip-Pen Nanolithography (DPN) is another SPM based technique, which uses an inked AFM tip to pattern dissolved ink molecules [45] (see Figure 1.2.6a). Typically to insure that the ink stays on the tip, the SPM probe needs to be chemically modified. A number of molecules, such as proteins, DNA, and organic molecules, have been patterned on a variety of surfaces [16, 46, 47]; however, sometimes different molecules require the AFM tip to have different chemical modifications [48]. While the technique has been shown to achieve down to 10 nm [49], typical resolutions are sub-100 nm [45]. The technique is limited by fluid transport rates and as a result it is a fairly slow SPM lithography (typical speeds are $\approx 1 \mu\text{m/s}$ or slower). There has been some focus on expediting the process by introducing multiple cantilever to pattern the surface simultaneously. An example of this parallelization is shown in Figure 1.2.6b, where an outline of a dime is replicated thousands of times [50]. By increasing dwell time ($> 1 \text{ min}$), different spot sizes can be reliably reproduced. One of the disadvantages to DPN is the inability to image the patterned areas without replacing the SPM tip; moreover, tip-surface contact needs to be broken in between patterned areas.

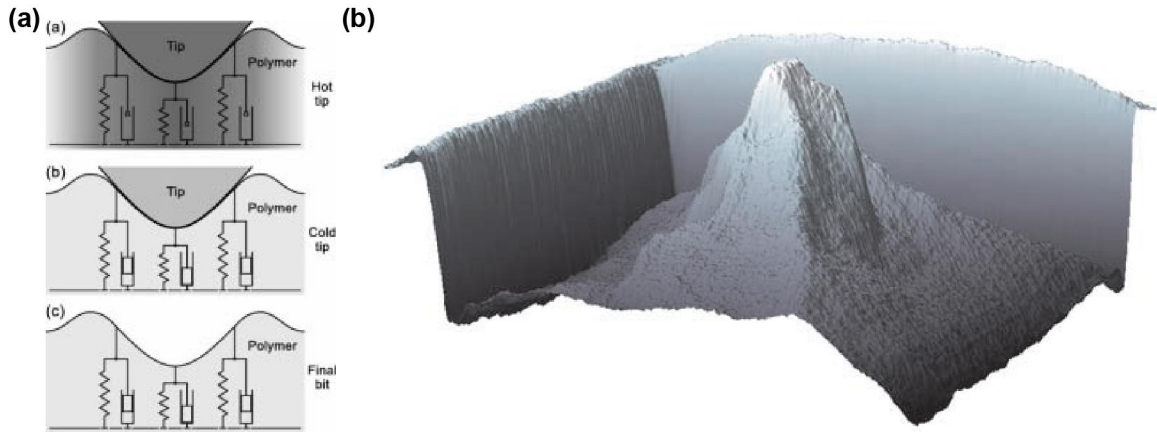


Figure 1.2.7: (a) Schematic showing thermomechanical lithography. Reprinted with permission from [52] ©2002 IEEE. (b) Example of 3-D patterning. Reprinted with permission from [55] ©2010 AAAS.

1.2.8 Thermal or Thermomechanical Lithography

Thermomechanical lithography tries to introduce indents into a substrate with a semi-conducting thermal cantilever. Thermal cantilevers are designed so that if biased with a voltage, the heat generated from the dissipated power raises the cantilevers temperature to several hundred degrees [51]. When brought into contact with a polymer substrate and heated, an indentation can form if the temperature exceeds the glass transition temperature (thermo) and a large enough load is applied (mechanical) [52]; this process is shown in Figure 1.2.7a. Different loading forces and temperatures change the interaction and the resolution [53].

Though initially the focus was on finding a new medium to increase data storage [54], the technique has grown to include patterning resists with extraordinary resolution (≈ 10 nm) and extraordinary detail, such as the 3-D reproduction of Mount Matterhorn [55] (Figure 1.2.7b). Thermal techniques can usually be run at high speeds (≈ 1 -10 mm/s) [56]. One of the main drawbacks to any thermal and thermomechanical lithography is the fact that the thermal tips are easily contaminated [57, 58, 59]. There are several ways around this such as using diamond coated tips [60] and using a modified version of thermal lithography [56].

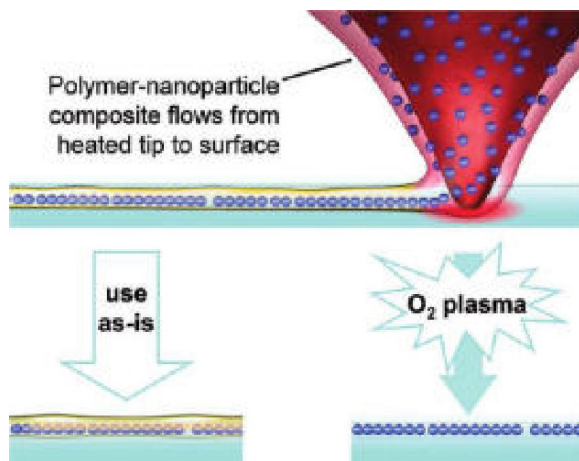


Figure 1.2.8: Schematic of tDPN. Reprinted with permission from [63] ©2009 American Chemical Society.

1.2.9 Thermal Dip-Pen Nanolithography

Thermal Dip-Pen Nanolithography (tDPN) combines thermal cantilevers with DPN; by coating a thermal cantilever with a solid ink, the thermal cantilever can be heated to melt the solid ink (thermal) and subsequently write the liquid ink (DPN) [61]. Cooling the tip solidifies the ink and this ability removes the continuous contact issue associated with DPN; however, one disadvantage is that depending on the substrate properties, the cooling can take several minutes [62]. The technique has been shown to achieve resolutions down to ≈ 100 nm. If the ink is doped with nano-particles, the capillary forces result in nano-particle alignment as seen in Figure 1.2.8 [63].

1.2.10 ThermoChemical Nanolithography

ThermoChemical Nanolithography (TCNL) uses a localized temperature profile to induce chemical transformation on a substrate. The technique has been used to functionalize substrates to attach proteins or convert to other functional groups [64], reduction of graphene oxide [65], reduction of graphene fluoride to grapheme [66], crystallization of ceramic materials [67], changing hydrophobic materials to hydrophilic [68, 69], and for the transformation of a precursor film into a semi-conducting organic

polymer [70]. Other variants of the technique include using thermal cantilevers to induce retro-Diels-Alder [71] reactions and desorption/depolymerization [56, 72] of organic polymer films; these variants introduce changes to the surfaces topographic structure. While typically TCNL employs the thermal cantilevers previously discussed, other forms have used small wires to produce the same effect [59]. The resolution is substrate dependent, but ranges from ≈ 10 nm up to ≈ 100 nm. Researchers have shown that TCNL can be done at high speeds (≈ 1 mm/s) [64, 68]. Since TCNL is based on temperature dependent phenomenon, it is possible to control the relative amount of chemical transformation taking place by tuning the temperature [58].

All of the mentioned lithographic techniques are summarized in Table 1.1; the resolutions, some advantages and disadvantages are listed there as well. Though only a few are reviewed here, there are vast numbers of lithographic techniques [73, 74, 75, 76, 77, 78, 79, 80, 81].

1.3 Chemical and Topographic Gradients

While there is no direct answer or evidence as to which technique is the best, certain standards have been suggested [2, 82]. In practice, the best technique is the one that fits an applications needs. For example, nano-scale studies would probably avoid light based techniques, and focus more on a SPM based lithography or E-beam.

The challenge proposed in the introduction was to develop a technique capable of creating controlled chemical and topographic gradients on the nano-scale to the micro-scale. The only lithographic technique which has shown promise to design and control a surfaces chemical and topographic morphology across these scales is ThermoChemical NanoLithography. There exists some preliminary evidence to suggest that TCNL can fabricate chemical gradients [64, 70], but until recently [58], a systematic approach was lacking. The next section gives direct experimental evidence to prove that TCNL is capable of creating chemical gradients; surface topographic

Table 1.1: Comparison of Lithographic Techniques.

Technique	Advantage	Disadvantage	Resolution
μ CP	Fast, Parallel	Rigid	≈ 100 nm-1 μ m
Photolithography	Fast, Parallel, Tunable	Diffraction Limited	≈ 10 nm-1 μ m
μ Fluidics	Fast, Parallel	Rigid	≈ 1 mm
E-Beam	High Resolution	Cost, Time, Vacuum	≈ 5 nm
Nano-shaving/ Nano-grafting	High Resolution	Aggressive Technique	5-100 nm
Electric and Conductive SPM Techniques	High Resolution	Slow	25 nm
DPN	High Resolution	Slow	10 nm
Thermal Lithography	High Resolution, Speed	Tip Contamination	10 nm
tDPN	Write/Read Capabilities	Slow	100 nm
TCNL	High Resolution, Speed	Tip Contamination	≈ 10 -100 nm

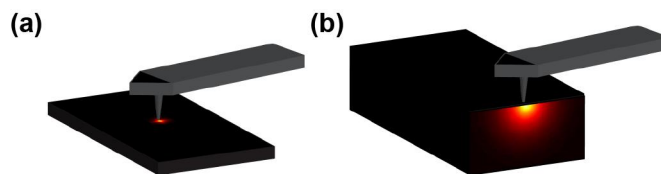


Figure 1.3.1: Schematic of a thermal cantilever inducing a local temperature profile. The profile spread (a) laterally and (b) into the substrate.

gradients will be left to a later chapter.

1.3.1 ThermoChemical Nanolithography: Evidence of Chemical Gradients

As previously described, TCNL is a lithographic technique which uses a thermal cantilever to induce chemical transformations at a surface. The details of these thermal cantilevers are reviewed in chapter three, but their most important feature is the ability to locally heat across several hundred degrees [51]. When brought into contact with a substrate, a heated cantilever induces a temperature profile in the substrate as depicted in Figure 1.3.1a,b. The input of thermal energy causes a thermally driven chemical reaction.

Although this technique has been used for a number of material substrates, the ability to create continuous chemical gradients is demonstrated on a thermally activated polymer substrate. The polymer poly((tetrahydropyran-2-yl N-(2-methacryloxyethyl) carbamate)-co-(methyl 4-(3-methacryloxypropoxy)cinnamate)), has a protected functional amine group.¹ When heated, the protection group dissociates from the surface, leaving an exposed reactive amine to which molecules with complimentary chemistries can be site-specifically bound. Proteins, DNA, and other biomolecules have been attached to these localized amine areas [64]. These amines have also been chemically transformed into other functional groups such as carboxyl or maleimides [64]. To test the ability to create gradients on this polymer substrate,

¹Synthesized by Professor Seth R. Marders lab at Georgia Institute of Technology.

a thermal cantilever is brought into contact with this polymer substrate and the cantilevers temperature is controlled as a function of position, such as the experiment shown in Figure 1.3.2. After patterning, the sample is chemically modified by attaching a fluorescent dye to the exposed amines. Areas with greater concentrations of amines result in a greater amount of fluorescent dye binding. The bright fluorescence signal seen in Figure 1.3.2 at the high temperature areas corresponds to more bound amines, while the dimmer signal results from the low temperature areas. This pattern provides evidence that TCNL can make chemical gradients, but without a systematic study, the need to control and extend this process to other materials and substrates remains unanswered.

The goal of this thesis is to develop a systematic approach to create and design controlled chemical gradients with TCNL. While so far, we have only discussed preliminary evidence with chemical gradients, we exploit TCNL to create topographic gradients with precisions down to the nano-scale. A chemical kinetics model is employed to predict the transformation taking place at a substrate. Once an approach has been established, systematic protocols will be developed to produce desired chemical gradients and topographic gradients. Finally with the goal of making the technique high throughput and fast, some of this work will be dedicated to discussing parallelization of TCNL using arrays of thermal cantilevers. The long term impact of this work is ability to generalize the methods and techniques discussed to apply to other materials and substrates.

The remainder of this study is broken down into four parts over the next five chapters. Chapter two reviews and discusses the first part of this thesis about coupling chemical kinetics with TCNL. Chapter three experimentally verifies the results derived in chapter two, and applies these results to controllably varying chemical concentrations (part two of this thesis). While chapter three focuses on surface effects, chapter four shifts this focus to how the chemical kinetics penetrates into the sample

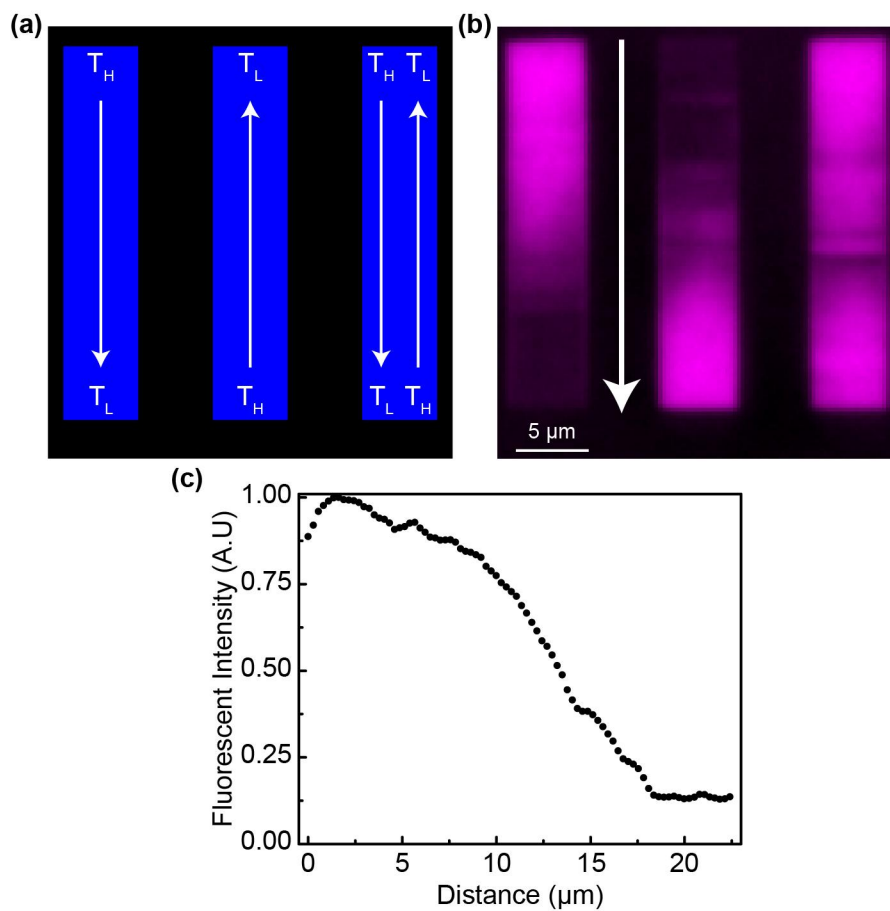


Figure 1.3.2: (a) Experimental setup to verify the ability to create chemical gradients with TCNL. The left rectangle is written starting with a high temperature at the top and finishing with a low temperature at the bottom; the middle starts with a high temperature at the bottom and finishes with a low temperature on the top; the right rectangle is a superposition of the two. (b) Fluorophore labeled pattern corresponding to (a). (c) Plot of the intensity signal versus distance of the left rectangle. The direction is indicated by the arrow in (a). The change in the intensity signal is indicative that TCNL is capable of patterning chemical gradients.

(part three). Chapter five discusses parallelization (part four), and finally chapter six concludes with a discussion of areas of ongoing research and possible applications for the works developed in this work.

CHAPTER II

CHEMICAL KINETICS MODEL

2.1 Introduction/Motivation

Modern fabrication processes have paved the way for advancements in technology and in research. These advancements have been particularly apparent in semi-conducting and electronic device manufacturing and miniaturization. Prevalent among the fabrication methods are photolithographic techniques, which as the name suggests uses light (photo) to crosslink photo-resists site-specifically (lithography) [26, 83]. Since photolithography is light based, it is diffraction limited, but interestingly, this limitation has not prevented fabrication engineers from extending photolithography to nano-scale sized devices [84]. It is not so much that these scientists and engineers have broken the laws of optics, but rather have used the laws to their advantage. For example, in photolithography, material scientists have developed high-dielectric materials to allow fabrication engineers to tune the diffraction limit to meet their needs [27]. The added value of high dielectric constants comes from understanding and deriving the limitations from the wave theory of light. Other improvements, such as studying which materials enhance two photon-absorption, have aided in micromachining 3-D objects with light [85]. Much as wave theory provided the fundamental principles to allow researchers and engineers to push the limits of photo-patterning to near any size [86], it stands to reason that any technique will be open to substantial improvement once the fundamental principles have been derived and validated. Using this as motivation, this chapter is dedicated to writing and deriving the principles governing ThermoChemical Nanolithography (TCNL). Our goal is to develop a novel approach for patterning controlled chemical concentrations with high resolution.

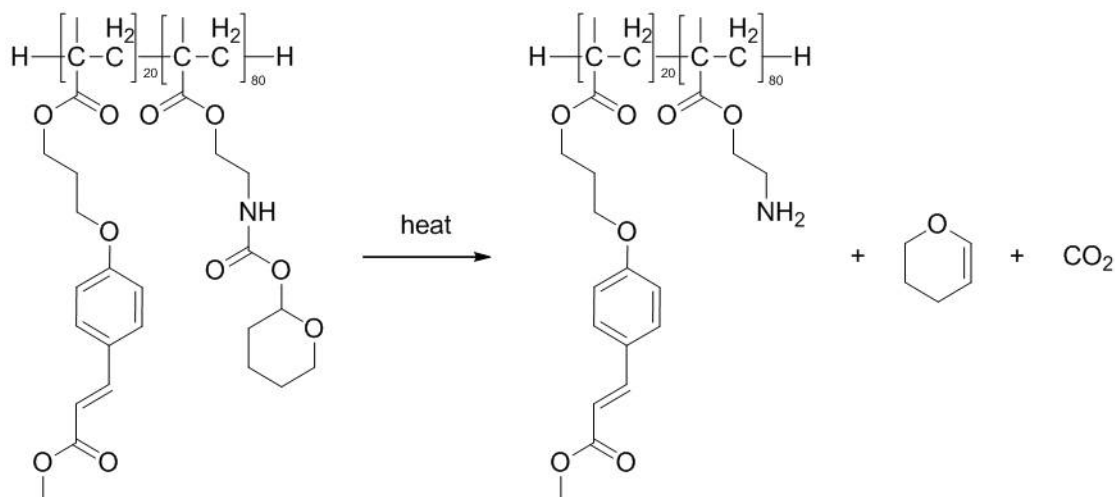


Figure 2.2.1: Thermal reaction for the Cinnamate Polymer.

2.2 Chemical Kinetics Model

Understanding that TCNL induces a localized chemical transformation at a substrate, it is reasonable to view this technique through the lens of chemical kinetics because chemical kinetics will provide the fundamental governing equations for TCNL. While TCNL has been performed on a multitude of substrates, we focus on a model surface, which will be used to measure a relative chemical concentration with the help of fluorescence microscopy as explained in chapter three. Our choice for this study is a spin casted organic polymer film (poly((tetrahydropyran-2-yl N-(2-methacryloxyethyl)carbamate)-co-(methyl 4-(3-methacryloyloxypropoxy)cinnamate))); the synthesis and surface preparation protocols are well described elsewhere [58, 64]. The polymer and polymer substrate were synthesized in Professor Seth R. Marder's lab at Georgia Institute of Technology. Briefly, it has been synthesized to have a protected functional group, and when thermally activated, the protection group dissociates and leaves behind an exposed functional group on the polymer. The reaction is shown in Figure 2.2.1, where the left hand side shows the protected polymer and the right hand side shows the thermally activated deprotected polymer with exposed, reactive amines [64].

This transformation from the protected, nonfunctional group to an exposed, active functional amine is described as a chemical reaction:



where R is the reactant, the protected polymer, and P is the final product, the deprotected polymer. Based on the likely deprotection mechanisms [64], the assumption is that this reaction should act similarly to a first order chemical kinetics reaction. The rate equation for this polymer goes as:

$$\frac{d[P]}{dt} = k[R] = k([P_{tot}] - [P]) \tag{2.2}$$

where $[P]$ is the product concentration, $[R]$ is the reactant concentration, $[P_{tot}]$ is the maximal product concentration (in this case the maximal density of deprotected amines), and k is the reaction rate. The reaction rate, k , is defined using the Arrhenius formula:

$$k = A \cdot e^{\frac{-E_a}{R \cdot T}} \tag{2.3}$$

where A is the temperature independent Arrhenius constant, E_a is the activation energy, R is the gas constant, and T is the temperature. Chemically, E_a is the energy barrier to cause the chemical transformation; more specifically, the activation energy has been associated with the energy difference between the reactant and an intermediate species [87, 88]. A represents the maximal rate of reaction. The literature suggests that there are other variants, such as the Arrhenius coefficient having a $T^{\frac{1}{2}}$ dependence [89]. Often, these other forms for A are intended for bimolecular reactions [90], collision based reactions [87], or reactions spanning a large temperature range [89]. Moreover, for narrow temperature range consistent with this work, there are very minor differences in the final values, and simulations, in which temperature dependent Arrhenius values were used, show negligible differences. It suffices for the intent of this work to use a temperature independent Arrhenius constant. The

values for E_a and A come from thermogravimetric analysis (TGA)¹ and are given by 134 ± 32 kJ/mol [58] and $1.7 \cdot 10^{16} s^{-1}$ [91] respectively. Note that since A is so large, the correct order of magnitude is sufficient (for more details, see supplementary information of reference [58]).

The solution to equation 2.2 at a constant temperature is:

$$\frac{[P]}{[P_{tot}]} = 1 - e^{-k \cdot t} = 1 - e^{-A \cdot t \cdot e^{-\frac{E_a}{R \cdot T}}} \quad (2.4)$$

This equation applies to instances in which the temperature is time independent (not changing in time).

2.2.1 Static Tip Solution

When a thermal tip is brought into contact with the substrate and heated, the surface locally heats until it reaches a static temperature profile, $T(\bar{r}, \bar{r}_o)$, where $\bar{r} = (x, y, z)$ is the spatial coordinate, and $\bar{r}_o = (x_o, y_o, z_o)$ is the coordinate describing the tip position. The time scale for this heating has been suggested to be about $1 \mu s$ [92]. A quick calculation based on the time dependent heat equation computes a lower bound for the times scales. A typical organic polymer has a specific heat capacity, $C \approx 1$ kJ·kg⁻¹·K⁻¹ and a thermal conductivity, $k \approx 1$ W · m⁻¹·K⁻¹; the length scale is ≈ 20 nm. For these values, the associated heat equation time scale goes as 10^{-13} s. The discrepancy between the literature values and this computed value probably arises from the fact that the reference [92] may be including cantilever heating time-scales, which are also about $1 \mu s$ [93], and that air conduction for the above calculations are ignored. The near instantaneous equilibrium time scale acts as a lower bound, since given the length scales and the calculated time scale, the hyperbolic heat equation [94] is more appropriate. For this work, since we focus mostly on effects taking place on time scales below both limitations, we ignore the time dependence of the temperature profile. Assuming the static profile is instantaneously reached, the static solution for

¹Measurements performed in Professor Seth R. Marders lab at Georgia Institute of Technology.

a tip in contact with a substrate is:

$$\frac{[P]}{[P_{tot}]} = 1 - e^{-k \cdot t} = 1 - e^{-A \cdot t_d \cdot e^{\frac{-E_a}{R \cdot T(\bar{r} - \bar{r}_o)}}} \quad (2.5)$$

where t_d is the tip dwell time. Wanting to gain some insight into how equation 2.5 evolves and changes with various parameters, we leave the discussion of the temperature profile form until a later section of this chapter, and we will work with a 1-D model temperature profile. To find a reasonable temperature profile, the surface temperature should approach room temperature and should attain a peak at the point of contact (here the point of contact is $x_o = 1$). Since our attempt is to learn how the reaction evolves, one reasonable temperature profile that meets these criteria is given by:

$$T = T_o + (T_{peak} - T_o) \cdot e^{\frac{-|x|}{\lambda}} \quad (2.6)$$

where T_{peak} is the peak temperature, and lambda is a decay length. Substituting this form into equation 2.5, there are three parameters to tune: dwell time (t_d), peak temperature (T_{peak}), and decay length (lambda). Each parameter is discussed separately, and all simulations were done in Matlab to couple equation 2.5 with equation 2.6. Only one parameter is varied for each simulation.

2.2.1.1 Time Variation

Figure 2.2.2 shows that for a fixed decay length (lambda = 100 nm) and peak temperature ($T_{peak} = 250^\circ\text{C}$), longer dwell times increase the concentration of the final product; as seen from the inset, the Full Width at Half Maximum (FWHM) also increases with dwell time. Physically, as time elapses the chance of a reaction increases; this manifests in two different ways: the percent transformation increases everywhere up to a maximum and the FWHM continues to increase even beyond the max percent transformation.

Developing some intuition with dwell time correlates to understanding how writing

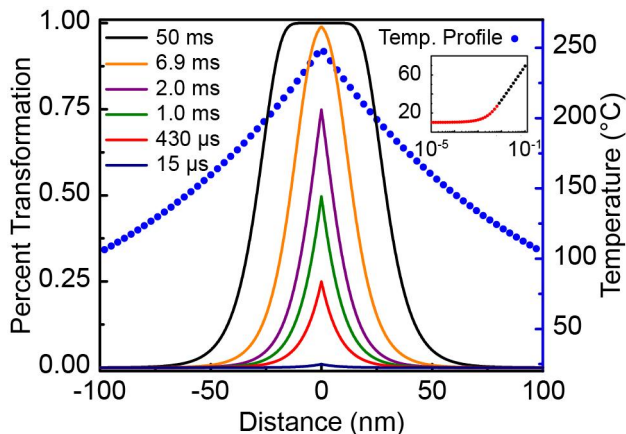


Figure 2.2.2: Time Dependence of equation 2.5 with equation 2.6.

speed affects TCNL. As will be demonstrated in a subsequent section, the correspondence between the speed and inverse dwell time is not perfect because of the increased complexity resulting from the tip motion; however, the analogy between inverse time and speed suffices to develop insight into tip speed. For example, Figure 2.2.2 shows that to span from 0.01 to 0.99 percent transformation, the dwell time scales span from 15 μs to 6.9 ms; this is 3 orders of magnitude in time scales. Based on this observation for dwell time, we expect that in order to span from 0.01 to 0.99 percent transformation at a fixed temperature, the speed will span 3 orders of magnitude. As will be discussed in section 2.2.3, this range is modeled, and in chapter three, the range is experimentally demonstrated.

2.2.1.2 Temperature Variation

Figure 2.2.3 shows several different peak temperature profiles (543 K, 523 K, 503 K, 493 K, 468 K, and 433 K) at a fixed dwell time of 6.9 ms and a fixed decay length of 100 nm. As the temperature increases, product concentration also increases; looking back at equation 2.3, the reaction rate, k , has a temperature dependence akin to a Boltzmann factor, and it is indeed related to the probability that a reaction will occur [87]. Higher temperatures increase the probability of reaction, and this mathematically manifests as an increase in the reaction rate. The ability to tune

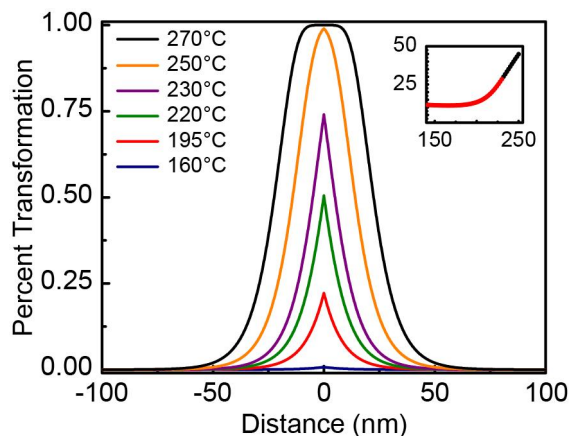


Figure 2.2.3: Temperature Dependence of equation 2.5 with equation 2.6.

the reaction rates with temperature is tantamount to controlling the extent of a localized reaction, and we exploit this dependence in chapter three to create controlled concentration profiles.

One of the key differences between time and temperature is the scale to achieve the same results. To span most of the product range (0.01-0.99), for temperature requires about 433 K-543 K; whereas, for the same product range, time requires 3-4 orders of magnitude. The scale differences arise from the fact that time alters the reaction rate linearly, whereas temperature affects the reaction rate through a Boltzmann exponential factor. As the thermal energy approaches the activation energy, there is a rapid turnover in the reactions probability; this leads to the short range over which the temperature activates the reaction.

2.2.1.3 Decay Length

Figure 2.2.4 shows four different decay lengths (1 nm, 10 nm, 100 nm, and 1000 nm), along with the associated temperature decay profile. The solid lines represent the percent transformation, while the scatter plot is the temperature profile. The peak temperature and the dwell time are fixed (523 K and 6.9 ms). As expected, the maximum probability never changes. Figure 2.2.4 illustrates that as the temperature profile decays, the products concentration decays at a much faster rate than the

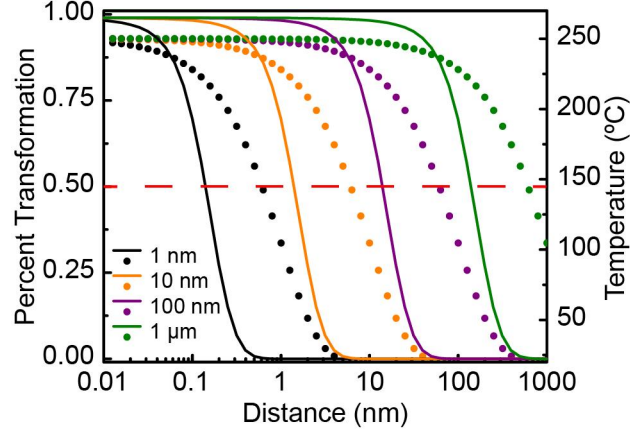


Figure 2.2.4: Decay length dependence of equation 2.5 with equation 2.6. The lines represent the extent of the chemical reaction, while the dots represent the decaying temperature profile.

original profile. The FWHM of the transformation is the intersection of the dashed (red) line with the solid lines; as can be seen, the FWHM values are significantly smaller than the associated decay lengths. This difference in FWHM and decay length arises from the final product concentration profile being the composition of a decaying function with a decaying profile. Assuming an exponentially decaying temperature, the percent transformation functional form shows an exponential of an exponential. The first exponential is from the static solution to the first order chemical kinetics equation (equation 2.4); the second arises from the Arrhenius equation (equation 2.3); the third arises from the temperature profile choice. Previously, it was hypothesized that the high resolution from TCNL results from the rapidly decaying temperature profile [68], but this is only part of the story. The sharp resolutions in TCNL result from the coupling between the chemical kinetics and the decaying profile.

The physical realization of variable decay lengths comes from the different ratios between the substrate and the silicon tips thermal conductivities. For example, a greater substrate conductivity versus tip conductivity results in a greater decay length, whereas a greater tip conductivity results in a smaller decay length [95].

While there are no results about varying substrate conductivity in this thesis, this type of study offers ample potential for studying materials effects, especially when multi-layer films are considered since they can artificially cause smaller decay lengths.

While resolution is not one of the optimized components for this work, based on the discussion from these 3 sections, tuning resolution involves effects of dwell time, temperature, and the substrates material properties. Despite these complexities, chemical kinetics plays the central role in determining the overall outcome.

2.2.2 Effects of Multiple Points

Having discussed the different tunable parameters, it is instructive to examine how multiple TCNL treated points interact with one another. It is clear from Figure 2.2.2 to 2.2.4, that if two points of contact are far enough apart, they have a negligible effect on each other. Bringing the two points closer until there is an overlap between the product profiles introduces secondary effects. Taking each point to be a separate event and using equation 2.5, the first contact point introduces a product profile concentration as:

$$\frac{[P_1]}{[P_{tot}]} = 1 - e^{-A \cdot t_d \cdot e^{\frac{-E_a}{R \cdot (T_o + (T_{peak} - T_o) \cdot e^{\frac{-|x-x_1|}{\lambda}})}}} \quad (2.7)$$

where x_1 is the point of contact for the first event. The remaining percentage of un-reacted substrate, $[R]$, is written as:

$$[R] = e^{-A \cdot t_d \cdot e^{\frac{-E_a}{R \cdot (T_o + (T_{peak} - T_o) \cdot e^{\frac{-|x-x_1|}{\lambda}})}}} \quad (2.8)$$

$[R]$ represents the substrates spatial distribution with which the second contact event can interact. The product concentration from the second event is:

$$\frac{[P_2]}{[P_{tot}]} = e^{\frac{-E_a}{R \cdot (T_o + (T_{peak} - T_o) \cdot e^{\frac{-|x-x_1|}{\lambda}})}} \left(1 - e^{-A \cdot t_d \cdot e^{\frac{-E_a}{R \cdot (T_o + (T_{peak} - T_o) \cdot e^{\frac{-|x-x_2|}{\lambda}})}}} \right) \quad (2.9)$$

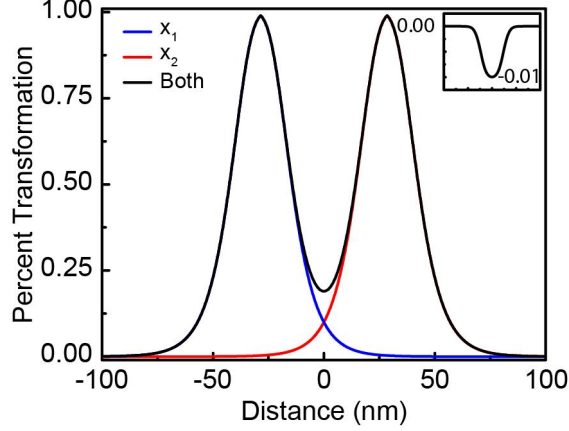


Figure 2.2.5: Interaction between two contact points described in equation 2.10.

where x_2 is the contact point of the second event. Combing equation 2.7 and equation 2.9, the final product concentration for the substrate is:

$$\frac{[P_f]}{[P_{tot}]} = \frac{[P_1]}{[P_{tot}]} + \frac{[P_2]}{[P_{tot}]} = 1 - e^{-A \cdot t_d \cdot e^{\frac{-E_a}{R \cdot (T_o + (T_{peak} - T_o) \cdot e^{-\frac{|x-x_1|}{\lambda}})}}} - e^{-A \cdot t_d \cdot e^{\frac{-E_a}{R \cdot (T_o + (T_{peak} - T_o) \cdot e^{-\frac{|x-x_2|}{\lambda}})}}} \quad (2.10)$$

Equation 2.10 demonstrates how two separate points of contact interact with each other. Figure 2.2.5 shows the interaction between two points of contact (decay length of 100 nm, T_{peak} of 523 K, t_d of 6.9 ms); the red and blue curves represent the product concentration for the individual events, and the black curve is the total interaction between both events occurring. There is an overlap region between the two events, corresponding to the interaction between the two events. While for any exponential decaying profile, there is always some overlap, the effects become negligible once the points are separated by a large distance. The inset shows the difference between the interacting events and individual, non-interacting events; the fact that the difference is measurably non-zero demonstrates that the interaction between the tip and the substrate is *not* a convolution of events except at large distances.

2.2.3 Extension to a Moving Tip

The previous section showed that two nearby points of contact interact with each other. If a tip is in motion, there should be a compact mathematical relationship between the temperature profile and the product concentration. Assuming an instantaneous temperature profile, the temperature profile moves along the substrate simultaneously with the tip. As seen from the perspective of an individual point, the point is locally subjected to an initial temperature, T_0 ; after an infinitesimal time step later (Delta t_0), the same point is now subject to temperature T_1 for another infinitesimal time step (Delta t_1). Using the same approach developed in the previous section, the final percent product concentration after both time steps is:

$$\frac{[P_f]}{[P_{tot}]} = 1 - e^{-A \cdot (\Delta t_0 \cdot e^{\frac{-E_a}{R \cdot T_0}} + \Delta t_1 \cdot e^{\frac{-E_a}{R \cdot T_1}})} \quad (2.11)$$

Continuing this process for time steps (Delta t_2 , Delta t_3 , \dots) and the subsequent temperatures (T_2, T_3, \dots), the final product concentration is given by:

$$\frac{[P_f]}{[P_{tot}]} = 1 - e^{-A \cdot \sum_j \Delta t_j \cdot e^{\frac{-E_a}{R \cdot T_j}}} = 1 - e^{-A \cdot \int e^{\frac{-E_a}{R \cdot T(t)}} dt} \quad (2.12)$$

where the final integral comes from assuming infinitesimal time steps. Finally, assuming a constant speed, equation 2.12 can be re-written as:

$$\frac{[P_f]}{[P_{tot}]} = 1 - e^{\frac{-A}{v} \cdot \int e^{\frac{-E_a}{R \cdot T(x_o, x)}} dt} \quad (2.13)$$

where v is the motion of the tip, x_o represents the tips position during translation, and x represents the point of interest.

While only 1-D expressions are examined here, similar results can be derived for 2 or 3-D. More complex formulas for different circumstances are derived from the analysis suggested in this and the previous section.

Equation 2.13 is the starting point for understanding TCNL. As will be discussed in a subsequent section, there is great uncertainty in the determining the exact tip-induced temperature profile. Despite these difficulties, significant insight can be

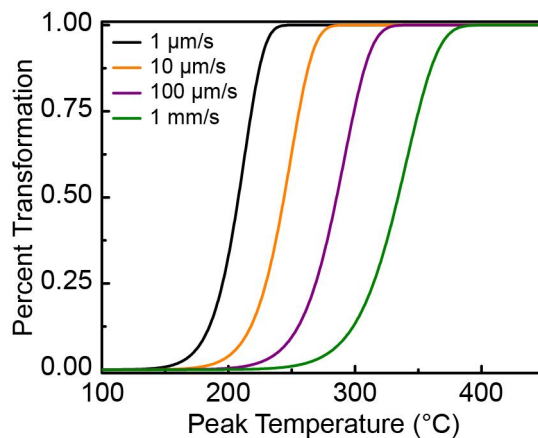


Figure 2.2.6: Plot of equation 2.13 with decay length of 100 nm.

gained from assuming a temperature profile to learn how different parameters alter the outcome. Using the same decaying exponential profile (equation 2.6) with a decay length of 100 nm, equation 2.13 is plotted in Figure 2.2.6 for four different speeds ($1 \mu\text{m/s}$, $10 \mu\text{m/s}$, $100 \mu\text{m/s}$, 1mm/s). Looking at a fixed speed ($10 \mu\text{m/s}$), the functional dependence on the peak temperature is an S-shaped curve; this S-shape results from the increased reaction rate from an increased temperature. This simulation agrees with the previous sections discussion of how temperature affects the static tip situation. At low (high) temperatures less (more) of the substrate undergoes the chemical transformation. While at higher temperatures there is a plateau in product concentration resulting from the finite reactant concentration, negligible amounts of the polymer transform at low enough temperatures.

2.2.4 Effects of Speed on TCNL

Mirroring the discussion of varying dwell time, simulations of different speed conditions are shown in Figure 2.2.6. The signature S-curve typical to bounded growth equations is still present for all speeds, but the curves shift to the right with increasing speed. Comparing speed to inverse dwell time and mimicking the discussion in the dwell time section, allows us to conclude that for faster (slower) speeds, less (more) of the polymer undergoes the chemical transformation.

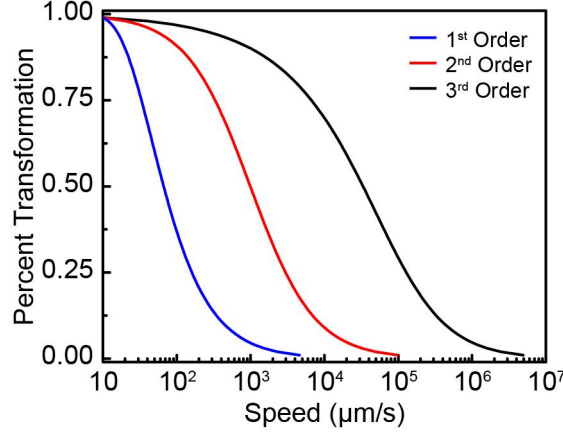


Figure 2.2.7: Plot of equation 2.15 and higher order variants; the reference speed is $10 \mu\text{m/s}$ and the reference transformation percentage is 0.99.

To see how speed evolves as a function of polymer transformation, equation 2.13 can be re-written as:

$$v = \frac{A \cdot C}{\ln(1 - Pr)} \approx \frac{1}{\ln(1 - Pr)} \quad (2.14)$$

where $C = \int e^{\frac{-E_a}{R \cdot T(x_o, x)}} dt$ and $Pr = \frac{[P]}{[P_{tot}]}$ is the percent transformation. Equation 2.14 still maintains the temperature dependence through the C variable, but using a reference Pr_{ref} at reference speed, v_{ref} , different speeds can be computed as a function of percent transformation:

$$v = v_{ref} \frac{\ln(1 - Pr_{ref})}{\ln(1 - Pr)} \quad (2.15)$$

The interesting thing about equation 2.15 is that it removes the complications of knowing an exact temperature profile, and replaces it with an experimentally determined reference percent transformation. We leave it to chapter three to discuss the limitations and difficulties in determining an exact Pr_{ref} .

Equation 2.15 is plotted for a reference speed ($10 \mu\text{m/s}$) with a reference percent transformation (0.99) in Figure 2.2.7. The variants of equation 2.15 for higher order reactions (2nd and 3rd order) are also shown in Figure 2.2.7. Interestingly, to span the percent transformation of 0.01 to 0.99, a first order reaction requires about 3 orders of magnitude for speed, whereas a second order and a third order reaction

requires about 5 and 7 orders of magnitude respectively. The differences in the speed range provide a nice physical basis for determining whether a substrate patterned with TCNL is a first, second, or third order reaction. The 3 orders of magnitude for a first order reaction was previously predicted based on the analogy between the dwell time and inverse speed.

There is also a rather obscure relationship between speed and the order of reaction; taking a $Pr_{ref} = 0.9$, the computed speed for a $Pr = 0.99$ follows the relationship:

$$v = \frac{v_{ref}}{10^{n-1} + 1} \quad (2.16)$$

where n is the order of reaction. Figure 2.2.7 and equation 2.16 tell us that as the substrates order of reaction increases, the corresponding reaction becomes more immune to changes in speed. Therefore, higher order reactions are therefore better candidates for reliable high-speed TCNL patterning, since they are less affected by speed.

2.3 Expanding to the Surface and 3-D

Equation 2.13 provides the probability for the chemical transformation for a single point in space. To expand this equation to a surface or 3-D space, consider a volume of space which has been discretized into small pockets (see Figure 2.3.1 for a 2-D schematic). Equation 2.13 describes the probability for each point, and a sum over the probability in the space of interest computes the number of sites undergoing the entire reaction:

$$N = \sum_i Pr_i \quad (2.17)$$

where N is the number of sites that have undergone the reaction, Pr_i is the probability of transformation at site i , and the summation is over available sites in the volume of interest.

Pr_1	Pr_2	Pr_3	Pr_4	Pr_5	Pr_6	Pr_7	Pr_8	Pr_9	Pr_{10}
Pr_{11}	Pr_{12}	Pr_{13}	Pr_{14}	Pr_{15}	Pr_{16}	Pr_{17}	Pr_{18}	Pr_{19}	Pr_{20}
Pr_{21}	Pr_{22}	Pr_{23}	Pr_{24}	Pr_{25}	Pr_{26}	Pr_{27}	Pr_{28}	Pr_{29}	Pr_{30}
Pr_{31}	Pr_{32}	Pr_{33}	Pr_{34}	Pr_{35}	Pr_{36}	Pr_{37}	Pr_{38}	Pr_{39}	Pr_{40}
Pr_{41}	Pr_{42}	Pr_{43}	Pr_{44}	Pr_{45}	Pr_{46}	Pr_{47}	Pr_{48}	Pr_{49}	Pr_{50}

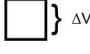


Figure 2.3.1: Schematic for equation 2.17.

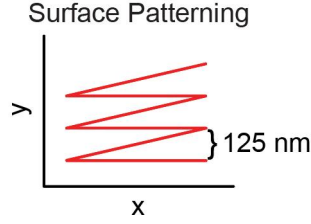


Figure 2.3.2: Rastering image to pattern a substrate.

Dividing N by the total number of available reactive sites gives:

$$\frac{N}{N_{tot}} = \frac{\sum_i Pr_i}{N_{tot}} = \frac{\sum_i Pr_i}{\sum_i 1} \quad (2.18)$$

where N_{tot} is the total number of available sites. Finally, since each site occupies a fixed volume, ΔV , the above can be re-written as:

$$\frac{N}{N_{tot}} = \frac{\sum_i Pr_i \cdot \Delta V}{N_{tot} \cdot \Delta V} = \frac{\sum_i Pr_i \cdot \Delta V}{\sum_i \Delta V} = \frac{\int \int \int Pr dx dy dz}{\int \int \int dx dy dz} \quad (2.19)$$

where the integral comes from assuming a continuous distribution of reactive sites. Here x and y are in the plane of the surface and z is normal to the surface. To compute the effect on a local region of a surface, the z integration can be ignored:

$$\frac{N}{N_{tot}} = \frac{\int \int Pr dx dy}{\int \int dx dy} \quad (2.20)$$

For this work, we ignore the y -integration since our patterning technique (see Figure 2.3.2), places consecutive zig-zag lines close to one another ($\approx 125/2$ nm > FWHM for the polymer substrate). This allows us to proceed with using equation 2.15.

For 3-D body effects, the z -dependence *cannot* be ignored, and it will be further discussed in chapter four.

2.4 *Discussion of the Assumed Temperature Profile*

The exact form for the temperature profile is incredibly difficult to compute. There is limited evidence to suggest that the heat equation holds down to these length scales [96]. There are some works which assume the heat equation holds, but often boundary conditions are ignored, such as convective cooling [97], calling into question whether the results show the validity of the heat equation. Solutions to the heat equation are boundary condition dependent and because of sub-continuum effects in the tip, these conditions are difficult to compute. Given the length scales, the Boltzmann Transport equation for the phonon distribution provides a more accurate solution [98]. Moreover, the literature agrees the main form of conduction is through the air [99], and while this is undoubtedly true, computing this effect on the temperature profile is also difficult and mostly done with Monte Carlo simulations [100]. There are also other effects to consider here, such as the glass transition temperature and visco-elastic behaviors [52].

Since there is uncertainty in the temperature profile, we make an approximation based on some previously attained results. The assumed profile will be the same one used throughout this chapter, specifically the form in equation 2.6. The motivation for this profile comes from the fact that if the static heat equation holds, the Laplacian form demands an exponential decay. Previous results suggest that it is possible to attain a 12 nm resolution moving at 2 mm/s on a similar polymer substrate [68], and we use this result to determine the decay length. Assuming the tips radius of curvature is 20 nm, the time scales associated with this speed is $20 \text{ nm}/(2 \text{ mm/s}) \approx 10 \mu\text{s}$. Substituting this into equation 2.4, the computed temperature is about 650 K to attain 99% conversion. Using this as the peak temperature in equation 2.6 and substituting this temperature profile into equation 2.13, comparisons of different decay lengths (1 nm, 10 nm, 50 nm, 100 nm, 1000 nm) shows that a decay length of 100 nm was closest to the 12 nm resolution at 1 mm/s. We use this form for our temperature

profile throughout this work.

2.5 Final Word

The intent of this chapter was to help develop the intuition and some of the basic math, chemistry, and physics for TCNLs governing mechanisms. Using a chemical kinetics model and working with a temperature profiles, it was shown how different parameters (decay lengths, peak temperature, and time scales) affect the mechanisms. The analytical methods necessary for predicting how more complicated situations will react were demonstrated. The model and results discussed in this section will be used for the remaining chapters.

CHAPTER III

CHEMICAL KINETICS MODEL

3.1 Introduction

ThermoChemical NanoLithography is a nano-scale lithographic technique that combines thermally activated chemical transformations with a spatially localized temperature profile induced by a thermal cantilever. Researchers have patterned with TCNL to site specifically attach proteins and other biomolecules [64], reduce graphene oxide to graphene [65], convert hydrophobic materials to hydrophilic [69], crystallize ceramic materials [67], and to pattern semi-conducting organic polymers [70]. While these works have demonstrated the impressive range of materials suitable for TCNL, there has been little attempt to quantify and model the technique. Even though there is much to gain from describing TCNL with a chemical kinetics model, it is equally important to verify and prove the assumptions and equations experimentally.

The next two chapters are dedicated to experimental verification of the equations derived in chapter two. The key differences between this chapter and the next is that here we focus on surface effects, ignoring the heat penetration into the sample. To study only surface effects, we couple the previously described thermally activated polymer with a fluorophore and fluorescence microscopy; because of the polymer substrate is crosslinked, the fluorophore should only attach at or very near the surface. Using this method, the basic principles derived in chapter two will be verified, and then we apply the model to design patterns with controlled chemical concentration variations. We start with a brief review of the electric and mechanical properties of the thermal cantilevers.

3.2 Review of Thermal Cantilevers and Instrumentation

The thermal cantilevers used throughout this work have an integrated heater built above the tip; when biased with a voltage, these semi-conducting cantilevers heat due to resistive heating. While there is ample literature on the thermal and electric properties of thermal cantilevers [93, 101, 102, 103], the basic concepts, terms, and properties are reviewed in this section. All tips used in this work were fabricated by Professor William P. King's lab at University of Illinois at Urbana Champaign.

3.2.1 Thermal Cantilevers: Fabrication and Design

The cantilevers are fabricated with ion implantation methods to introduce contrasting doping levels. The cantilevers are etched from a silicon wafer; the wafer comes with a native doping concentration of about $10^{14}/\text{cm}^3$. The legs are ion implanted with high doping levels (Phosphorous, *n*-type $10^{20}/\text{cm}^3$) causing them to be highly conductive, and the integrated heater region above the tip is doped with low levels (10^{17} - $10^{18}/\text{cm}^3$) (see Figure 3.2.1) [101]. While the doped legs are highly conductive, the heater region is more resistive, and as a result of this doping contrast most of the electric power ($\approx 90\%$) is dissipated in the low doped region [51, 104]. This influx of energy results in the localized heating of the low doped region; because of this localized heating, the low doped region is referred to as the heater. Finally, the tips are sharpened with an oxidation procedure, described in the literature [105].

The fabricated cantilevers have a reported stiffness of 0.1-1N/m. The resonant frequency is approximately 60-70 kHz; the length and thickness are about 150 μm and 600 nm respectively [93, 106]. The tip height is about 1.5 μm , and the radius of curvature is about 20 nm [93]. The mechanical properties are important since they can tune different thermo-electrical properties, such as thermal constriction [102].

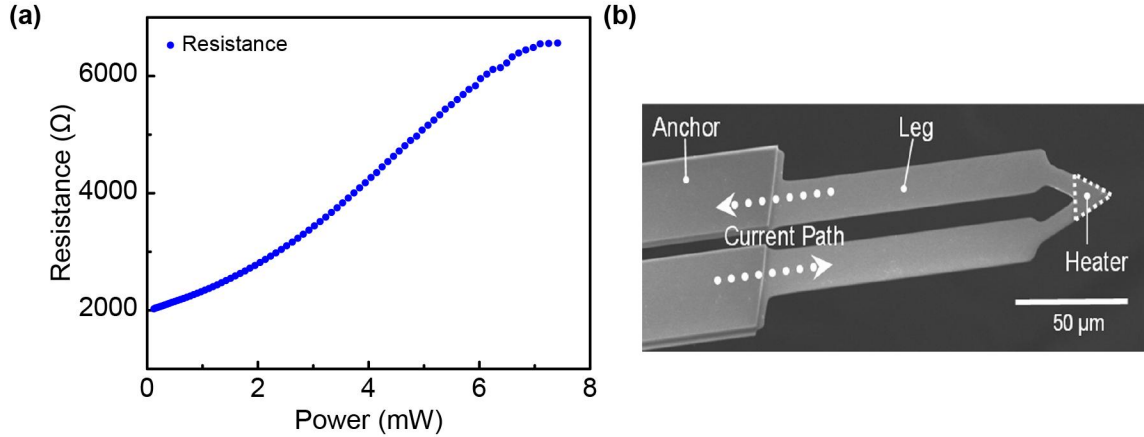


Figure 3.2.1: (a) Graph of thermal cantilever resistance versus power dissipated across the cantilever; 90% of the power is dissipated in the heater region. (b) Scanning Electron Microscope (SEM) image of a thermal cantilever. Image [104] reprinted with copyright permission © 2008 Taylor and Francis.

3.2.2 Electronic Properties

The heater region dissipates most of the power because of the doping contrast. As in most metals, the resistance in the silicon tip has a positive temperature coefficient [93] because of the increased scattering from phonons [107]. Above a certain temperature, the temperature coefficient switches to negative values because the increased temperature causes the intrinsic carriers to dominate conduction [108]; the temperature, at which this switch occurs, is commonly referred to as the thermal runaway. Measurements with Raman Spectroscopy reveal that the thermal runaway occurs at about 550 – 600 °C in the heater region [93]. Raman spectroscopy also shows that the integrated heater temperature is linear in both cantilever resistance and dissipated power and because of the consistency of the thermal runaway temperature, both the resistance and power can be used to estimate the heater temperature to about 10% accuracy.

The temperature at the tip-surface interface is reported to be less than the heater region; this results from thermal transport down the tip and sub-continuum effects. Depending on the thermal properties of the substrate, the tip-substrate interface

temperature is $\approx 0.6-0.1$ of the heater regions temperature; more thermally conductive surfaces typically have a lower efficiency (≈ 0.1 for graphene [91]), while substrates with a lower thermal conductivity have higher values (0.3-0.6 for organic substrates [69, 109]). This loss is referred to as the tip efficiency [109].

3.2.3 Instrumentation

Throughout this thesis, all AFM imaging and patterning are done with an Agilent 5600 LS AFM. The closed loop scanner range for this instrument is approximately 90-100 μm . Unless otherwise stated, all AFM images are in contact mode. The AFM is shown in Figure 3.2.2a. The adapted nose cone for mounting the thermal cantilevers on the scanner is shown in Figure 3.2.2b; the nose cone is designed by Anasys Instruments to hold a printed circuit board (PCB) mounted with a thermal cantilever (see Figure 3.2.2c). The PCBs also come from Anasys Instruments. Silver paint electrically connects the legs of the thermal cantilever to the PCB contacts (Figure 3.2.2c).

The wires from the PCB contacts are connected to the circuit schematic shown in Figure 3.2.2d. The power supply for the circuit is an Agilent E3648. The power supply is updated with a computer script. The sense resistor R_s is 2 k Ω , and a voltage divider consisting of two 1 M Ω resistors measures half the voltage drop across the sense resistor.¹ An NI-USB 6216 Data Acquisition (DAQ) device measures the voltage divider. An alternative circuit to this one uses two 1 k Ω resistors in series and the voltage is read across one of the 1 k Ω resistor. Coupling measurements from the DAQ with the controlled voltage output from the power supply, any electronic information about the thermal cantilevers could be computed. Equations for different electronic measurements are shown in Table 3.1. All lithography programs were written in house

¹The Data Acquisition (DAQ) Device for this work is limited up to 10 V; since the maximum output of the voltage supply is 20 V, by halving the sense resistor, the limits of the DAQ are never reached.

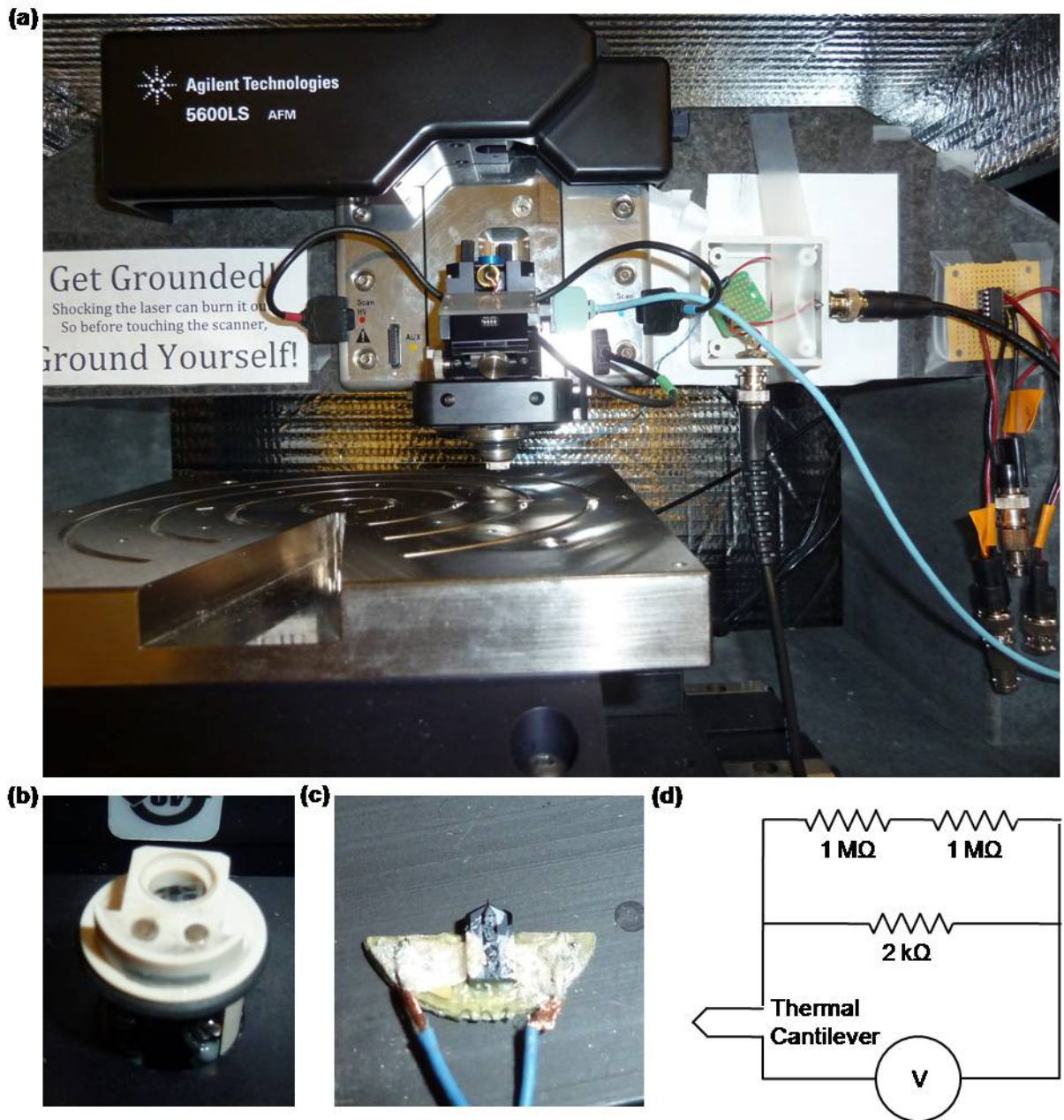


Figure 3.2.2: (a) Shown is an image of the Agilent 5600 LS series mounted with a thermal cantilever. (b) Shown is the nose cone adaptor used to mount the printed circuit board chip (PBC) shown in (c). (c) This is the PCB for mounting the thermal cantilever (mounted with a thermal cantilever). The silver paint connect the contacts to the legs of the thermal cantilever to complete the circuit. (d) This is one example of a circuit used to measure and compute all the electrical properties of the thermal cantilever according to Table 3.1.

Table 3.1: Computer Circuit Components

Computed Component	Symbol	Equation
Current	I	$I = \frac{V_{DAQ}}{1000}$
Cantilever Voltage	V_C	$V_C = V_{tot} - 2 \cdot V_{DAQ}$
Cantilever Power	P_C	$P_C = V_C \cdot I$
Cantilever Resistance	R_C	$R_C = \frac{V_C}{I}$

(using both C++ and Matlab), and the voltage and power were monitored through a computer programmed feedback.

All patterns are made with a loading force between 30-300 nN; the best results were found with loading forces between 100-200 nN. Lower loading forces are employed for higher resolutions. Higher loading forces are used for experiments requiring high speeds to ensure contact while writing.

All fluorescence measurements come from a Nikon Eclipse TE2000 inverted epifluorescence microscope. Images are taken with either an Andor iXon or a Roper CoolSnap CCD camera. The filter used throughout this chapter has an excitation filter centered around 620 nm, an emission filter centered around 700 nm, and a dichroic mirror center around 660 nm. All images were taken in liquid (Phosphate Buffer Solution, PBS) with either a 40x Oil immersed objective (1.3 Numerical Aperture, NA) or a 60x water immersed objective (1.2 NA). All results shown were reacted with a 25 nM solution of the fluorophore DyLight 633 functionalized with an N-hydroxysuccinimide ester group (NHS DyLight 633, Thermo Fisher Scientific Pierce Biotechnology) for approximately 1 hour. They were rinsed with alternating cycle of water and PBS for about 5 minutes.

Polymer substrates were synthesized and prepared as previously discussed in the literature [58, 64].

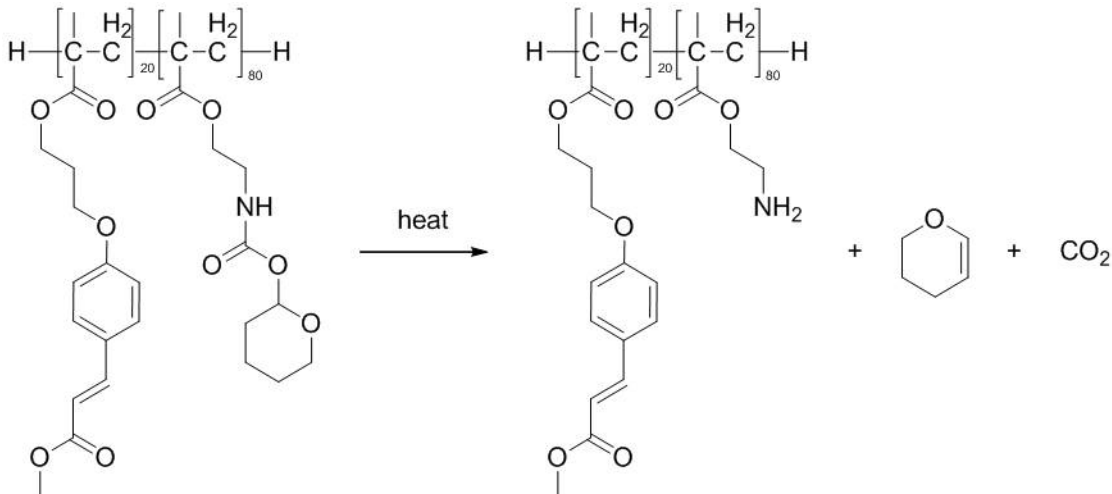


Figure 3.3.1: Chemical structure of polymer.

3.3 ThermoChemical NanoLithography: Temperature Dependence

The polymer substrate is the same one detailed in chapter two. The chemical structure of the polymer, (poly((tetrahydropyran-2-yl N-(2-methacryloxyethyl)carbamate)-co-(methyl 4-(3-methacryloyloxypropoxy)cinnamate))) is shown again Figure 3.3.1; for convenience in this chapter, we refer to the spin case polymer substrate as the polymer or polymer substrate. The polymer was synthesized by Professor Seth R. Marder's lab at Georgia Institute of Technology. Synthesis and chemical preparation of the polymer is described elsewhere [64, 110], but some key features are discussed here.

The polymer has a protected functional amine group; when heated, the protection group dissociates, leaving behind an exposed functional group to which various complementary chemistries can be attached [64]. The dissociated groups (gaseous CO₂ and dihydropyran) are volatile enough that more than likely they diffuse away [58]. To ensure the polymer substrate structure remains intact, the polymer's glass transition temperature is increased with an increased UV induced cross-linking between the polymer's cinnamate side chains [64].

3.3.1 Methods and Description of Experiments

A typical experiment to test the models validity is shown in Figure 3.3.2a, where an array of squares tests the validity of the chemical kinetics model; each square is written at a fixed heater temperature. The numbers indicate typical values for power dissipated across the cantilever. As explained in section 3.2.2, the power dissipated across the cantilever is approximately linear to the heater temperature, and so the heater temperature in each square is maintained through a computer feedback system which monitors and adjusts the power dissipated across the tip. The minimum change in power is limited by Johnson Shot noise [102, 111]. Figure 3.3.2b shows the polymer before it is patterned. Because of the spin-coating and thorough cleaning, the polymer surface is flat and smooth. After the patterning, noticeable changes in the topography can be seen in Figure 3.3.2c. At higher temperatures, the surface starts to show an enhanced topographic change, specifically a drop in the surface height caused by the material loss from the chemical transformation. At lower temperatures, there is less material loss since as we will discuss less of the polymer undergoes the chemical transformation. The correlation between the height and temperature is fairly difficult to accurately reproduce for this polymer; as a result, we focus on surface effects. We take the change in topography as qualitative evidence that the polymer has undergone a transformation. Z-penetration and 3-D conversion are discussed in the next chapter.

While AFM measurements are suggestive that TCNL has induced some form of change, fluorescence microscopy will semi-quantitatively verify the chemical nature of the transformation. By attaching an amine reactive fluorophore, the presence of a localized fluorescence signal both confirms the existence of exposed amines and provides a mechanism to analyze how temperature affects the TCNL process. Fluorescence microscopy is an effective method for semi-quantitatively analyzing chemical concentrations since the emission intensity is linearly proportional to the concentration.²

²Special care needs to be taken to quantitatively use fluorescence microscopy because fluorescence

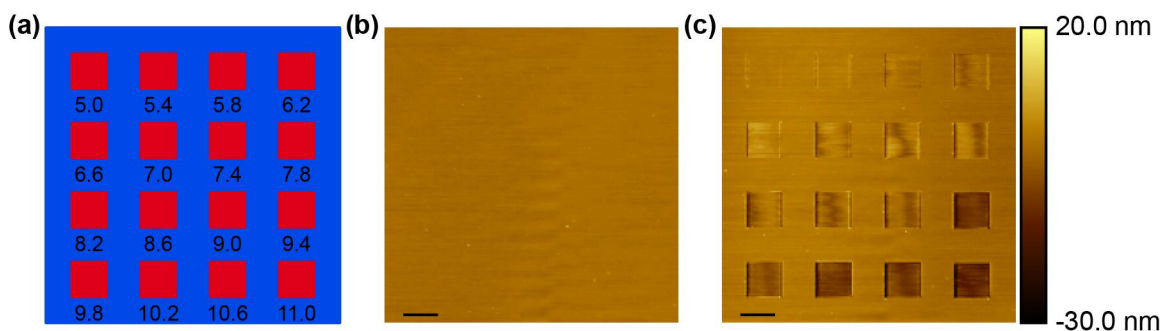


Figure 3.3.2: (a) Typical experiment to test the chemical kinetics model. The numbers indicate typical dissipated powers for these experiments. (b) AFM image of the polymer substrate prior to patterning. (c) AFM image of the pattern detailed in (a).

Other methods, such as X-ray Photoelectron Spectroscopy (XPS) or Friction Force Microscopy (FFM), allow for a similar analysis to be done, but each has its drawback. XPS, for example, is tedious and would be difficult to demonstrate designing patterns [112]; analysis of FFM signals would be difficult since there may not be a linear relationship between the friction measurement and the concentration (there is also the interaction between topography and the friction measurements which may alter the results) [113]. Fluorescence microscopy provides an efficient, straightforward method to quantifying chemical concentrations.

After the patterns are made, a fluorophore (here NHS-Dylight 633, 25 nM in DMSO), is used to label the patterned areas. The bound dye concentration relates to the exposed amine concentration. In areas with a greater concentration of exposed amines, more dye attaches. When imaged with fluorescence microscopy, areas with a more dye emit with a greater intensity and this produces a brighter signal. Dimmer signals correspond to less dye and lower concentrations of exposed amines.

The dye concentration is kept low to reduce effects from quenching resulting from

 can exhibit non-linearity in concentration, such as quenching.

closely packed dye molecules and to insure an approximately linear relationship between the bound molecules and the amine concentration. This former effect is a known phenomenon, variations of which are used in other microscopy techniques, such as FRET [114, 115]. The latter comes from the fact that the concentration of exposed amines may be substantial enough that steric hindrance between dye molecules prevents proportional labeling of the amine concentration. Reducing the dye concentration alleviates this issue because the dye concentration will be proportional to the amine concentration at low concentrations. This last fact comes from naively suggesting³ the reaction between the dye and the exposed amines as an equilibrium equation:

$$\frac{1}{K_{eq}} = \frac{[D] \cdot [SA]}{[D - SA]} \quad (3.1)$$

where $[D]$ is the fluorophores solution concentration, $[SA]$ is the concentration of exposed surface amines, and $[D - SA]$ is the surface concentration of bound fluorophore. By maintaining a low dye concentration and assuming the amount of dye in the solution is much greater than the bound dye concentration, the number of attached dyes should approximately be proportional to the amine concentration.

The fluorophore labeled and imaged pattern corresponding to the sample in Figure 3.3.2 is shown in Figure 3.3.3. The orientation is the same as the experimental setup in Figure 3.3.2. We observe that qualitatively there is agreement between the chemical kinetics model and the fluorescence signal. For higher temperatures, the intensity signal is brighter versus the lower temperature patterns; this increased signal results from a greater fluorescent dye presence which indicates a greater concentration of exposed amines. Lower temperatures have less dye, and therefore indicate a lower concentration of amines. The last row also shows the intensity levels start to level off

³This assumption is naive since the reactions used in this work are irreversible. Arguments could be made that to first order, one still expects the chance of a reaction happening in this particular case to be proportional to the concentration of the amines and the concentration of the reactive dye. Thus, equation 3.1 still stands.

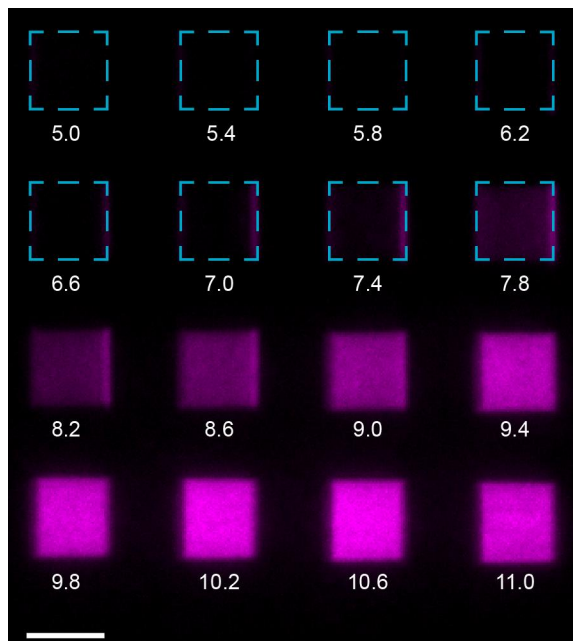


Figure 3.3.3: Fluorescence image from the experiment shown in Figure 3.3.2. Scale bar is $5 \mu\text{m}$.

and form the same plateau, consistent with the trend seen in Figure 2.2.6.

To compare this result with the model, there is a standard procedure [116] to follow; Figure 3.3.4 shows the steps. Briefly, first a background image is taken to correct for any uneven illumination resulting from the fluorescence lamp source; this background divides the raw data image to produce an even illumination field. Next the intensity levels for each square are measured; in order to avoid edge issues, the measurements must be inscribed in each square. For example, for a $5 \times 5 \mu\text{m}^2$ square, a $3 \times 3 \mu\text{m}^2$ concentric square was used; this is portrayed in Figure 3.3.4c with the inscribed cyan square. To correct for non-specific binding and for standard noise from images, the intensity levels of unpatterned areas were measured. Finally the relative intensity levels were calculated using the following formula:

$$I_{rel} = \frac{I_{measured} - I_{background}}{I_{plateau} - I_{background}} \quad (3.2)$$

where I_{rel} is the relative intensity levels of the square intensity, $I_{measured}$ is the measured flattened intensity of the patterned square, $I_{background}$ is the average background

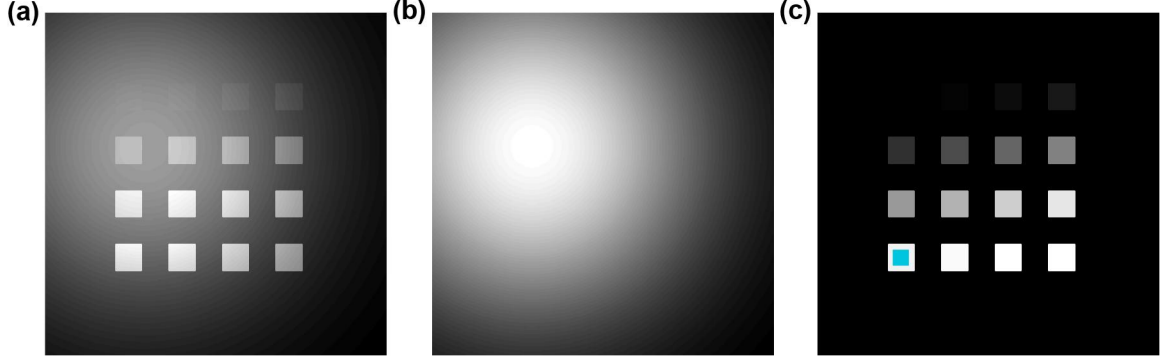


Figure 3.3.4: (a) Theoretical fluorescence image measured with an uneven illumination field. (b) Theoretical background image indicating the uneven illumination field. (c) Corrected fluorescence image resulting from dividing (a) by (b). The cyan square indicates an inscribed to measure a squares intensity level.

intensity resulting from non-specific binding and noise in the camera, $I_{plateau}$ is the average intensity of the plateau region (for Figure 3.3.3 it is the average intensity of the squares in the bottom row).

The relative intensity levels are compared against the corresponding relative version of equation 2.13:

$$\frac{P_{rel}}{P_{plateau}} = \frac{1 - e^{\frac{-A}{v} \cdot \int e^{\frac{-E_a}{R \cdot (T_o + (T_{peak} - T_o) e^{-\frac{|x|}{\lambda}})} dt}}}{1 - e^{\frac{-A}{v} \cdot \int e^{\frac{-E_a}{R \cdot (T_o + (T_{max} - T_o) e^{-\frac{|x|}{\lambda}})} dt}} \quad (3.3)$$

where T_{peak} is the peak temperature (K), P_{rel} is the relative concentration at T_{peak} , T_o is room temperature (K), lambda is the decay length (100 nm), T_{max} is the peak temperature (K) for the square with the maximum heater temperature in the plateau, and $P_{plateau}$ is the concentration at T_{max} . The peak temperature is calculated through:

$$T_{peak} = T_o + \eta \cdot (T_{heater} - T_o) \quad (3.4)$$

where eta is the efficiency parameter discussed previously and T_{heater} is the heater temperature. A reliable method for computing T_{heater} is described in the literature [51, 93]. To fit the model with the relative intensity, eta and E_a are taken as fitting parameters. Eta is load dependent and varies from tip to tip depending on the size

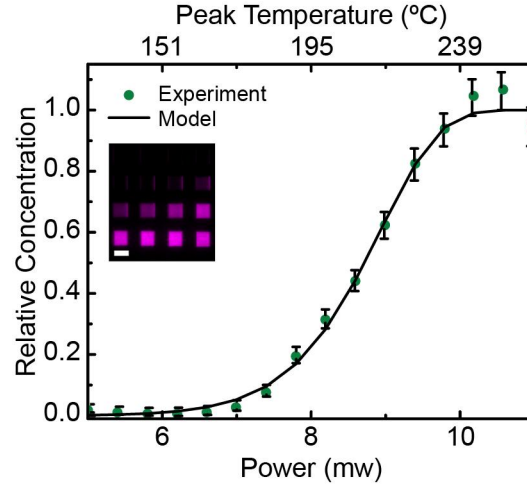


Figure 3.3.5: Comparison of the insets measured intensity (equation 3.2) (inset same as Figure 3.3.4) with the chemical kinetics model (equation 3.3). There is good agreement between the experiment and the model. The error bars represent the standard deviation from the measured intensity signal.

and radius of curvature; the calculations [117, 118, 119] for E_a from TGA showed a significant range and TGA comparisons to data are fairly sensitive to small changes in E_a (see supplementary materials of reference [58]). Figure 3.3.5 shows good agreement between the model and the experiment. This result confirms that a chemical kinetics models the technique, and will provide the basis for spatially controlling chemical reactions with TCNL.

Two key assumptions embedded in equation 3.3 are the form of the temperature profile and that the polymer motion is minimal in comparison to the chemical reaction. In chapter two, the temperature profile choice is discussed and assumed to be exponential decaying. The value for the decay length comes from matching some previous experimental results. The latter issue is justified because the glass transition temperature is increased through the enhanced cross-linking between polymer components. There is research which suggests that organic thin films show a decreased glass transition temperature from bulk material [120, 121]; this change may need to be accounted for in future works.

This model works up to temperatures below the polymer glass transition and

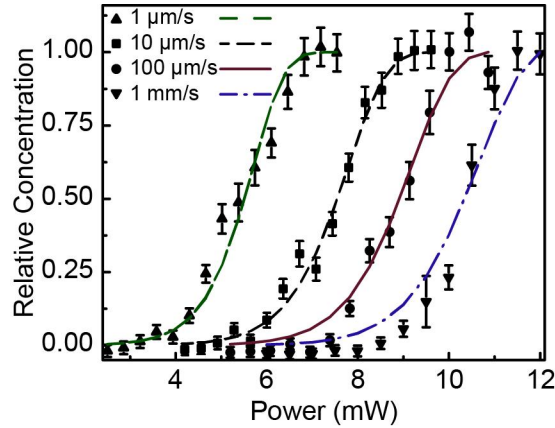


Figure 3.3.6: Comparison of the model with four different speeds ($1 \mu\text{m/s}$, $10 \mu\text{m/s}$, $100 \mu\text{m/s}$, 1mm/s). The results show the curves shift to the right as predicted in chapter two.

decomposition temperatures. If higher temperatures are applied, the labeled polymer starts to show a measured decreased in intensity signal, followed by a significant drop off in signal. The first effect is probably from a combination of the glass transition temperature effects and polymer decomposition. The second drop off can be attributed mostly to the polymer decomposition since AFM measurements indicate a height difference in the patterned areas consistent with the film thickness.

3.3.2 ThermoChemical NanoLithography: Speed Dependence

To test the dependence on speed, two experiments were designed. The first experiment follows the same procedures as in the previous section but with four versions of the patterns each at different speeds ($1 \mu\text{m/s}$, $10 \mu\text{m/s}$, $100 \mu\text{m/s}$, 1mm/s). The labeling and quantification are the same, and the result is shown in Figure 3.3.6. The same S-shaped curve is seen for all four speeds, but there is a corresponding shift of the curve to the right for increased speeds. This shift comes from the fact that faster speeds expose the polymer to the temperature profile for less time, resulting in a decreased rate of reaction. This shift is also predicted and discussed in chapter two (Figure 2.2.6).

The second experiment fixes the heater temperature and varies the speed across

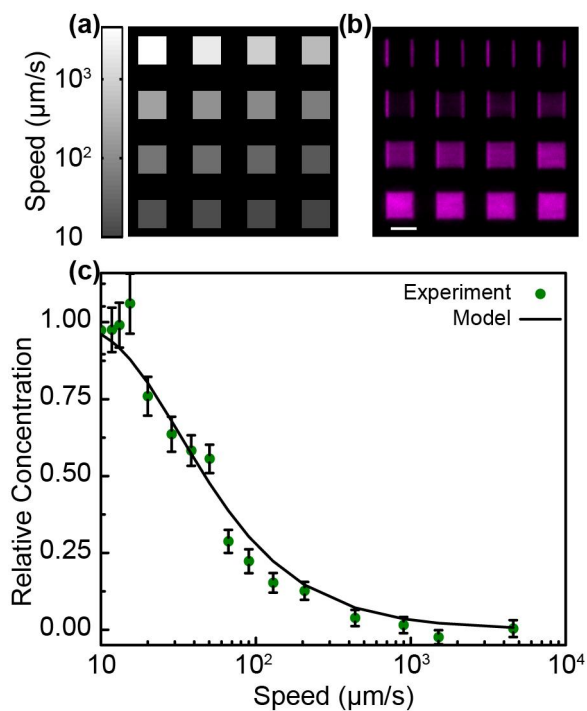


Figure 3.3.7: (a) Experimental setup in which the temperature is fixed, but the speed is varied across 3 orders of magnitude. (b) Fluorophore labeled image corresponding to the experiment in (a). (c) Comparison of the measured fluorescence intensity to the chemical kinetics model with a fixed temperature and varying speed.

approximately four orders of magnitude. The experiment and results are shown in Figure 3.3.7. As the speed increases, the relative percent of transformation decreases. The model predicts an exponential decay with respect to inverse velocity, and the measured data fits this prediction well.

Figure 3.3.7 shows that for a fixed temperature, in order for speed to span the chemical transformations range, approximately 3.5 orders of magnitude of speed are needed. This agrees with the predictions made in chapter two, and interestingly, this speed dependence provides more credence to a first order chemical kinetics model being applied to this chemical transformation. As discussed in chapter two, the chemical kinetics model predicts that 2nd and 3rd order reactions require a greater range in the speed (5 orders of magnitude for 2nd, and more than 7 for 3rd order); if the polymer were not a first order reaction, it would exhibit a different range in

speed than the observed range.

The key assumption for these experiments is that the temperature profile minimally changes at different speeds. We justify this with our own calculations in chapter two, which showed the temperature profile should reach static equilibrium near instantaneously; additionally, other temperature profile time scale calculations [92] are below the time scales associated with the tip radius and speeds up to about 10 mm/s.

The results shown in this section are the basis for using speed to control chemical reactions as will be discussed in a subsequent section.

3.4 Controlling Chemical Reactions

3.4.1 Controlling Chemical Reactions with Temperature

In section 3.3.2, it was shown how to model TCNL with chemical kinetics assuming a fixed speed and variable temperature. In this section, the model is applied to control the relative chemical transformation and produce intended chemical concentration gradient profiles at fixed speeds. The basic procedures are outlined in Figure 3.4.1, where the starting point is a calibration curve to find the fitting parameters η and E_a ; these are measured through the methods suggested in section 3.3.2. The designed pattern (here a linear gradient) is translated into a grayscale, which relates each intensity value to a percent transformation (i.e. from about 0 to 1). Coupling equation 3.3 with the measured E_a backs out the peak temperature field for a given relative concentration, and a new map detailing the peak temperature is drawn. Using equation 3.4 with the measured η determines T_{heater} (step not shown), and using the methods described in the literature, T_{heater} translates into a power map. Spatial distribution of the power controls the chemical concentration profiles to produce the initial design. Other parameters, such as load and speed, should be the same as those used to measure E_a and η .

An example of one set of designed patterns is shown in Figure 3.4.2. The three

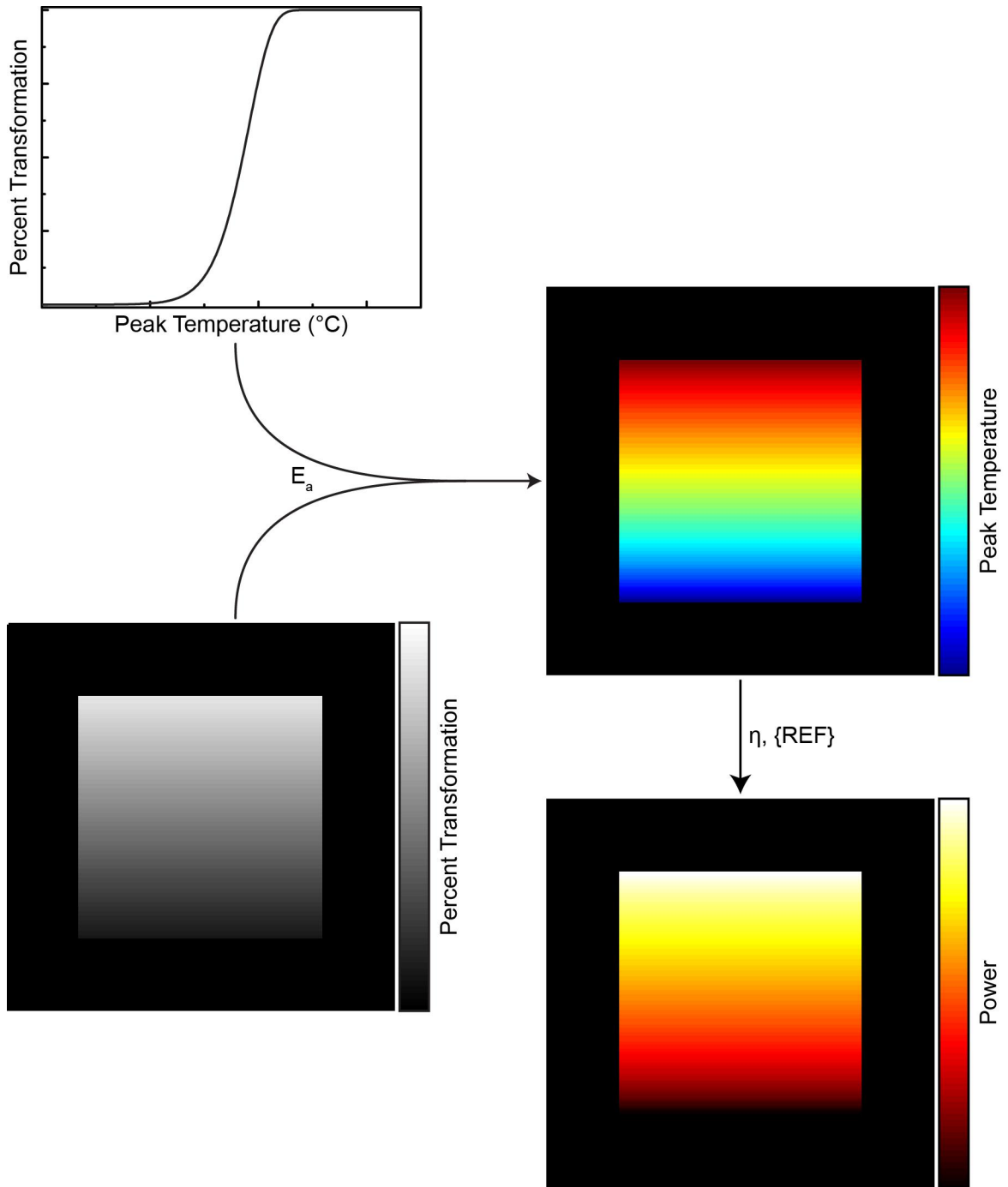


Figure 3.4.1: Schematic explaining how to create controlled chemical concentration profiles with TCNL. First, a calibration of the parameter E_a is combined with the intended pattern. This combination gives the peak temperature, T_{peak} , as function of position. Using methods described in the literature along with the measured η , T_{peak} is translated into the spatial distribution of dissipated power. More details are provided in the text.

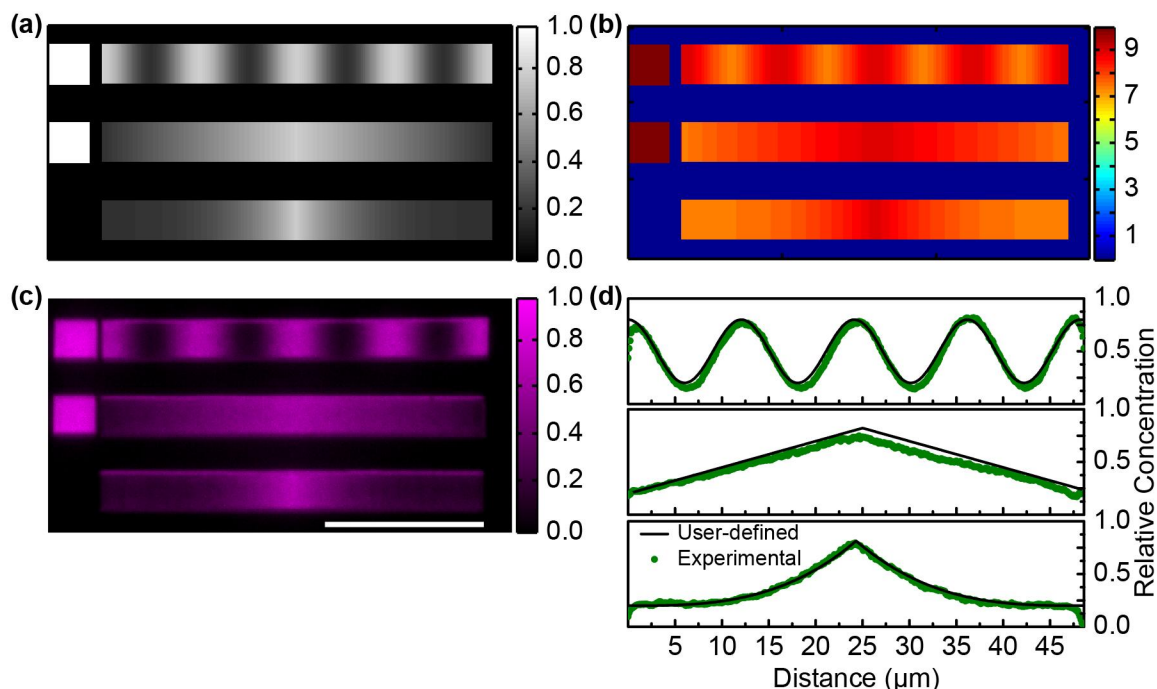


Figure 3.4.2: (a) User-defined concentration profile. (b) Map describing the power distribution as a function of position. This is obtained by following the procedures displayed in Figure 3.4.1. (c) Fluorescence image corresponding to the pattern defined in (a) and (b). (d) Plots comparing the user-defined (intended) concentration profiles against the experimentally measured values seen in (c).

designed forms vary between 0.2 and 0.8 relative values, and they have three different forms: a sinusoid, a linear carrot-top, and a cubic carrot-top. There are also a set of squares written off to the side which act as a normalizing intensity value. After being patterned, the sample is labeled with a fluorescent dye and same procedures for flattening and computing the relative intensity values described previously are used to quantitatively compare the fluorescence results with the intended profile. The results, shown in Figure 3.4.2d, compare well with the intended profiles, and variations along the profiles are smooth and measurable. This result verifies that coupling TCNL with a chemical kinetics model can design and create controlled chemical concentration profiles.

Typical results show about a 5-10% percent deviation from the intended profiles; the reason for this deviation can be attributed to the fact that there may be some small

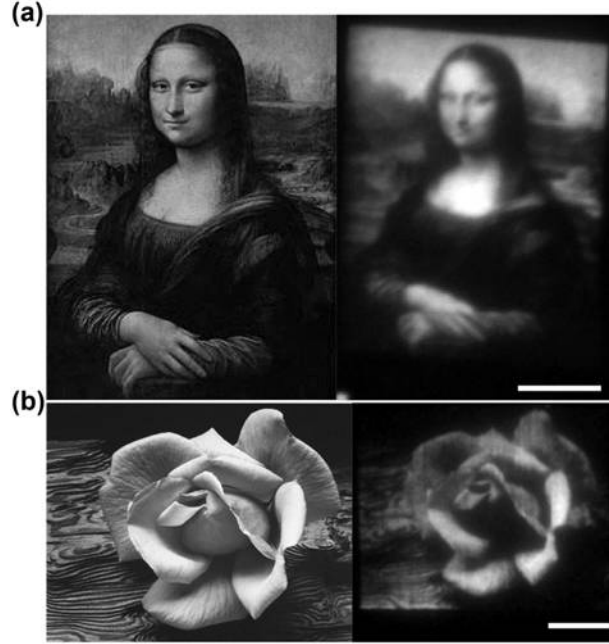


Figure 3.4.3: (a) (Left) Original *Mona Lisa* image; (Right) $\approx 30 \times 40 \mu\text{m}^2$ reproduction of the *Mona Lisa* (commonly referred to as the *Mini Lisa*). (b) (Left) *Rose and Driftwood*, 1932, photograph by Ansel Adams, copyright 2012 The Ansel Adams Publishing Rights Trust. (Right) $44 \times 34 \mu\text{m}^2$ reproduction of *Rose and Driftwood*. Scale bars are $10 \mu\text{m}$.

difference in film thickness from the calibration step to the designed patterns. The film thickness affects the peak temperature (η) because the underlying substrates thermal properties (here silicon) start to manifest at thin films. The deviations can also be attributed to the normalization value; if this is off by a small amount it can affect the range of the relative concentration results. The deviations in the normalization values likely arise from slight variations in film thickness and shot noise in the thermal cantilevers.

The results shown in Figure 3.4.2 demonstrate the ability to control concentration profiles in 1-D. Figure 3.4.3 show the ability to extend this into 2-D concentration profiles. In these cases, two images are converted from a grey scale image to a 2-D spatial power map. Instead of having the tip move continuously across the substrate, the tip remains at a pixel for a fixed period of time with the power being set by the

spatial power map. Instead of using equation 3.3, a static version backs out the peak temperature:

$$Pr = 1 - e^{-A \cdot t_d \cdot e^{\frac{-E_a}{R \cdot T_{peak}}}} \quad (3.5)$$

where Pr is the grey scale value and t_d is the fixed dwell time (here 50 ms). There should be some difference between the two methods, but since the intent is to show approximate control in 2-D, this suffices. Figure 3.4.3 shows the results of two images, da Vincis *Mona Lisa* scaled down to about $30 \times 40 \mu\text{m}^2$ and a $44 \times 34 \mu\text{m}^2$ replica of Ansel Adams' *Rose and Driftwood*. The pixel spacing is about 125 nm which is optimal for fluorescence microscopy (otherwise diffraction would blur the image too much⁴) and this 125 nm spacing is also about the FWHM measured on this polymer substrate (see section 3.3.4).

The results shown in this section demonstrate the ability to use TCNL for designing and creating controlled variations in the chemical concentration by tuning temperature. The assumptions made for producing these patterns are the same as in section 3.3.1. Interestingly, the techniques and methods described in this section can be applied to other molecules, such as proteins or DNA; however, there are differences. For example, to account for differences in binding and packing densities, the first step calibration curve needs to be done with the final attached molecule.

3.4.2 Resolution Measurements

The Full Width at Half Maximum (FWHM) determines the length scales down to which control holds, and Figure 3.4.4 shows the FWHM measurements of several lines at different temperatures. The measurements were made with an AFM using Friction Force Microscopy (FFM); FFM is capable of detecting changes in surface chemistry because the capillary interactions between the tip and substrate are enhanced or diminished depending on the surface hydrophilicity [113, 122]. In particular, amine

⁴An excellent example of this is given in chapter four.

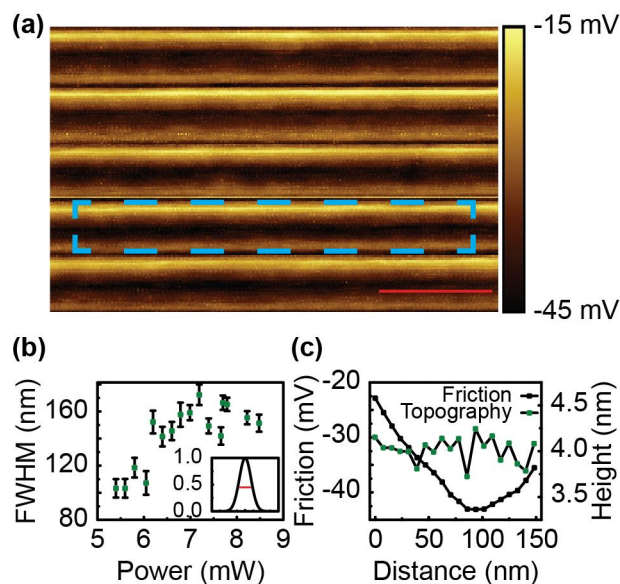


Figure 3.4.4: (a) Friction measurement of consecutive TCNL patterned lines spaced by 125 nm. Cyan square indicates the average profile shown in (c); scale bar (red) is 1 μm . (b) FWHM measured with FFM for lines written at different powers. (c) Profile showing a smooth variation of the friction signal over a topographically flat area. The friction shows a measurable change over distance of 20 nm.

exposed areas are more hydrophilic than the protected polymer [110], and the corresponding FFM measurements show an increased interaction in the patterned areas.

The measured resolution is about 150 nm, which is larger than previously reported on the same substrate [64]. The difference may arise from the film thickness: previously the films were up to 150 nm thick and the films used for this work were about 50-70 nm thick. The measurement styles were also different. Previously, bound proteins were used as the standard, but because of packing densities and efficiency loss from the multiple layers of chemistry to attach the protein, the resolution could artificially be increased.⁵ FFM is a surface technique that will exhibit a higher sensitivity.

Figure 3.4.4a shows an experiment in which the two different temperatures were written at a spacing of 125 nm. As can be seen in Figure 3.4.4c, the friction profile

⁵By resolution, we mean resolving power; increased resolution refers to smaller lengths.

shows a measureable change over distances of 20 nm. This represents the lowest bound down to which TCNL controlled reactions work. The flat region over which the friction is measured indicates that the measurements are done without having the friction convolve with the local topography.

3.4.3 Controlling Chemical Reactions with Speed

The previous section demonstrated how to control chemical concentrations by tuning temperature; this section is dedicated to showing controlled chemical concentrations realized using a spatially varying speed. The procedures for doing this are similar to those for temperature, and the main difference is the governing equation, which for speed is given by:

$$v = v_{ref} \frac{\ln(1 - Pr_{ref})}{\ln(1 - Pr)} \quad (3.6)$$

where v is the calculated speed, Pr_{ref} is a measured reference percent transformation done at fixed temperature and a reference speed, v_{ref} , and Pr is the variable percent transformation.

The first step is to select values for v_{ref} and a Pr_{ref} . The optimal choice is a $Pr_{ref} \approx 0.50$, as will be explained later. The value for v_{ref} can be any reasonable value; the value used here is 10 $\mu\text{m/s}$. A calibration plot similar to the one discussed in section 3.3.1 with the selected v_{ref} determines the eta and E_a values. The power needed for the peak temperature for the selected Pr_{ref} is computed, and using the equation 3.6, the spatial distribution of speed is computed as a function of Pr .

The results of one experiment are shown in Figure 3.4.5. The functional forms shown are a sinusoid, a line, and a step-function; the intensity normalization values are not shown. A quantitative comparison between the experimentally measured results and the intended profiles shows good agreement. The changes in the profile are both measureable and fairly smooth.

There are some differences between the intended and measured profiles. Some of

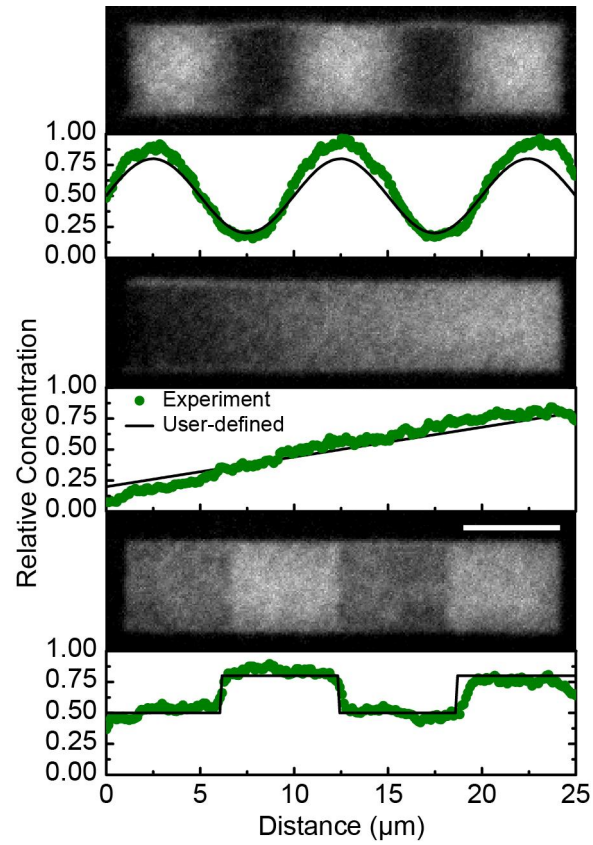


Figure 3.4.5: Experimental results showing controlled changes in chemical concentrations using variable speed. The plots indicate good agreement between the user-defined profiles and the experimentally measured values. Scale bar is 5 μm .

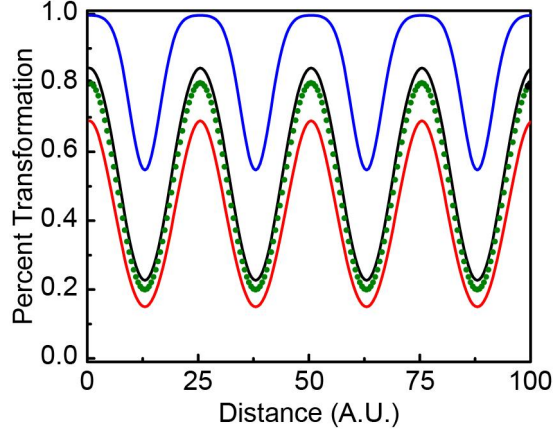


Figure 3.4.6: Plots showing how errors can be amplified in equation 3.6. See text for details.

these differences arise from the same difficulties discussed in the temperature control section, such as film thickness. Most of the differences, however, come from having an inexact Pr_{ref} value. Recalling that Pr_{ref} is a selected *measured* value, Figure 3.4.6 shows how a small deviation in the actual value for Pr_{ref} can ripple into deviations from the intended profile. For this reason, the optimal choice is a Pr_{ref} somewhere between 0.2-0.8; at too small Pr_{ref} values or values too close to 1, errors are amplified because of the nature of equation 3.6. The green scatter plot curve is the intended profile. The black indicates a theoretical curve where the measured Pr_{ref} is 0.5 but the actual Pr_{ref} is 0.55. The blue curve is the theoretical output for situations in which the measured Pr_{ref} is 0.01 but the actual Pr_{ref} is 0.035. Finally the red curve is the theoretical output for situations in which the measured Pr_{ref} is 0.99 but the actual Pr_{ref} is 0.965. The results seen in Figure 3.4.6 show that the difference between the intended curve and the theoretical measured curve is minimized for a Pr_{ref} of 0.5.

While Figure 3.4.5 shows variations in only 1-D, equation 3.6 could be used to create 2-D profiles; however, this would be rather difficult, since secondary effects such as acceleration and timing would need to be taken into account. Another option would be to use a static form of the equation as done in the temperature case; however, the

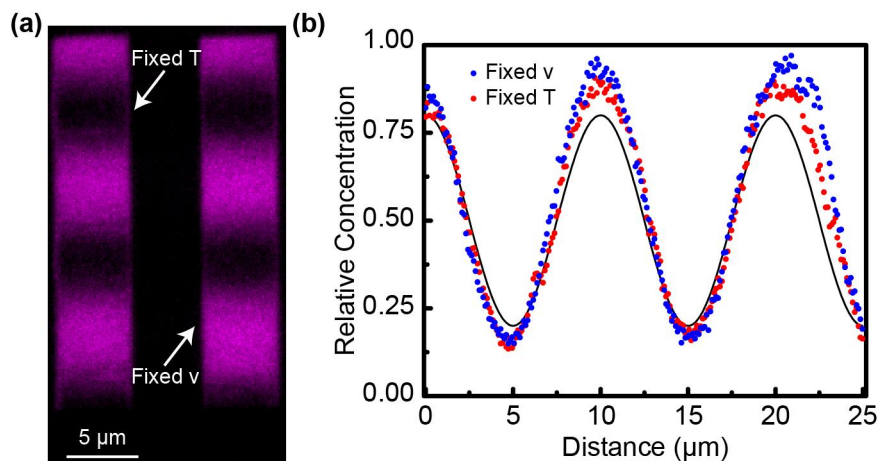


Figure 3.4.7: Comparison of fixed temperature versus fixed speed designed patterns. (a) Fluorescence image with fixed temperature on the left and fixed speed on the right. The normalization factor is not shown. (b) Plots of the intensity signals versus intended (solid line).

intent of this section is to show that speed can be used control the surface reactions, so Figure 3.4.5 suffices for this purpose.

3.4.4 Comparison of Temperature and Speed

Figure 3.4.2 and 3.4.5 show two different methods for controlling chemical reactions, and while it is instructive to ask which is better, there is no easy response to this. Both have their advantages and disadvantages. Figure 3.4.7 shows the result of a comparison between temperature controlled patterns and speed controlled patterns. Because the results are so similar, there is little conclusion to draw about which is better. The key advantage to temperature, however, is that it is easier to implement 2-D complex patterning; the key advantage for speed is that the large working range for speed (3 order of magnitude) could lead to a reduction in error if the input speed is off.

3.5 Controls

In this section, we briefly review past controls, as well as other controls done throughout this work to ensure experimental validity. Previous experiments have shown

that bulk heating of the polymer substrates and subsequent binding of fluorescent molecules demonstrated changes in the fluorescence intensity [110]. Past experiments have also shown that localized heating changes the surface chemistry; friction force microscopy (FFM) detected these changes. These controls demonstrate that the change in the fluorescence signal and the measured friction changes are likely due to the change in the polymers chemistry.

Another set of experiments showed that with no heating and application of forces between 20-300 nN demonstrated no significant change in the binding signals. This showed that the deprotection was thermally activated and not mechanical in nature. Finally, to test whether the change in fluorescence signal was inherent to the polymer or from the binding of the fluorophore, two different experiments were employed. The first measured the fluorescence signal without binding any dye; these experiments showed no measureable change in the patterned areas versus unpatterned areas. The second set of experiments labeled the substrate with a fluorophore with a different excitation and emission spectrum (N-hydroxysuccinimide ester functionalized Alexa 488, Life Technologies). The details and procedures were the same as with the DyLight 633 fluorophore. These experiments showed the same change in the signal as detected by the DyLight fluorophore.

3.6 Final Word

This chapter was dedicated to proving and verifying the model derived in chapter two. In addition, the model was applied to control chemical reactions by varying temperature and speed. The results showed good agreement, and while some effects were ignored, this shows that the chemical kinetics model describes most of the observed and intended chemical changes taking place at the polymer substrate. The truly powerful aspect about the methods and techniques developed in this section is that they are not limited to using fluorescence microscopy to measure a change in a substrate,

but rather they can be generalized to other physical or chemical properties such as the change in conductivity of graphene oxide to reduced graphene [65]. Another example is described in chapter four, where because of the chemical transformation taking place, there is a measureable physical change taking place as well.

CHAPTER IV

EXTENSION OF TCNL TO 3D

4.1 Introduction

Previous works have shown that TCNL induces chemical transformations on a substrate. In chapter three, we showed that temperature and speed can tune the amount of reaction at the surface. The ability to tune surface reactions down to near nanoscale sizes and with such accuracy holds promise for a number of different research fields (see chapter six for examples). In reality, the chemical reactions driven by TCNL are not limited to the surface, but rather occur in 3-D because the temperature profile penetrates into the surface. The transformations from TCNL extend not only along the surface but also into the body of the substrate. The penetration of the TCNL reaction into the sample (hereto referred as the z-dependence) undoubtedly leaves behind a measurable and detectable effect. For example, TCNL has been used to reduce graphene derivatives [65, 66]; the results have shown an increase in the conductivity of the patterned areas. This reduction conversion, however, measures not just the surface transformation, but also the z-dependence of TCNL (in graphene for example, there are a few layers of material).

Chapter three focused on describing and modeling how TCNL can be used to control reactions; because we attached fluorescent molecules to exposed surface amines, our measurements were confined to the surfaces and we did not develop a systematic approach to detect body effects. In reality, an understanding the 3-D effects of TCNL is quintessential for other applications that extend beyond surface patterning to 3-D lithography [55, 56] or controlling ferroelectric properties with TCNL [67, 123, 124].

Chapter three was also limited in that we relied on quantitative fluorescence microscopy to analyze and verify the chemical kinetics model, but most materials that have been used in conjunction do not always exhibit physical or chemical manifestations of TCNL induced transformations that are easily converted to fluorescence microscopy. It would be useful to develop a technique to extend the results from chapter three to other material transformations. The goal of this chapter is two-fold: 1) to go beyond surface only effects and examine the z-dependence of TCNL and 2) to develop a method to expand our analysis from relying on fluorescence microscopy. The first goal is motivated by the drive to understand and predict the effects of the TCNL process on substrates, such as graphene oxide/reduced graphene. The second goal expands the chemical kinetics model and predictions to other materials which exhibit different physical or chemical manifestations from TCNL induced reactions.

To accomplish these goals, a different organic polymer is introduced: a poly(p-phenylene vinylene) (PPV)-precursor, known as poly(p-xylylene tetrahydrothiophenium chloride)(PXT). PPV is a semi-conducting polymer which was first introduced as an organic polymer alternative for light emitting diodes (LEDs) [125]. The conversion of PXT to PPV has been demonstrated down to about 70 nm [70] using TCNL, and processing the polymer substrate can reduce this even further down to about 30 nm [59]. What makes the transformation process from the precursor film to PPV attractive as a candidate for studying 3-D effects is that the transformation leaves behind a measurable and quantitative change in the materials photoluminescence, and because the films have a certain thickness, the intensity of photoluminescence depends on how far the reaction penetrates into the sample.

This chapter is organized into four parts. The first part expands the chemical kinetics model developed in chapter two to compare surface effects with the z-dependence. The second part discusses the transformation of the precursor film to PPV. The third part semi-quantitatively shows how PPV changes as a function

of heater temperature, and we show that one of the physical manifestations of the chemical transformation is a change in the surface topography. We exploit this relationship in the last section to produce topographic gradients and to make a very rough approximation about the temperature profiles decay length into the sample.

4.2 Simulations of Chemical Kinetics in 3-D

In chapter two, an equation for TCNL induced transformations was derived for the body transformation given as:

$$Pr_{body} = \frac{N}{N_{tot}} = \frac{\int \int \int Pr(x, y, z) dx dy dz}{\int \int \int dx dy dz} \quad (4.1)$$

where Pr_{body} is the probability that the volume of interest undergoes the chemical reaction, and $Pr(x, y, z)$ is the spatial probability a single point undergoes the reaction. $Pr(x, y, z)$ is given by:

$$Pr(x, y, z) = 1 - e^{-\frac{A}{v} \cdot \int e^{\frac{-E_a}{R \cdot T(x_o|x, y, z)}} dx_o} \quad (4.2)$$

As explained in chapter two, we ignore the y -direction dependence since the distance between consecutive lines is on the order of or smaller than the FWHM. We also ignore the x dependence because we avoid edge effects.¹ With these assumptions, equation 4.1 reduces to:

$$Pr_{body} = \frac{N}{N_{tot}} = \frac{\int Pr dz}{\int dz} = \frac{\int Pr(z) dz}{L} \quad (4.3)$$

where L is the film thickness, and $Pr(z)$ is now given:

$$Pr(z) = 1 - e^{-\frac{A}{v} \cdot \int e^{\frac{-E_a}{R \cdot T(x_o|z)}} dx_o} \quad (4.4)$$

Equation 4.3 is complicated since it relies heavily on knowing the temperature profile. As discussed in chapter two, the temperature profile is difficult to compute; furthermore, even with an analytic form for the temperature profile, closed analytic forms

¹This is not the same as ignoring the x_0 integral. x_o is an integral over the tips trajectory.

for equation 4.3 are not easily computed. Instead computational forms are needed, and for simulations done below, we break the z-integral into uniform, discrete layers, and replace the above with:

$$Pr_{body} = \frac{\sum_i Pr_i(z)}{N} \quad (4.5)$$

where the summation is over the different layers (i), and N is the number of layers. To gain insight to how equation 4.5 depends on speed and z decay lengths, a temperature profile will be assumed:

$$T = (T_{peak} - T_o) \cdot e^{-\frac{|x_o|}{\lambda} - \frac{z}{\Lambda}} \quad (4.6)$$

where λ is the x decay length and Λ is the z-decay length. There are three regimes to consider: Λ equal to the film thickness (L), Λ greater than the film thickness, and Λ less than the film thickness. For these simulations, the film thickness is 50 nanometers, and each layer is assumed to be a nanometer thick.

Figure 4.2.1 shows the simulations of the surface and body transformations for three different z-decay lengths (50 nm, 100 nm, and 25 nm) and a fixed λ (100 nm) for four different speeds (1 $\mu\text{m/s}$, 10 $\mu\text{m/s}$, 100 $\mu\text{m/s}$, 1 mm/s). The first thing to note is that universally across these simulations, faster speeds show the same shift in the curve to the right that was predicted and experimentally verified in chapters two and three. To understand how the films body transforms, we want to compare it against something familiar, and since we have developed intuition in chapter two and experimental evidence in chapter three for surface reactions, we use the surface transformation as a frame of reference. Conceptually, there is a difference between the two because as is explicitly stated in equation 4.5, body effects include not just a single layer, but multiple layers. But as we will show, we can think of the body transformation not as a continuous structure, but as a set of layers undergoing an effective surface transformation at different temperature ranges dependent on the z-decay length.

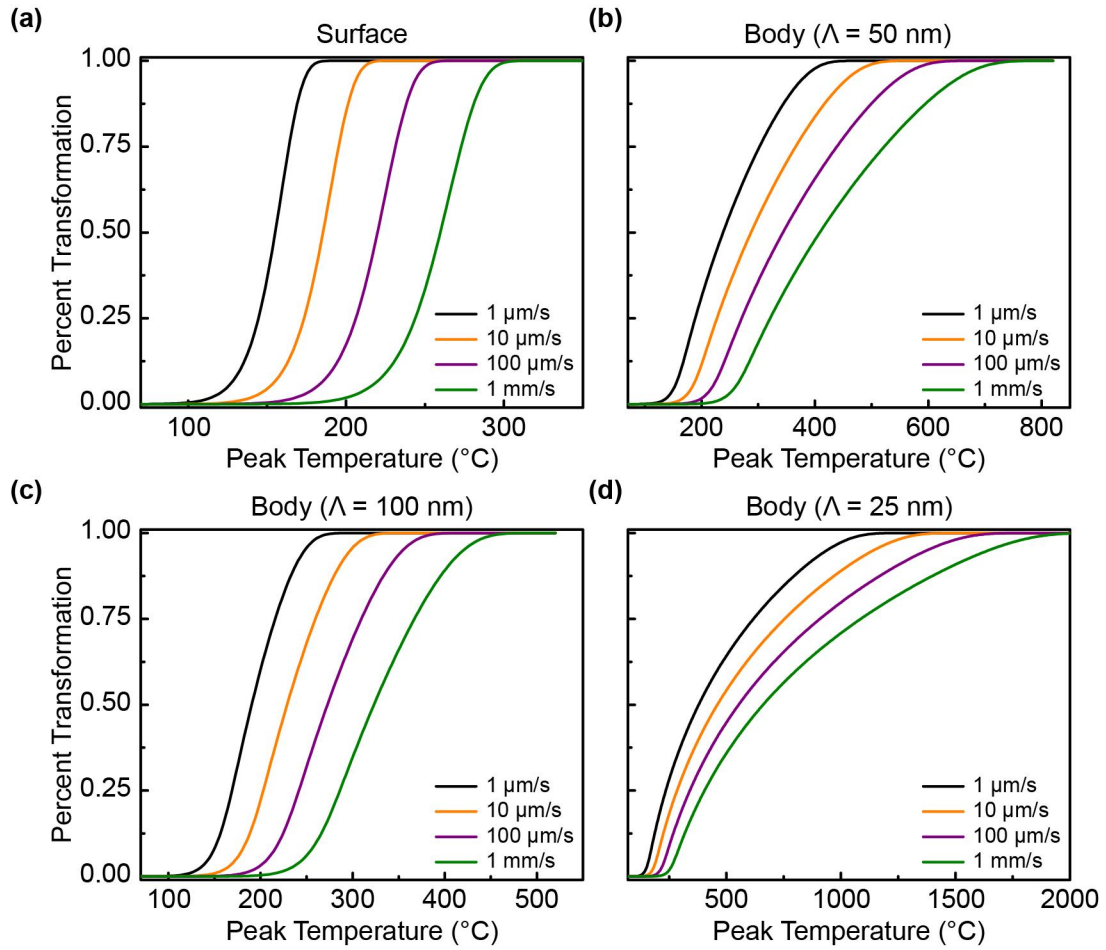


Figure 4.2.1: (a) Simulation of the surface transformation for a decay length (λ) of 100 nm for four different speeds. Simulations at four different speed for the body transformation for three different z -decay lengths: (b) $\Lambda = 50$ nm, (c) $\Lambda = 100$ nm, (d) $\Lambda = 25$ nm. The assumed film thickness is 50 nm.

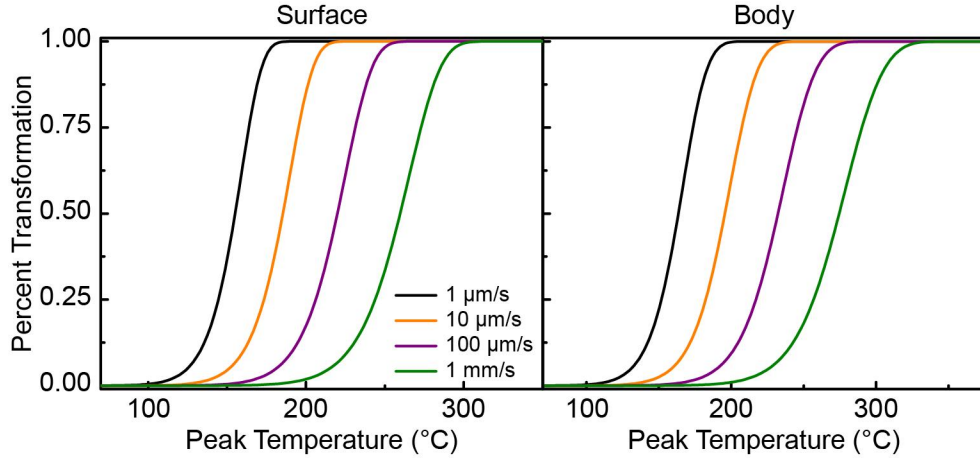


Figure 4.2.2: Simulation showing that at larger z-decay lengths ($\Lambda = 400$ nm), the body transformations temperature range starts to overlap with the surfaces transformation temperature range.

In all three cases, peak temperature required for any non-trivial percent transformation value is greater than the peak temperature for the same surface percent transformation. For example, at $10 \mu\text{m/s}$, the peak temperature for a surface percent transformation of 0.50 is about 190°C , while the body transformation requires a peak temperature of about 480°C , 300°C , and 240°C for z-decay lengths of 25 nm, 50 nm, and 100 nm respectively. Physically this comes from the decay of the temperature profile through the 50 nm thick film, and in order for the chemical transformation to occur some distance into the film, the peak temperature must be increased to compensate for this decay.

The discrepancies between the body and surface transformation temperatures start to dwindle as the z-decay length (Λ) increases. This is demonstrated in Figure 4.2.2, where a simulated z-decay length of 400 nm is shown. The differences between in the temperature ranges are minimal in comparison to those for short decay lengths, such as those shown in Figure 4.2.1d.

If Λ is decreased to the approximate spacing between layers, the conversion of individual layers can be observed. Figure 4.2.3 shows the simulation for a z-decay length of 1 nm; this decay length matches the spacing between layers. The

conversion of each layer is labeled in the figure; each layer follows an S-curve, but over different temperature ranges. The S-curve becomes exaggerated with increasing layer, the exaggerated forms account for why at short z-decay lengths (such as 25 nm in Figure 4.2.1d), the S-curve starts to skew from the sharp curves seen for larger z-decay lengths. We can approximate the required peak temperature for each layer by accounting for the decay of the temperature profile. For example, at 10 $\mu\text{m/s}$ a percent transformation of 0.50 occurs at about 190 °C, or about 170 °C above room temperature, for the surface. For the same percent transformation, the second layer requires a peak temperature of approximately:

$$T_{peak} \approx \frac{170^\circ\text{C}}{e^{-1}} \approx 460^\circ\text{C} \quad (4.7)$$

above room temperature (or 480 °C), and the third layer needs about:

$$T_{peak} \approx \frac{170^\circ\text{C}}{e^{-2}} \approx 1250^\circ\text{C} \quad (4.8)$$

above room temperature.

The above calculations based on Figure 4.2.3 can be generalized to approximate any z-decay length to:

$$\frac{T_{surface} - T_o}{T_{body} - T_o} = e^{\frac{-L}{2\lambda}} \quad (4.9)$$

where $T_{surface}$ is the approximate peak temperature at which the surface undergoes 0.50 percent transformation and T_{body} is the approximate peak temperature for which the body undergoes 0.50 percent transformation. Comparisons of equation 4.9 with the discussion for Figure 4.2.1 show good agreement.

Figure 4.2.1 to 4.2.3 and equation 4.9 tell us that what affects the conversion of the body is not the decay length, but the ratio between film thickness and the z-decay length. Equation 4.9 could also be used in reverse to determine an approximate z-decay length associated with a given material.

Finally, there may arise situations in which the transformation of the entire film in z cannot occur; this happens because the peak temperature range is outside of the

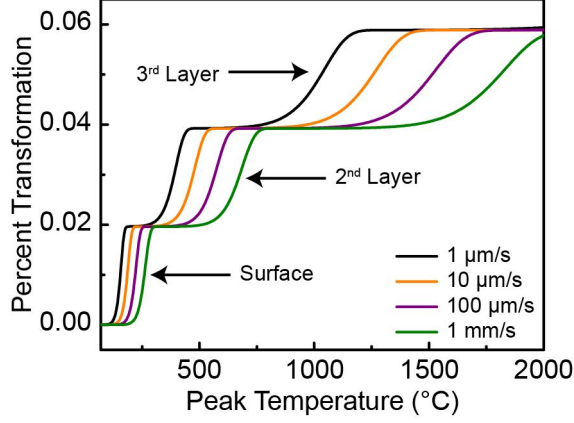


Figure 4.2.3: Simulation showing that at small z -decay lengths ($\Lambda = 1 \text{ nm}$), activation of individual layers can be observed.

operating range of the thermal cantilever, or the material starts to undergo decomposition at the necessary peak temperatures. To overcome these limitations, varying speed continuously can provide a useful expression to estimate the decay length into the sample. If we continue to assume an exponentially decaying temperature profile, there we can make an approximation based on equation 4.4. We show this by re-writing equation 4.4 as:

$$Pr(z) = 1 - e^{-\frac{k_{eff}(z)}{v}} \quad (4.10)$$

where $k_{eff}(z)$ is given by:

$$k_{eff}(z) = \int e^{\frac{-E_a}{R \cdot T(x_o|z)}} dx_o \quad (4.11)$$

Figure 4.2.4 shows plots of computed for different decay lengths ($k_{eff}(z)$ is represented as circles) and a fixed peak temperature of $220 \text{ }^\circ\text{C}$. $k_{eff}(z)$ seems to follow an exponential decay, approximated by:

$$k_{eff} \approx k_o \cdot e^{-\frac{z}{\kappa}} \quad (4.12)$$

where kappa is a new effective decay length, and k_o is related to the peak temperature through the Arrhenius equation. Fits using equation 4.12 are shown also in Figure 4.2.4 as solid lines for different z -decay lengths.

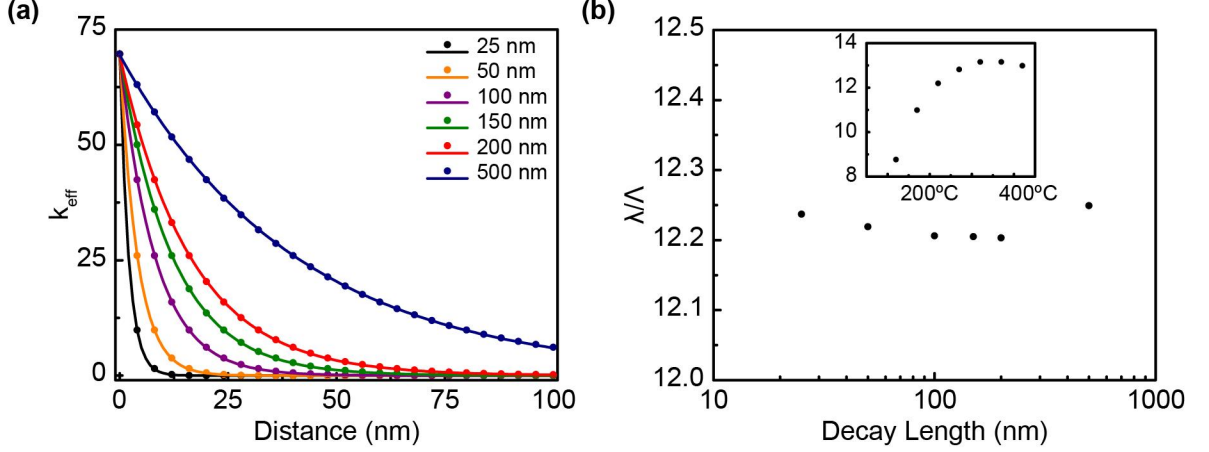


Figure 4.2.4: (a) Simulations (circles) and fits (lines) of $k_{eff}(z)$ based on equation 4.6 and equation 4.11 for six different z-decay lengths ($\Lambda = 25$ nm, 50 nm, 100 nm, 150 nm, 200 nm, and 500 nm). (b) Comparisons of the z-decay length (Λ) to the effective decay length (κ) for the same six Λ decay lengths in (a). Inset shows how this ratio change for a fix Λ of 100 nm and variable T_{peak} .

The relationship in equation 4.12 is significant for two reasons. The first is that for a given peak temperature, the ratio between the effective decay length and the z-decay length for different z-decay lengths is approximately constant (see Figure 4.2.4b). The ratios value is dependent on the peak temperature, but for our working peak temperature ranges of ≈ 120 - 420 °C, the ratio varies very little (as seen from the inset in Figure 4.2.4b, about 9-13). This narrow range for the ratio can give us an approximation for the z-decay length.

The second reason that equation 4.12 is important comes from combining equation 4.3, equation 4.10, and equation 4.12. Appendix A shows the derivation, equation 4.13 gives an analytic form for the probability:

$$Pr = \left(\text{Ei}\left(\frac{k_o}{v} e^{-\frac{L}{\kappa}}\right) + \ln\left(\frac{k_o}{v} e^{-\frac{L}{\kappa}}\right) - \text{Ei}\left(\frac{k_o}{v}\right) - \ln\left(\frac{k_o}{v}\right) \right) \cdot \frac{\kappa}{L} \quad (4.13)$$

Where Ei is the exponential integral [126, 127], given by:

$$\text{Ei} = \int_x^\infty \frac{e^{-x}}{x} dx \quad (4.14)$$

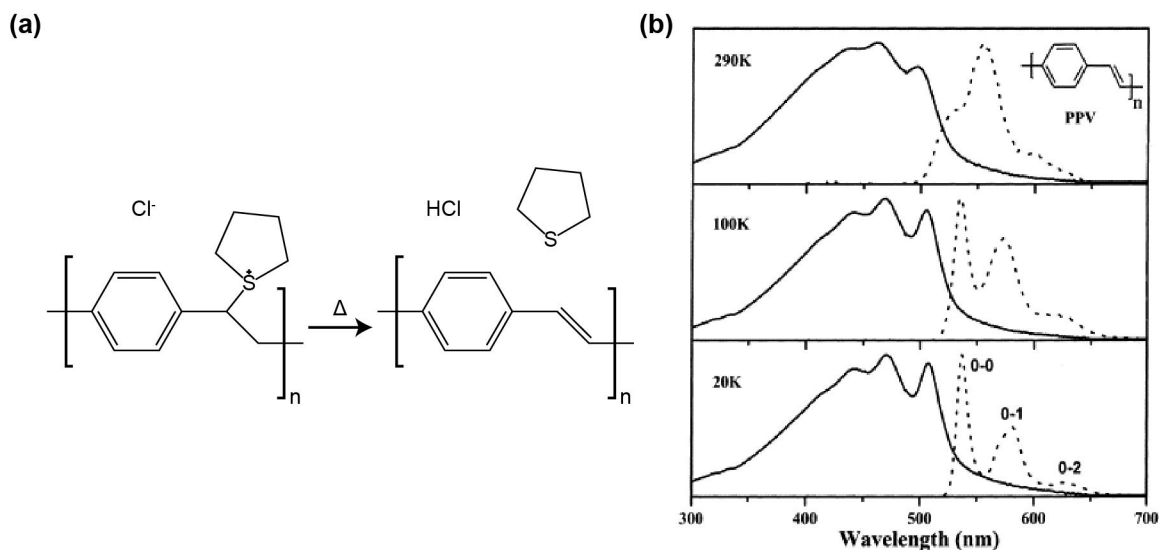


Figure 4.3.1: (a) Chemical transformation of PXT to PPV. (b) Excitation (solid line) and Emission (dashed line) of PPV.

4.3 Conversion of PXT to PPV

We use the transformation of a PPV precursor film to PPV to demonstrate some of the predictions made in the previous section. Reviewed in this section are some of the properties of PPV; substrate preparation is also discussed.

4.3.1 Chemical Transformation and Properties of PPV

The chemical transformation for PXT to PPV has been used in a number of studies. The chemical transformation is shown in Figure 4.3.1a. PXT conversion to PPV has been demonstrated with near field UV lithography methods [128], but instead, we rely on the thermal cleavage of the tetrahydrothiophene (THT) to form the organic semi-conducting polymer. According to the literature, this material follows a first order reaction (see supplemental information of reference [59]). The Arrhenius constant, A , is given by $1.67 \cdot 10^{17} \text{ s}^{-1}$ and the activation energy is measured to be 128 kJ/mol .²

There are several ways to detect that the transformation has occurred. Since PPV is a photoluminescent material and PXT is not, we can use fluorescence microscopy

²These are also the values used in the simulations in section 4.2.

to detect the transformation. The excitation/emission spectrum of PPV is shown in Figure 4.3.1b.³ For this work we use an excitation source centered around a wavelength of 480 nm and an emission filter centered around 535 nm.

Raman spectroscopy can also be used to detect the transformation of the precursor film to PPV. Measurement made in Figure 4.3.2a agree with previous observations: PPV patterns show an increased response at the 1600 cm^{-1} peak as well as an increase in the 1180 cm^{-1} peak [70]. There exist methods to quantitatively analyze Raman signals [129]; however, for this particular material, it is unclear whether these approaches apply. Figure 4.3.2b shows the photoluminescent signal from a patterned PXT film; this image was taken before Raman measurements. Figure 4.3.2c shows the same pattern after Raman measurements. There is a noticeable change in the pattern, and based on these results, we observe that Raman measurements are potentially invasive and need further analysis. Careful treatment should make quantitative measurements possible, but these are beyond the scope and intention of this thesis. Instead, we rely on photoluminescent measurements and make the assumption that the fluorescence signal is linearly proportional to the concentration of PPV. We justify this assumption by working with thin films ($<300\text{ nm}$) coupled with the fact that photoluminescence signals have been observed to be approximately linear at low concentration regimes (at higher concentrations they show non-linear effects) [130]. We also discuss how to deal with situations in which the photoluminescence signal is nonlinear to the concentration of PPV.

4.3.2 Film Preparation

Silicon substrates were cut into 1 in x 1 in squares. Select samples were sonicated for 30 minutes each in a 5 % (v/v) solution of Micro-90 detergent in deionized (DI)

³Reprinted from Chemical Physics Letter, Vol 342, Lim, S.H., Bjorklund, T.G., and Bardeen, C. J., Temperature-dependent exciton dynamics in poly(p-phenylene vinylene) measured by femtosecond transient spectroscopy, 555, Copyright (2001), with permission from Elsevier.

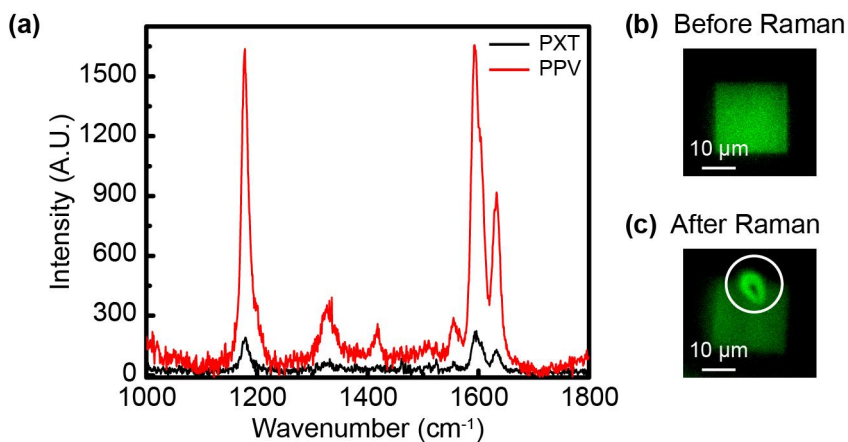


Figure 4.3.2: (a) Raman measurements indicated an increase in the 1180 cm^{-1} and 1600 cm^{-1} peaks; this indicates the transformation from PXT to PPV. (b) Fluorescence image of PPV patterns before Raman measurements. (c) Fluorescence image of the same PPV pattern after Raman measurement. The circled region indicates the invasive nature of the Raman probing laser.

water, DI water, and ethanol. These samples were then rinsed with ethanol and dried under a flow of nitrogen. All samples were then immersed in Piranha (3:1 sulfuric acid:hydrogen peroxide) for 30 minutes with a subsequent 30 minute immersion in DI water. Samples were then washed with DI water followed by ethanol and dried under a flow of nitrogen. The freshly cleaned samples were spin-coated at different speeds with a 0.25 % (PXT) in water solution to achieve the desired thicknesses. In the case of samples for Raman measurements, PPV precursor was drop-casted and allowed to dry under ambient conditions. The best results were from film thickness of about 100-300 nm which were obtained from spinning speeds of 300-625 RPM using an acceleration value of 330 rpm.

4.4 *Measurements of PXT/PPV Transformation*

To test how the photoluminescence varied with tip-surface temperature, two sets of squares were patterned on the PPV-precursor. One set was written at $1\text{ }\mu\text{m/s}$, while the other was written at $10\text{ }\mu\text{m/s}$. The heater temperature was fixed for each square pair but increased from $\approx 100\text{ }^{\circ}\text{C}$ to $550\text{ }^{\circ}\text{C}$ across the array in temperature steps of

20 °C. The experiment is depicted in Figure 4.4.1a.

Figure 4.4.1b shows the corresponding photoluminescent signal for the described experiment. Qualitatively, we observe that the signal increases with heater temperature for both speeds; this agrees with previous results [70], as well as the predictions made in section 4.2. The squares written at slower speeds show an enhanced photoluminescent response as compared to their higher speed counterparts. This agrees with the shift of the S-curve to the right as mentioned in section 4.2.

Semi-quantitative measurements are shown in Figure 4.4.1c. The processing is similar to that discussed in chapter three. Background images corrected for any uneven illumination. The key difference between the analysis here and that done in chapter three is that here the plotted intensities, I , are not normalized, but instead are given by:

$$I = I_{measured} - I_{background} \quad (4.15)$$

where $I_{measured}$ is the average intensity of a square and $I_{background}$ is an average background intensity levels. The normalization factor was removed to prevent any misconception that a 1 value represented full conversion. Here, I represents more than just the surface effects we measured in chapter three, but also the effects of the entire body since the z-resolution of the microscope is larger than the film thickness (even methods such as TIRF or confocal microscopy will not work for these film thicknesses around 100 nm [131, 132]).

The plots shown in Figure 4.4.1c show that as the heat temperature increases, the photoluminescent signal increases slowly at first, and then it appears to increase at an approximately linear rate at a heater temperature of about 400 °C. At first glance, these trends do not seem to agree with the discussion in section 4.2; however, close inspection of Figure 4.4.1d, which is a zoomed in version of Figure 4.2.1d, shows that for small peak temperatures, the simulations are similar to those seen in Figure 4.4.1c. These results are suggestive that the temperature profile is not penetrating

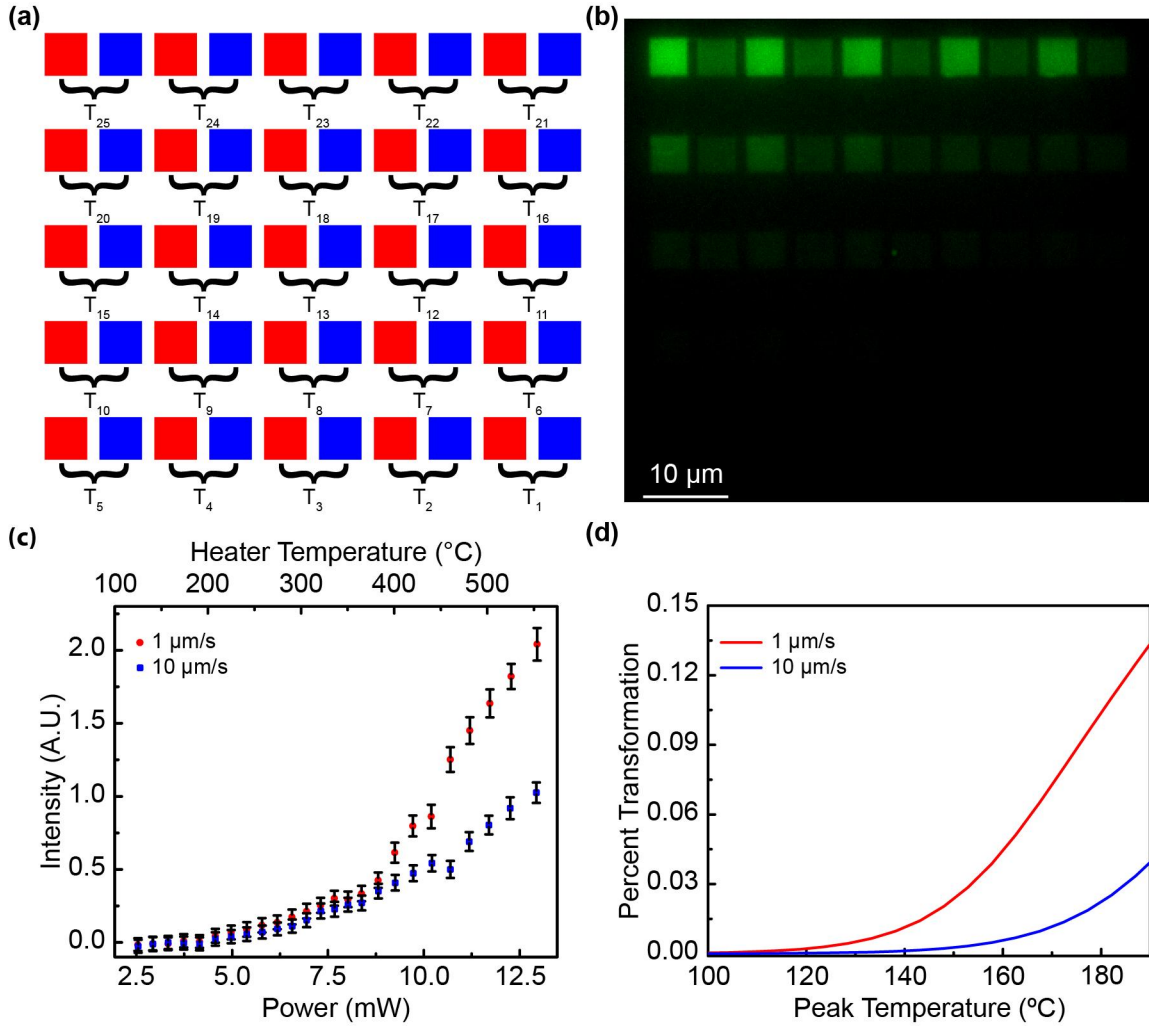


Figure 4.4.1: (a) Experimental schematic for the measuring the change in the photoluminescence signal with changing heater temperature. Red squares indicate patterns written at 1 $\mu\text{m/s}$, while blue squares are at 10 $\mu\text{m/s}$. (b) Photoluminescent image of the pattern corresponding to the experiment in (a). (c) Semi-quantitative measurements of the signals in (b). (d) Zoomed in version of Figure 4.2.1 (d) to indicate that at low peak temperatures, the data forms agree. ($\Lambda = 25 \text{ nm}$, film thickness = 50 nm).

far enough into the sample to transform the entire film.

The results shown in Figure 4.4.1 are suggestive that a chemical kinetics model applies, but in order to provide additional evidence, we want to show other predictions made in section 4.2 are also true. One of the key observations reported in section 4.2 is that the surface undergoes the transformation before the film body does. In chapter three, we discussed how FFM can detect changes in a substrates chemistry. Specifically, FFM is capable of detecting changes in hydrophilicity/hydrophobicity because of the change in capillary forces at the tip-substrate interface [113, 122]. Comparisons of the pre-cursor chemical structure to PPVs chemical structure suggest the pre-cursor is more hydrophilic than PPV. FFM should be able to detect this change, and by its very nature as a surface technique, it would only measure the surfaces transformation. The results of an experiment in which the heater temperature was varied across an array of squares is shown in Figure 4.4.2. While the exact relationship between the measured friction signals and the concentration of PPV to PXT is not known, certain things should be expected. At low concentrations of PPV the friction signal should be approximately the same as the precursor film; at higher temperatures, once the local surface has been fully converted, the friction signals should level off to measure a fixed PPV only signal. Figure 4.4.2 shows how the friction signal varies with heater temperature; the trend in the FFM agrees with our discussed prediction in the friction signal. At lower temperatures, the friction signal is not much different than the precursor, while at higher temperatures, the patterns show a contrast in the friction signal from the substrate. Plots of the friction signal versus heater temperature show that the friction signals plateau above a heater temperature of 400 °C.⁴ While the data is noisy, we interpret the leveling off as indication that the surface has fully undergone the reaction.

⁴This heater temperature should not be confused with the previous heater temperature of 400 °C for Figure 4.4.1; these experiments were done on separate films and with different tips.

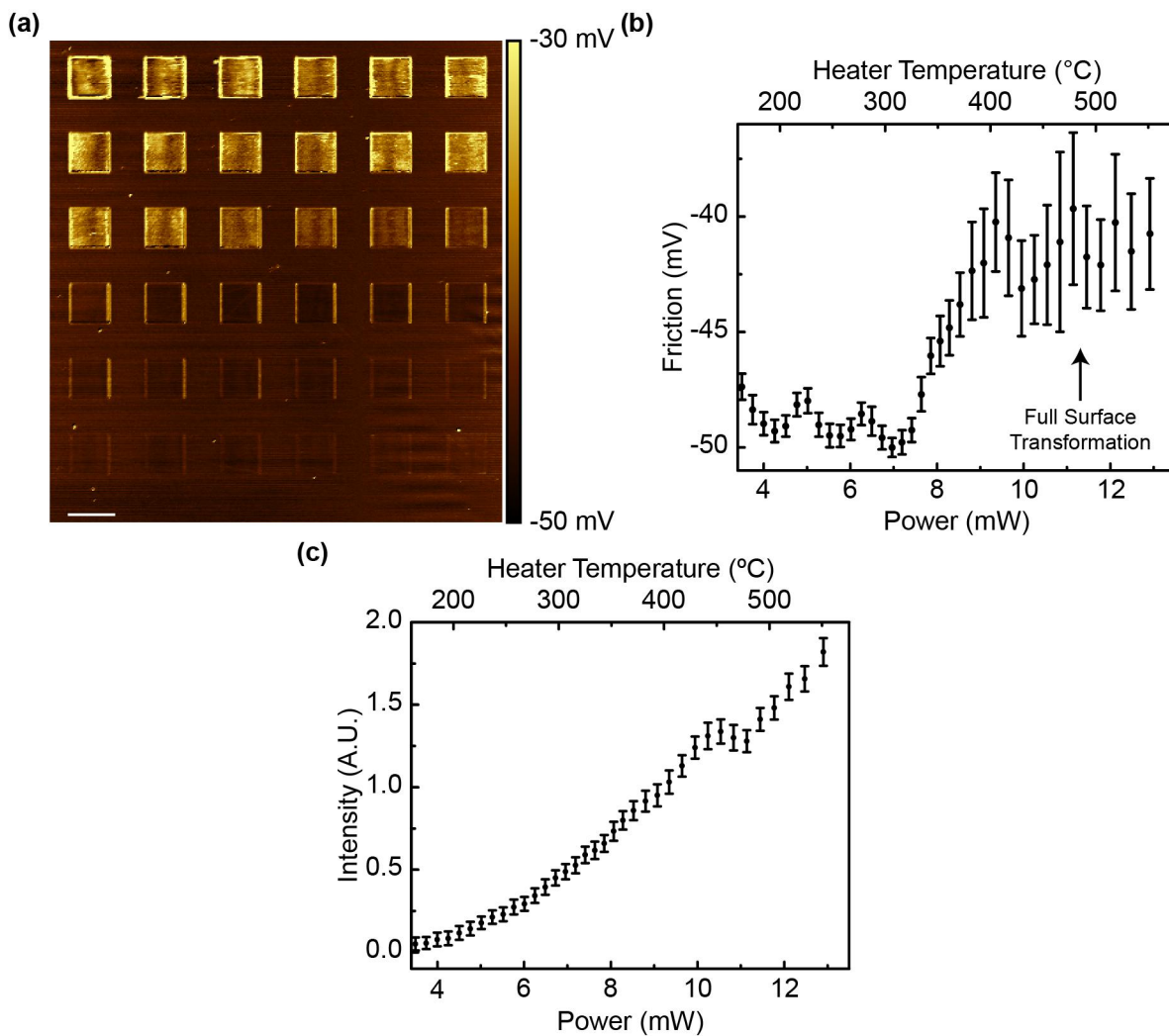


Figure 4.4.2: (a) Friction measurement for a series of squares written at heater temperatures of $\approx 150^\circ\text{C}$ up to $\approx 550^\circ\text{C}$. (b) Plots of the friction signal versus heater temperature seen in (a). Above 400°C the friction signal is seen to level off; this is indicative the surface transformation has completely taken place. (c) Plot of the fluorescence signal for the pattern in (a). The signal continues to increase pass the 400°C heater temperature; this suggests the body has not undergone the complete transformation, while the surface has.

Comparing the results against the patterns photoluminescent signals show that the signal is still increasing past a heater temperature of 400 °C (Figure 4.4.2c). This suggests that the entire film has not undergone the reaction, but the *surface* has.

AFM measurements also indicate that when the precursor undergoes the transformation to PPV from a localized temperature profile, the patterned areas show a reproducible change in the surface topography. Figure 4.4.3 shows an example in which an array of squares at increasing temperatures was thermally patterned. Figure 4.4.3a shows that for low temperatures, the drop in topography is smaller when compared to the drop at higher temperatures. The measured depth drop in topography ranges for this sample from about 2 nm to about 30 nm. While it is tempting to relate the change in topography to the loss of the side group from the chemical reaction, there is no direct evidence to prove that this is the only cause of the change in topography. This change in topography has been observed previously, and it is suggested in the literature that this drop may come from polymer confinement [59] or from the loss of water and the THT side chain [59, 133]. This shrinking results from the polymer being able to closely pack on itself. It is likely that the drop in topography results from a combination of loss of side group and polymer shrinking.

Figure 4.4.3b shows the fluorescence images of the patterned areas, and again, we observe the intensity increasing with heater temperature. There are similar trends between the change in topography and the change in intensity: as the heater temperature goes up, the resulting change is amplified. Plotting the two values against each other reveals a close to linear relationship between the measured depth profile and the intensity signal. To compare the two signals, the surface height is measured with an inscribed square and the difference is averaged between unpatterned to the left and the right of the square. The averaging is done to reduce possible artifact introduced from the large scan range of the image [134, 135]. The intensity signals undergo the same processing as described above. The relationship between the topography change

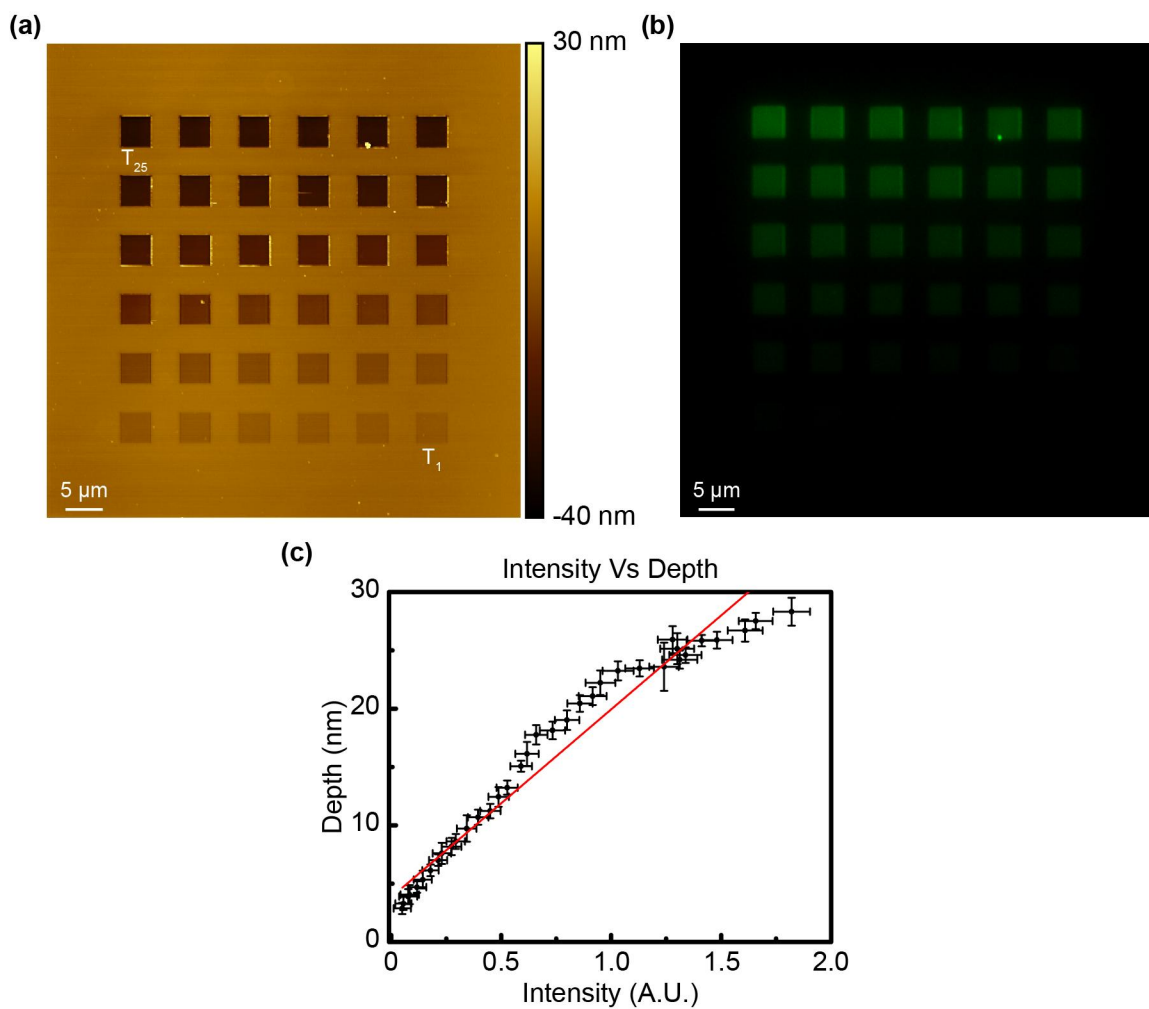


Figure 4.4.3: (a) AFM measurements of squares patterned into PPV. The heater temperature range is $T_1 \approx 160^\circ\text{C}$ (lower right) up to $T_{25} \approx 550^\circ\text{C}$ (upper left). (b) Fluorescence signal of the pattern in (a). (c) Comparison of the change in PPV height (depth) (a) versus the intensity signal in (b). The two are approximately linear.

and the intensity signal is close to linear as seen in Figure 4.4.3c.

The above analysis suggests the change in height is linear to the photoluminescence, and because we have assumed the photoluminescence is linear to the chemical change, this implies that the change in height to be linear with the chemical transformation. By measuring the change in topography to the something comparable to the change in PPV concentration, we have essentially measured another physically parameter with which we can gauge the reaction process. For other systems, the relationship between the new parameter and the reaction need not necessarily be linear, but as long as there is a measureable or theoretically computed relationship between the concentration and a measureable parameter, the analysis developed in this and the previous chapters hold.

4.5 Using Topography to Demonstrate Extensions of TCNL

One of the goals we set out for this chapter was to use other physical parameters to measure the chemical kinetics model. FFM measurements and the correlation between the height and the intensity demonstrate two techniques which show measureable changes in the substrate chemistry. In particular, FFM measured qualitatively demonstrated the full conversion of the surface chemistry, while topographic measured the effect through the entire film. Figure 4.4.3 related the topography changes to the photoluminescence, and since our assumption was that photoluminescence is linearly related to the concentration of PPV, we can now assume the height is also linear to the PPV concentration. If other measurements indicate that photoluminescence followed some other functional dependence on PPV concentration, the height could still be used as a gauge for the reaction by composing the PPV-Photoluminescence dependence with the linear relationship between height and photoluminescence. This section takes advantage of the observed linear height-photoluminescence relationship and the new linear PPV reaction to height relationship to demonstrate two concepts:

1) the proof of TCNLs control down to the nano-scale and 2) to approximate the z-decay length.

4.5.1 Nano-Scale Control

The results shown in chapter three for surface reactions show a nice predictable way to create and design patterns. As mentioned in chapter three, we could not reproducibly alter topographic variations in the cinnamate polymer, and therefore we relied on fluorescence microscopy to analyze our data. Fluorescence microscopy, however, is diffraction limited, and because of this limitation, it is tough to scale the relationships down to the nano-scale without resorting to super-resolution techniques [131, 136]. For example, even though the pixels for the *Mona Lisa* depiction are spaced by 125 nm, for our current setup, there is no *easy* way to show that the model accurately predicted each pixel or if the point spread function [137] of the microscope effectively averaged the pixels to produce an approximately correct image.

PPV overcomes this requirement because the reproducible relationship between the change in height and the photoluminescence allows us to go beyond the diffraction limit by measuring the substrate with an AFM. An example of the improved imaging quality is shown in Figure 4.5.1 where another reproduction of the *Mona Lisa* down to $\approx 30 \mu\text{m} \times 40 \mu\text{m}$ is shown in PPV. The two key differences between this reproduction and the previous is that this is achieved empirically (hence why we show applied voltage instead of power), and rather than a pixel by pixel fabrication, the images seen here are fabricated with the tip moving continuously. Figure 4.5.2b shows the fluorescence image; the results show a similar diffraction limited reproduction of the *Mona Lisa* to that seen in Figure 3.4.3. Figure 4.5.1c shows the corresponding AFM image, and the extra detail not present in the fluorescence image can be seen with the higher resolution AFM image. This result demonstrates that control of the chemical transformation continues down to the nano-scale (here the pixel resolution is ≈ 78

nm). Figure 4.5.1d shows the FFM measurement of the same pattern; this result is only qualitatively, and should not be interpreted quantitatively as we did with the squares because the rapidly varying topography prevents the friction signals accuracy.

To push the limits of this, a smaller version ($\approx 20 \mu\text{m} \times 33 \mu\text{m}$) is shown in Figure 4.5.2. The pixel spacing was about 60 nm, and the topography reveals the same amount of detail as seen in Figure 4.5.1. The fluorescence image seen in Figure 4.5.2b, however, suffers further from diffraction, and the *Mona Lisa* blurs more, though it is still decipherable.

The pixel resolution ($\approx 60 \text{ nm}$) shown in Figure 4.5.2 is slightly lower than previously measured FWHM of lines ($\approx 70 \text{ nm}$). Since the sample preparation was different for these two studies, a series of lines were written at different heater temperatures (see Figure 4.5.3). The measured resolutions are slightly above 60 nm, and agree with previous results. The measured FWHM suggest that if the *Mona Lisa* were shrunk even further, one would expect to start seeing the topography image blur. Figure 4.5.2 is approaching those length scales, and it would be instructive to know if the length scales for blurring are different from the FWHM. This type of study could suggest that the FWHM is not an appropriate measure for the resolution, but we leave this for future work.

4.5.2 Z-Dependence

Figure 4.4.1 and Figure 4.4.3 show that the depth and photoluminescent signals continue to increase with increasing temperature. The results from section 4.2 are suggestive that under appropriate conditions an S-curve should manifest. Those conditions are that the peak surface temperature reaches a high enough temperature to penetrate through the entire thickness to thermally induce a chemical reaction throughout the film. The thermal cantilevers, however, have certain limitations; for example their optimal working range is below the thermal runaway ($\approx 600 \text{ }^\circ\text{C}$) [51]. Clearly the heater

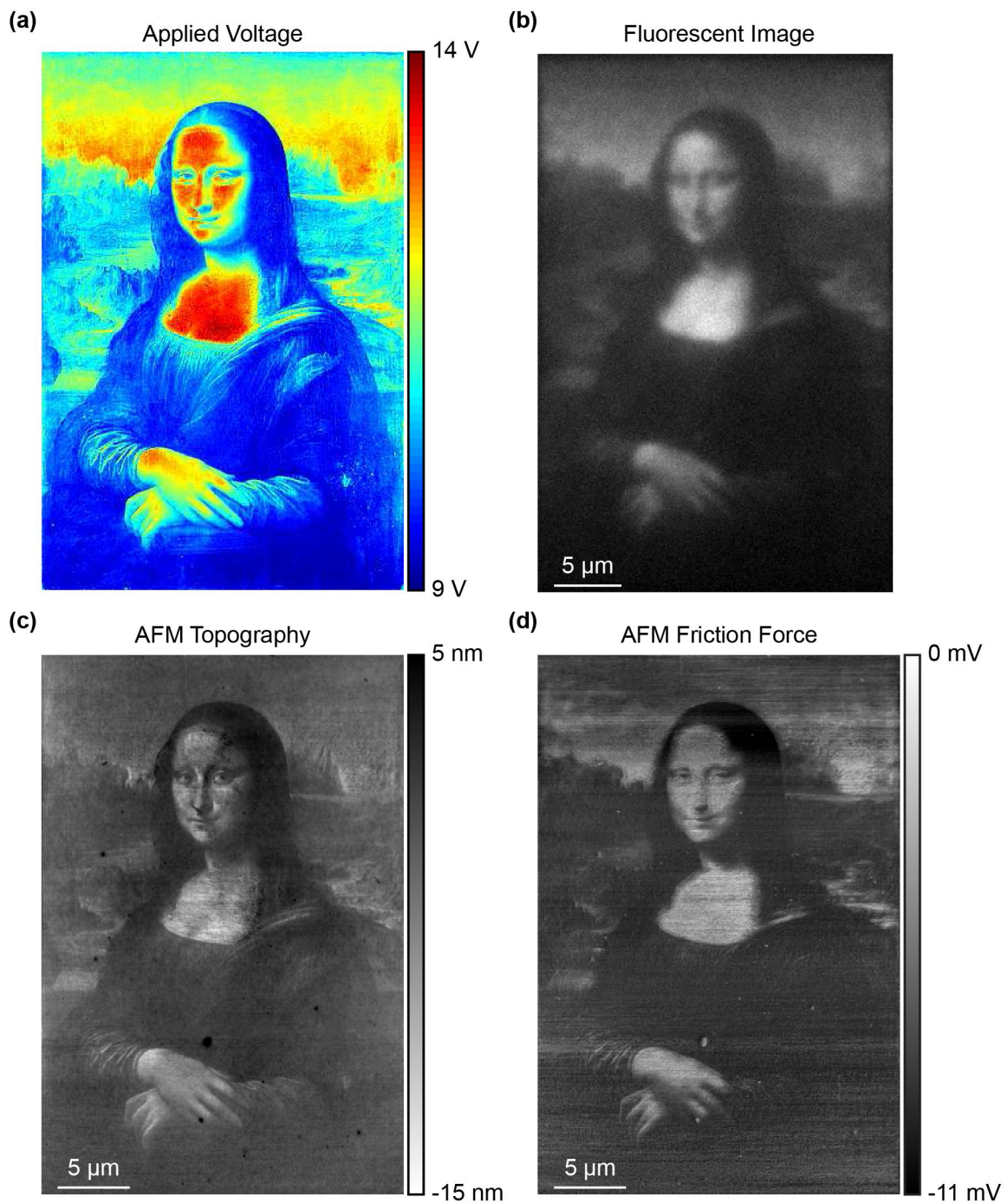


Figure 4.5.1: (a) Spatial distribution of applied voltage to create a 30 μm x 40 μm reproduction of the *Mona Lisa*. (b) Fluorescence image of the patterned PPV. (c) AFM image of the patterned PXT/PPV film. Diffraction in (b) limits our ability to see the added details. (d) FFM measurements that qualitatively detail the reproduction.

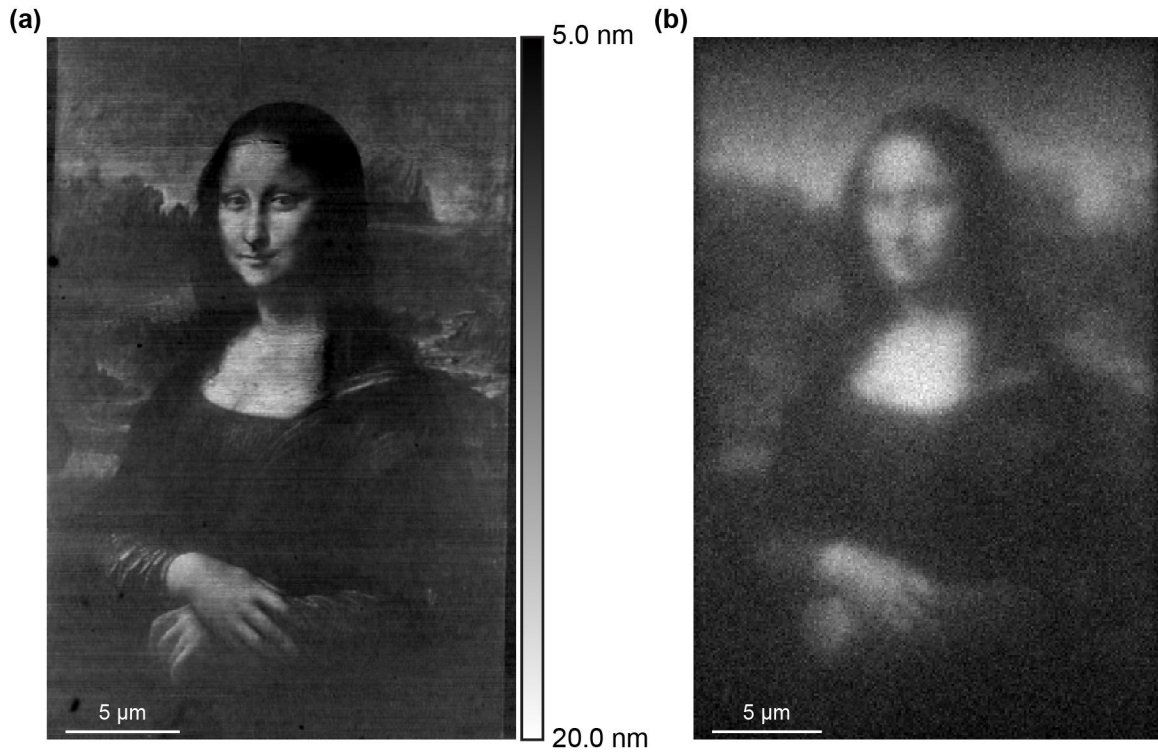


Figure 4.5.2: (a) AFM image showing $\approx 20 \mu\text{m} \times 33 \mu\text{m}$ reproduction of the *Mona Lisa* in PXT/PPV film (*Mona Lisa 2.0*). (b) Fluorescence image corresponding to the pattern in (a). Diffraction makes the image look blurry as compared with the high resolution AFM image.

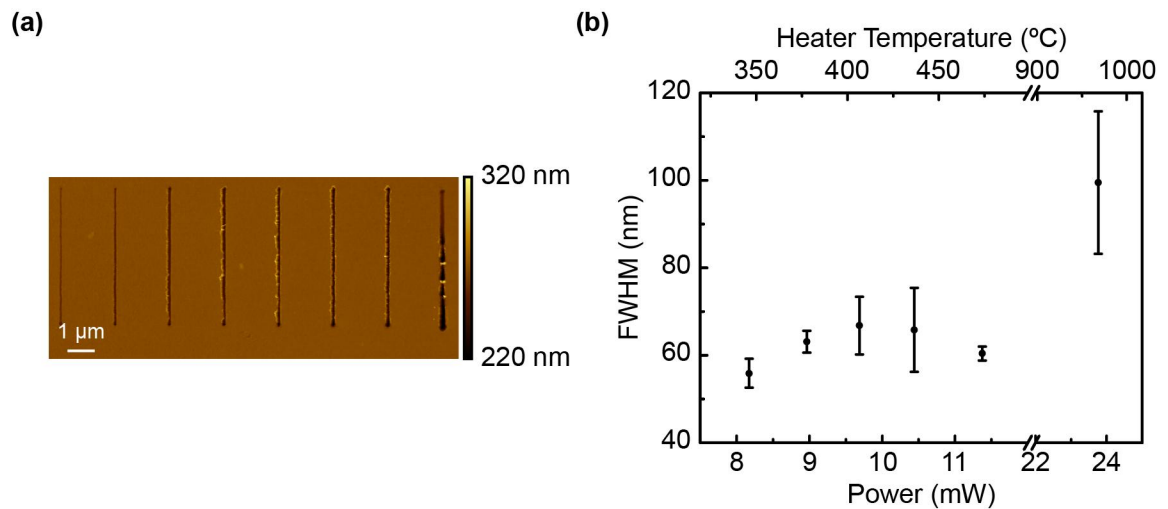


Figure 4.5.3: Measurements of FWHM of lines made in PXT/PPV film (a) AFM image of lines at different temperatures. (b) Measurements of the FWHM as a function of power and heater temperature.

temperature cannot reach temperatures of 2000 °C since the melting temperature of silicon is about 1500 °C [138]; as a result, the tip-surface interface temperatures cannot approach those values (recall that the tip-surface temperature is less than the heater temperature [69, 109] as described in section 3.2.2). The limitations on the thermal cantilever may hinder the ability to induce the reaction throughout the entire film.

It is instructive to wonder to which depths the reaction does penetrate. The relationships developed in section 4.2 can at least suggest an approximate answer; specifically, using the relationship developed for the z-decay length and the effective decay length from equation 4.12 and equation 4.13. Figure 4.5.4a shows the experimental setup for measuring the z-decay length. Each rectangle is run at a fixed temperature, and as the tip continues up the pattern, the tips speed decays exponential. Figure 4.5.4b shows the resulting AFM image corresponding to the experiment in Figure 4.5.4a. The topographic profiles show that at low speeds, the change in topography is greater than at fast speeds. This relationship agrees with the chemical kinetics model and the results seen in section 4.2. Figure 4.5.4c shows the corresponding plot of the fluorescence image (shown as an inset) of the patterned PPV. The signals indicate the same trend discussed for the drop in height.

Comparing the fluorescence image with equation 4.13 is difficult since diffraction makes edge detection difficult. Instead, the AFM data will act as a substitute since edge detection will not be such an issue. The normalized values are compared against a normalized version of equation 4.13. The normalized depth values come from:

$$H_{rel} = |H_{pattern} - H_{surface}| \quad (4.16)$$

where H_{rel} is the absolute relative depth, $H_{pattern}$ is the profile of the pattern (red line in Figure 4.5.4b), and $H_{surface}$ is the average profile of the surface (average of the blue lines in Figure 4.5.4b). Finally, the absolute depth values are normalized by the maximal depth value.

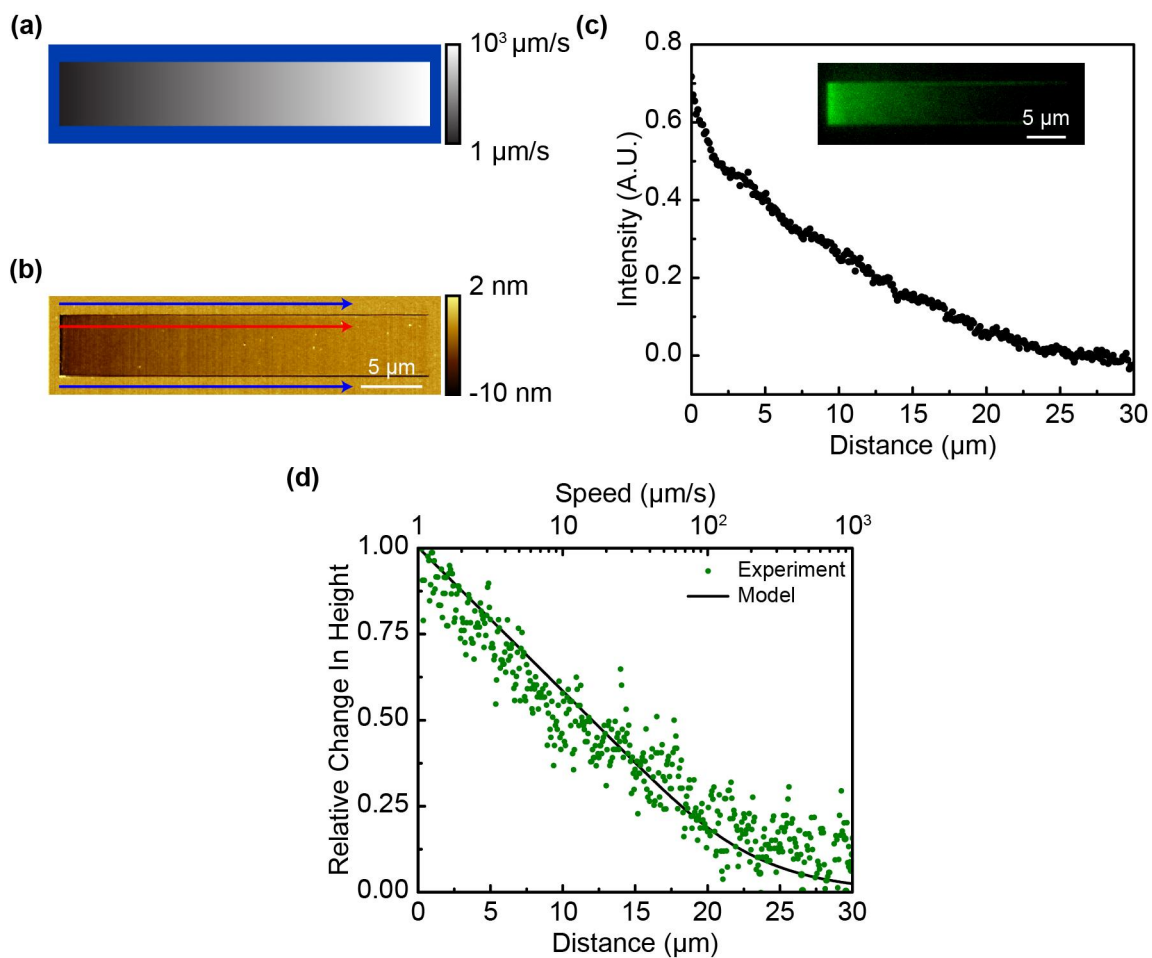


Figure 4.5.4: (a) Schematic showing an experiment in which the heater temperature is kept constant and the speed is varied as a function of position. (b) AFM image corresponding to the experiment in (a). (c) Plot of the fluorescence signal of the PXT/PPV pattern. (d) Fit of equation 4.13 with experimental results in (b). The measured effective decay length is ≈ 3.0 ; we approximate the temperature decay length as $\approx 40 \text{ nm}$.

Figure 4.5.4d shows the comparison between the measured AFM profiles and equation 4.13. The measured effective decay length is about 3 (2.96). Assuming the decay length is approximately 13 times larger than the effective decay length, the temperature decay length in the z-direction is approximately 40 nm. Given that the film thickness is about 100 nm for this substrate, in order for the transformation to fully penetrate through the entire sample, the peak temperature range needs to scale up to approximately 2500 °C! This is well beyond the optimal working range of the thermal cantilevers. This result suggests that the reason we never obtained the full S-curve is that the temperature decays too rapidly into the sample. This result, however, needs to be taken with some care. The fits from equation 4.13 are not that good, but this result does at least agree with our previously discussed experimental results. This is an on-going study, but the fact that the approximate z-decay length is also near the measured FWHM hints that at least this value is in the same range as the lateral decay.

4.6 Final Word

In this chapter, we set out to extend TCNL beyond the limitations of measuring surface reactions and started to make some observations on the penetration of the chemical reaction into the sample. We strived to define a methodical way to relate a physical manifestation of a chemical reaction into quantitative information about the chemical transformation rather than rely directly on fluorescence. Even though we assumed that the photoluminescence signal of PPV is linearly proportional to the PPV concentration, we described how to overcome any complications introduced if this assumption failed after some point. We also showed a unique method for creating topographic gradients and demonstrated control down to the nano-scale. The long term impacts of this chapter are describing the translation from one physically measureable parameter to a chemical concentration and using that new relationship

to show other features of TCNL and the chemical kinetics model.

CHAPTER V

PARALLELIZATION OF TCNL

5.1 Introduction

Essential to the development of any lithographic technique for research and industrial applications is the ability to implement high-throughput patterning. In particular, SPM techniques have garnered significant focus and have made impressive advancements towards parallelization; parallelization here refers to any process which implements simultaneous use of multiple SPM probes with a single instrument. The emphasis on parallelization of SPM techniques derives from the fact that many SPM techniques are capable of achieving nano-scale resolutions but many are slow [139].

Parallelization of SPM techniques, however, introduces two major complications: the ability to read and to write. Traditionally, AFM techniques use an optical feedback for measuring surface properties, but parallelizing optical feedback would be tedious and grow in complexity with larger numbers of tips in use. A number of unique and interesting solutions have been developed to remove traditional optical feedback requirement; such solutions have included complementary metal oxide semiconducting (CMOS) technologies employing piezo-resistive/strain effects [140, 141], interferometric optical measurements [142], or thermal interactions between a thermal cantilever and a substrate [53]. There have also been some attempts to control individual cantilever actuation through contrasting thermal expansion coefficients [143], an effect often referred to in the literature as the bi-morphic effect.¹

¹The bi-morphic effect also appears in the thermal cantilever used in TCNL, but in a less controlled manner.

While many techniques have focused on reading and measuring surfaces, the ability to parallel write is relatively infantile in its development compared with the advancements made for single tips. There have been limited attempts for SPM based patterning parallelization. Parallelization of 50 tips produced 100 mm² patterned areas with electro-oxidizing lines in a silicon substrate [144]. DipPen Nanolithography (DPN) has employed the use of both passive and active cantilever arrays, which use the bimorphic effect to lift individual tips off the substrate [145]. The DPN community has also introduced 55,000 parallel cantilevers to pattern substrates down to 80 nm [50]. Thermo-mechanical lithography is of particular fame because of the IBM millipede, where near 1000 cantilevers were brought into contact with a polymer substrate and actively used to indent a surface with high resolution [52]. The "millipede" work was not limited to patterning, but also extended to imaging; moreover, that work introduced a cheaper alternative to the traditional expensive piezo-scanner [52].

This chapter is dedicated to the description and implementation of thermal cantilever arrays for TCNL parallelization. The focus is more on the implementation, as opposed to the more exact treatment in previous chapters. As with all SPM techniques, parallelization of TCNL still requires the ability to read and write; the ability to read is well described for thermal cantilevers throughout the literature, but it is briefly reviewed and demonstrated here. Most of this chapter, however, is focused on parallelization of TCNL patterning.

5.2 Description of Thermal Arrays

The thermal arrays are composed of 5 tips as seen in Figure 5.2.1. All arrays were fabricated by the Professor William P. King's lab at the University of Illinois at Urbana Champaign. For convenience, the tips are numbered 1-5. Each tip is individually addressable which means that tip 1 can be heated to one temperature while tips 2-5

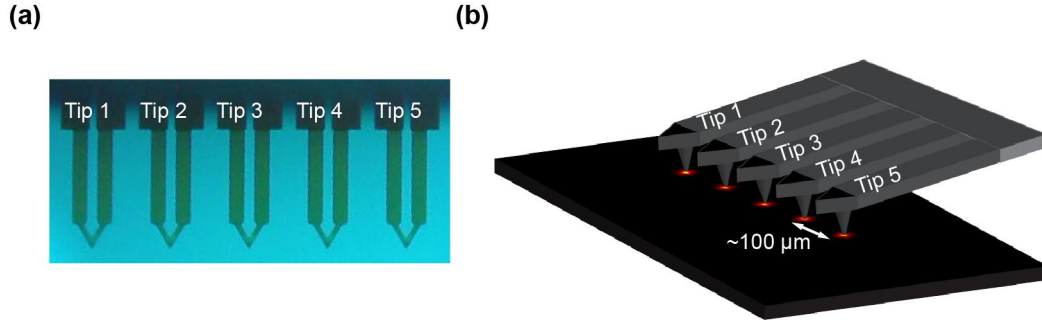


Figure 5.2.1: (a) Optical image of thermal cantilever array with numbering. (b) Schematic showing a thermal cantilever array inducing a temperature profile in a substrate.

are each maintained at different, unique temperatures. The electronic and thermal responses of the tips are the same as those described in chapter three for a single cantilever. Since the arrays are manufactured simultaneously and under the same conditions, the thermal runaway point is similar for all five cantilevers [146].

5.3 Leveling

Arrays present an additional challenge not present with a single cantilever: leveling. With multiple tips, it is important to ensure all the tips are brought into contact with the surface simultaneously. By measuring the interaction between the thermal tips and a substrate, the arrays can externally be aligned with a substrate. To demonstrate these thermal interactions, we start with a single tip.

5.3.1 Interaction between a Thermal Tip and a Substrate

Analogous to other AFM modes, thermal cantilevers interact more with a substrate as distance between the tip and substrate decreases. For thermal cantilevers, some of interactions result from the increased air conduction between the cantilever legs and the substrate. As the gap between the tip and substrate decreases, there is a greater flux of heat out of the thermal cantilevers legs causing the integrated heaters temperature to go down (hereto referred to as the "cooling" effect). This effect is well reported [92, 147]. The substrate induced cooling leads to a measurable

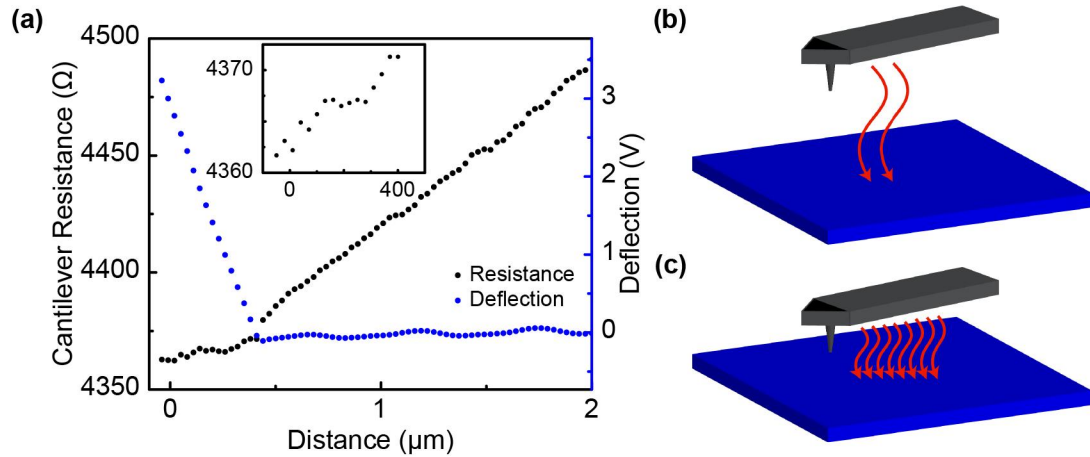


Figure 5.3.1: (a) Resistance measurement as a thermal tip is brought into contact with a surface; also shown in blue is the optical measured force displacement curve. (b) and (c) Schematics showing that at far distance from a substrate (a) the thermal cantilever transfers less heat than close to the surface (b).

change in the thermal cantilevers electronic properties since they are closely connected to temperature (see discussion in chapter three). Although there have been other suggested routes, we measure this electronic change through the cantilevers electrical resistance for this work. An example and schematic are displayed in Figure 5.3.1.

Figure 5.3.1a shows a force displacement curve [148] and the cantilevers change in resistance as a function of z -position. The resistance monotonically decreases as the tip approaches contact with the substrate; Figure 5.3.1b and c show a schematic of this process. Far from the substrate, there is less heat transfer between the cantilever and the substrate, resulting in a higher temperature; these higher temperatures cause a larger resistance. As the tip is lowered, there is a greater heat flux out of the cantilevers legs, and this leads to a lower temperature and a lower resistance [147]. Once contact is reached between the tip and the substrate (as indicated through the blue force-displacement curve), the inset to Figure 5.3.1 indicates that the resistance continues to decrease monotonically, but at a slower rate. It is likely that this comes from the fact that even though the tip is in contact with the surface, the cantilever legs still approach the surface both as a result of cantilevers increased bending and

the elastic response of the surface [149].

5.3.2 Array Leveling

Coupling the "cooling" effect with a leveling device alleviates this issue. An optical leveling mount was integrated with the AFM to tilt the substrate in order to level the tips. The cooling effect indicates and measures which tips first contact the substrate; iterative adjustments of the leveling mount align the tips with the substrate. An example is shown in Figure 5.3.2, where tip 1 first reaches contact with the surface first (Figure 5.3.2a). After an adjusting the leveling mount, as indicated, all five tips are approximately in contact at the same time (Figure 5.3.2b). Variations in tip heights and cantilever bending prevent perfect alignment between the tips and the surface, and so a working range is about 200-300 nm for all tips to be in contact simultaneously.

5.4 *Thermal Patterning with Arrays*

Having resolved issues with leveling, we return to parallelization of TCNL. Figure 5.4.1 and Figure 5.4.2 show two examples of patterns made in the same PPV-precursor (poly(p-xylene tetrahydrothiophenium chloride)) described in chapter four. For Figure 5.4.1, all five tips were brought into contact with the substrate simultaneously and patterned the same 3 by 3 array of pentagons at increasing temperatures. In agreement with the results shown and described in chapter four, the corresponding fluorescence measurements suggest the conversion from the pre-cursor film to the semi-conducting PPV polymer. As the temperature increases, so too does the photoluminescence of the PPV. Figure 5.4.1a, shows a Raman spectroscopy measurement of an array patterned area (fluorescence inset); the increased signal in the 1160-1180 cm^{-1} and 1580-1600 cm^{-1} wavenumber range are indicative of the chemical transformation [70].

Figure 5.4.2 shows a PPV-precursor substrate patterned with a set of lines at

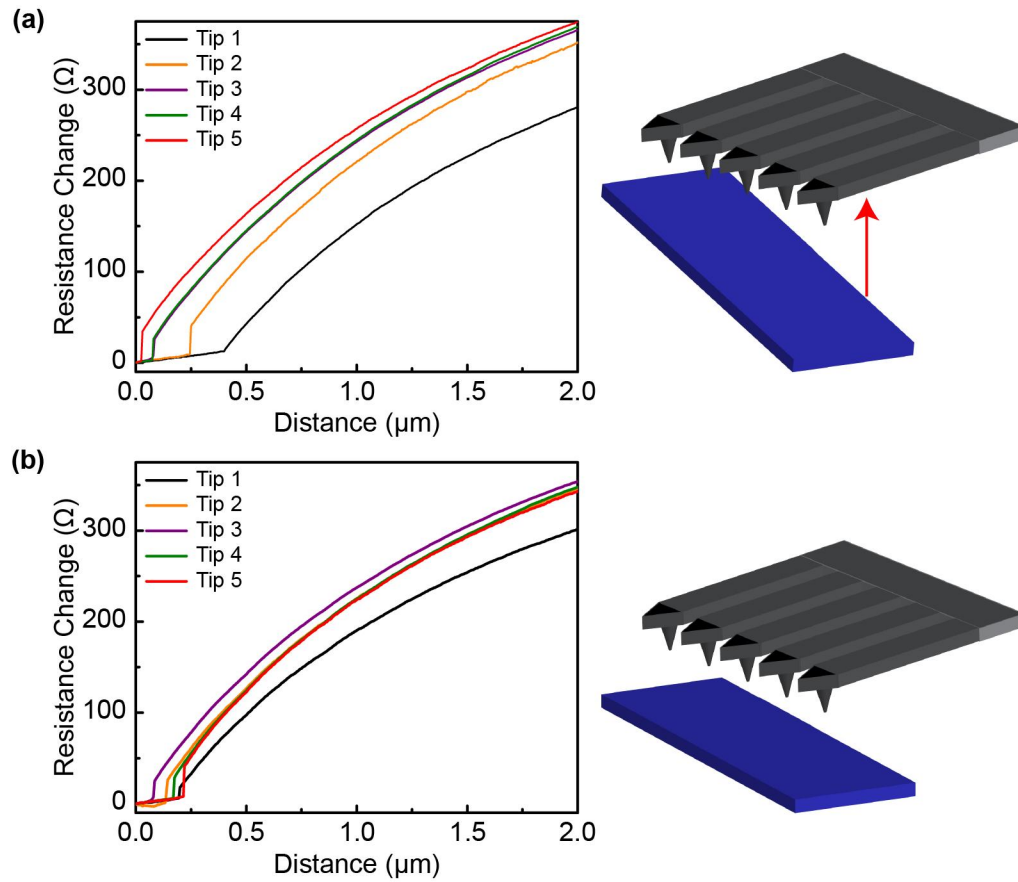


Figure 5.3.2: Resistance measurements of individual cantilevers in an array versus distance. (a) Measurement and schematic showing misalignment between the thermal cantilever array and the substrate. (b) Measurement and schematic showing all five tips in contact with the substrate near simultaneously after indicated correction made (a).

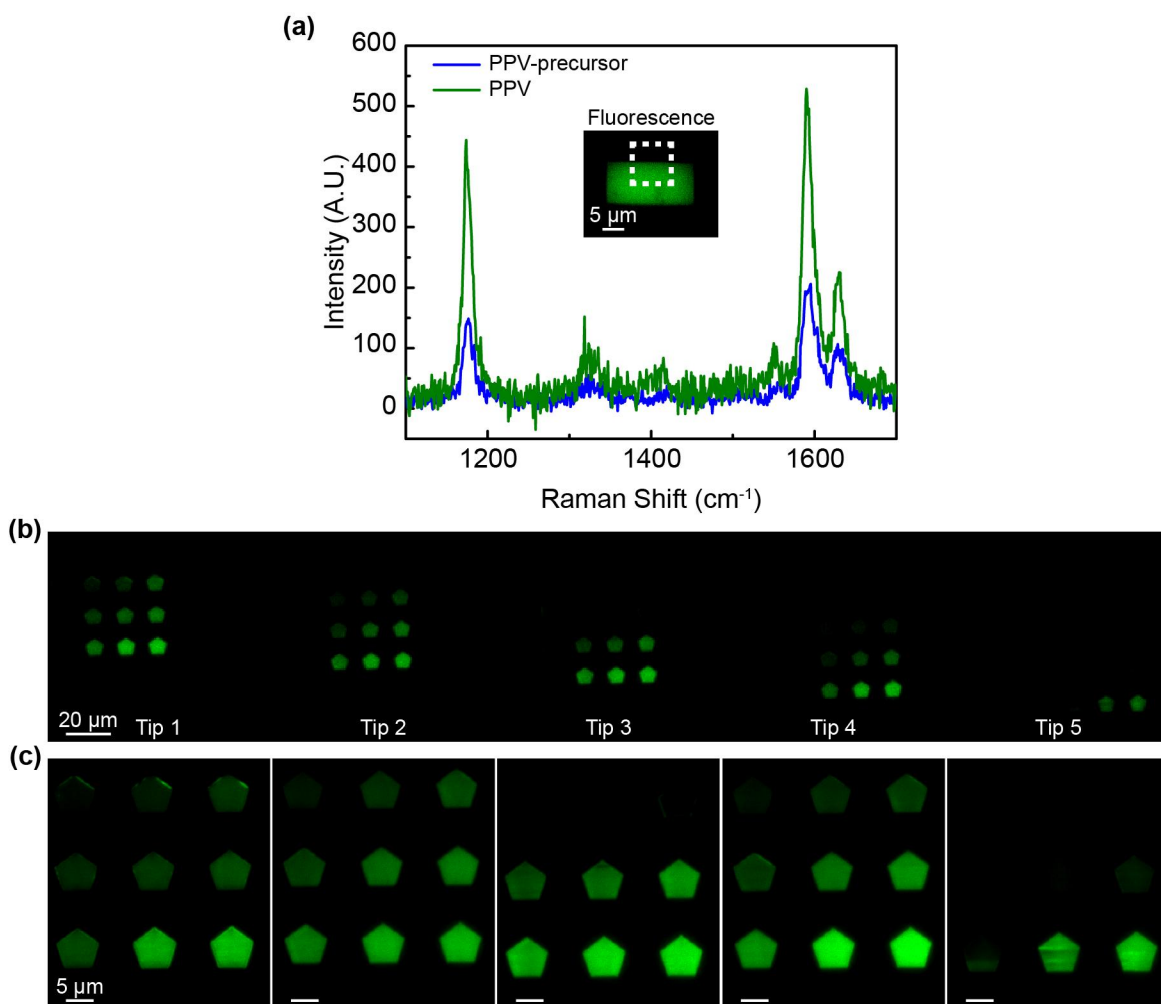


Figure 5.4.1: Thermal patterning in a PPV-precursor film made with thermal cantilever array. (a) Raman measurements indicating the transformation from precursor to PPV. (b) Fluorescence image of pentagon PPV patterns made with thermal array. (c) Zoom-in version of patterns from (b).

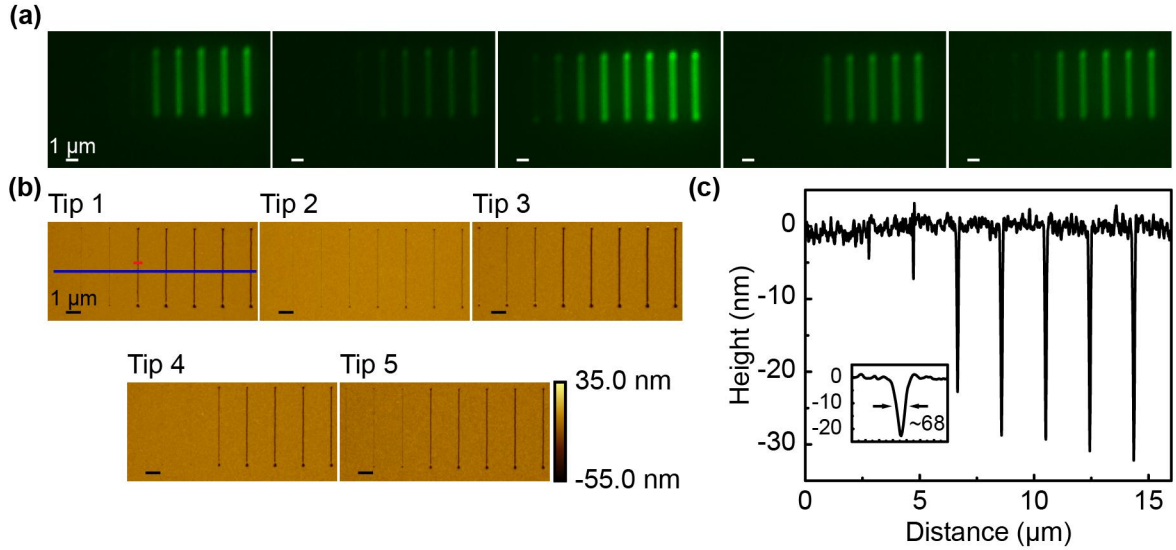


Figure 5.4.2: Measurements of lines made in PPV-precursor film made with thermal cantilever array (a) Fluorescence image of patterns of lines made with thermal cantilever array. (b) AFM image of patterns imaged in (a). (c) Topography profile for Tip 1 (indicated in blue in (a)), inset indicates a resolution of about 68 nm.

increasing temperatures with the thermal cantilever array. The fluorescence images indicate the presence of the photolumescent PPV polymer, and AFM measurements indicate a change in the height that was described and measured in chapter four. Finally, Figure 5.4.2c, shows a profile of the lines; the inset indicates a resolution of 68 nm; this measurement is on par with values measured in chapter four and described in the literature [70].

5.5 Thermal Imaging

Thermal cantilevers have the unique ability to both write and read the surface through the integrated heater. Metrology of surface variation is useful to verify thermal lithography and make alterations as needed [57]. While we have described and present the mechanisms for TCNL writing, central to thermal imaging is the energy transfer between tip and substrate. This transfer induces a measurable effect based on the substrate composition and topography. More specifically, the tip-substrate interaction manifests as a change in the thermal cantilevers electronic properties, namely

the cantilevers resistance. Small changes in the resistance register variations in the surface topography, and while the mapping is not perfect, thermal topography imaging provides a qualitative method to confirm lithographic patterning. To understand the mechanisms and principles of thermal imaging, we start with a single cantilever to display the most important features, and then expand the concept to arrays.

5.5.1 Thermal Imaging with a Single Tip

To demonstrate thermal imaging, a single cantilever is brought into contact with an AFM z-calibration grating. While in principle we could pattern a substrate and measure the change, the materials presented in this work are not conducive for this since they are thermally reactive; in place we use an AFM z-calibration grating. A z-calibration grating is a repetitive square corrugated substrate, which simplifies the analysis and interpretation of thermal imaging. By biasing the tip with a constant voltage and measuring the resistance as the tip rasters the surface, the change in resistance maps out changes in the topography. The results are shown in Figure 5.5.1, where the relative changes in the resistance are shown. Also shown in Figure 5.5.1 is a contact mode image of the same area. The changes in resistance correspond to the changes in topography. The troughs of the calibration grating have a lower resistance than the peaks; in the valleys, there is an increased heat transfer between the cantilever and the substrate. With an increased heat flux out of the cantilever, the temperature in the heater region lowers, and as explained in chapter three, a lower temperature corresponds to a lower resistance. The effect is reversed for the peaks, where there is less heat transfer and correspondingly a higher temperature and resistance. Interestingly, this thermal imaging mode, also measures the speck of dust seen in the topographic image. The resistance is highest on the dust since the tip is furthest away from the substrate. Using this technique, resistance, R , sensitivities ($\frac{\Delta R}{R}$) in vertical resolutions down to 10^{-6} - 10^{-5} /nm have been reported [54]; with a

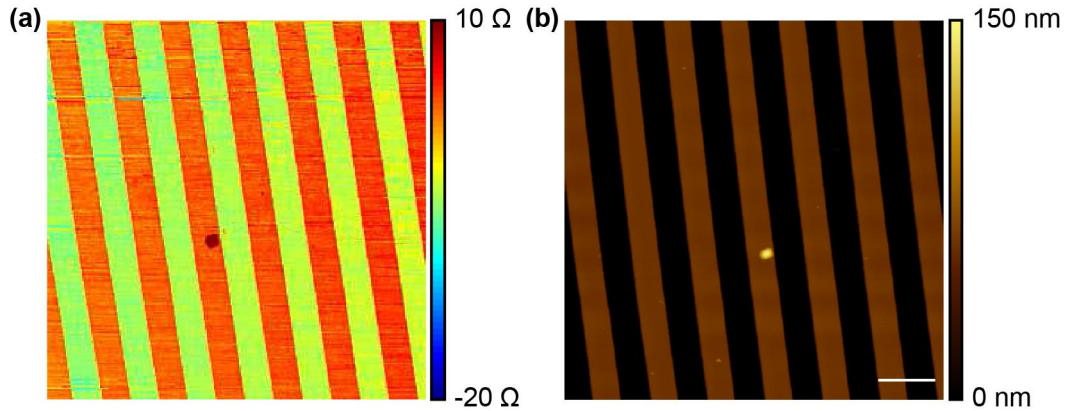


Figure 5.5.1: (a) Thermal imaging of a z-calibration grating with a single tip (b) AFM image of the same area measured in (a).

modified version, vertical resolutions less than 1 nm have been shown [150].

5.5.2 Thermal Imaging with Arrays

The same mechanisms to do thermal imaging with a single tip apply to the cantilever arrays. After aligning the tips with substrate, all five tips are simultaneously rastered across a z-calibration, and because each tip is individually addressable, the changes in resistance map out the local tip's topography. The results are shown in Figure 5.5.2. The sharp edges seen in the optical feedback AFM image and the thermal image for a single tip seen in Figure 5.5.1 are present in Figure 5.5.2. It should be noted that in Figure 5.5.2, although the images look contiguous and connected, this is purely coincidental. In fact there is about $110 \mu\text{m}$ between each cantilever as can be measured from Figure 5.4.1a. Techniques and methods for image stitching do exist [151], but since the intent is to demonstrate simultaneous imaging, this suffices. Metrology of surfaces is especially valuable for situations in which corrections to lithographic patterning may be needed [57].

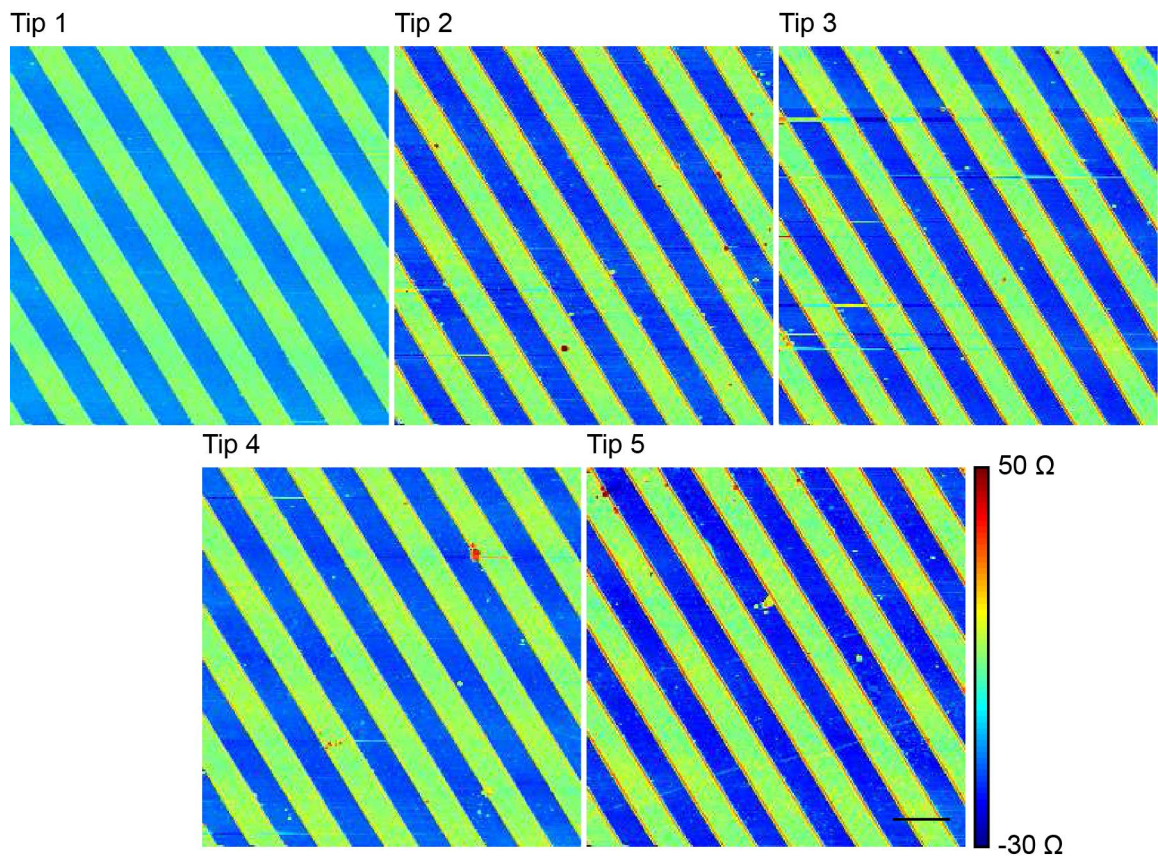


Figure 5.5.2: Thermal image obtained from a z-calibration grating with a thermal cantilever array.

5.6 Complications with Arrays

Despite the nice results discussed and displayed in this section, there are several unavoidable complications associated with the current thermal array setup. While leveling does a lot to maintain the tips being in contact with the surface concurrently, there are still situations in which one tip may lose contact with the surface. The mechanism used in this chapter to overcome this limitation was to increase the load to insure all tips maintained contact; however, this can have adverse effects such as a worsening of the resolution or faster tip wear. The inability to control the loading force also makes controlled chemical reactions difficult since increased loads increase the efficiency parameter [109]; this leads to a less effective control as to how heater temperature will transform a substrate. More work needs to be done to alleviate these issues, and possible solutions include coupling a second heater [152] with the Lorenz magnetic force [106].

The second issue is that there is some cross-talk between the cantilevers [146]. Experimental measurements have shown that the cross-talk is close to linear and the cross-talk seems to follow a superposition rule when multiple cantilevers are activated. In order to alleviate these issues, the thermal cantilevers could be run in a closed loop operation [150].

5.7 Final Word

This chapter set out to describe and show proof of principle parallelization of TCNL patterning. Using an array of thermal cantilevers, the ability to read and write to a surface were demonstrated. While little work was done to demonstrate the concepts in discussed in chapter two through four, complex patterning with individually addressable cantilevers indicates that similar principles could be adapted and modified for thermal arrays. Future works with arrays may include taking into account the complications discussed.

CHAPTER VI

CONCLUSIONS AND FUTURE WORKS

6.1 Introduction

The goal of this thesis was to develop TCNL to fabricate controlled chemical and topographic gradients that span from the nano-scale to the micro-scale. In order to do this, we started described and applied a chemical kinetics model to TCNL, and then we exploited the model to control chemical reactions down to the nano-scale. In this thesis, we developed a systematic approach to study and demonstrate how temperature and speed affect the localized, TCNL induced chemical reaction both on the surface and into the body of the substrate. In this chapter, we summarize chapters two through five, emphasize areas needing improvement, and discuss applications for chemical and topographic gradients.

6.2 Review

In chapter two, we identified and adapted a chemical kinetics model to explain the key physical principles of TCNL. Our modified model accounted for tip motion and we derived a probability equation to predict the evolution of a thermally induced chemical reaction. The model showed that the essential component to TCNL's high resolution was the coupling between the temperature profile and the solution of the chemical kinetics equation. While the temperature profile is difficult to compute, we assumed a decaying profile and approximated a decay length with previous empirical data.

In chapter three, we apply the results derived in chapter two to surface reaction. We combined a thermally activated polymer substrate with quantitative fluorescence

microscopy to measure TCNL induced surface concentration. We compared the fluorescence results against the model, and we showed excellent agreement to our predictions in chapter two. The dependencies on temperature and speed were exploited to create and design spatially extended patterns of varying chemical concentrations, and the designed patterns demonstrated high levels accuracy on short length scales (sub micron).

Chapter four moved away from studying surface only effects and expanded the model to account for 3-D effects. This is a meaningful contribution to TCNL since patterning of other material properties requires control beyond the surface. The chemical kinetics equations from chapter two were modified versions to account for 3-D effects, and using a film of a semi-conducting precursor, z-dependence was semi-quantified using two physically different but measureable effects manifesting from the TCNL process. The long term impact of this work was the ability to expand the developed analysis to other material properties and this would be useful for situations where the techniques impart patterns not easily translated to fluorescence microscopy.

Finally, in chapter five, we showed proof of principle parallelization of TCNL. The work in that chapter indicated that despite some of the complications associated with working with arrays (such as leveling or parallel reading), parallelization of TCNL works without much loss in the high resolutions. Though there is work to be done, parallelization is a powerful tool to make TCNL an attractive candidate for large scale applications.

6.3 Future Works and Improvements

The results shown throughout this work showed good agreement and an impressive amount of control over such short length scales. Future works on chemical kinetics modeling should look to expand alleviate some of the assumptions and exploit some of the extra factors that were ignored. There would be much to gain from finding or

computing a better approximation to the temperature profile. The y/z dependence or the exact speed dependence, for example, could be derived. Verification of the computed temperature profile could be done by comparing against empirical investigations of individual points [97] or against line resolutions. These studies should also include comparing different conditions such as film thickness or the thermal conductivity of the underlying substrate, and these studies could be applied to be surface and 3-D effects.

Future works on surface reactions include taking into account polymer motion. In chapter three, we ignored polymer melting because of the increased glass transition temperature since the polymer was crosslinked. There has been some work done in connection with thermomechanical lithography regarding glass transition of polymer films [52, 97]. Coupling these results and studies with chemical kinetics works could effectively be used to predict an average polymer motion. This type of study, however, would be difficult since the exact relationship between the surface and 3-D effects would be needed.

For chapter three (and four) we ignore the dependence in the y -direction because our patterning technique wrote consecutive lines smaller than the measured FWHM from FFM. By accounting for the y -direction, future works could improve upon designing profiles of chemical concentration. In those chapters, we also worked at speeds lower than 10 mm/s to assume an instantaneous temperature profile for the given the time scales [92], but future works could try to exploit time dependence to improve spatial resolutions.

Other factors that were not varied in this work are film thickness [153], surrounding medium [103, 154], substrate conductivity [95], and load dependent phenomena [109]. Film thickness studies should be studied in relation with 3-D effects and the temperature profile. Using vacuum chambers or changing the medium from air to another form such as liquids or a more conductive gas may change the resolutions or

even some of the dynamics since medium effects enhance or dampen reactions such as in catalytic processes [155]. Throughout this work, load effects were ignored, but there is some evidence that increasing the load alters the dynamics at the tip-surface interface. The efficiency parameter, for example, has been shown to increase with increased load [109]. Nano-shaving and nano-grafting techniques have also shown that shearing forces can selectively cleave bonds [156, 157], and it is conceivable that by varying load, the effect may manifest in a way analogous to a catalyst, which raises or lowers a reactions activation energy.

6.3.1 Experiments to Verify Assumptions

Throughout this work, a series of assumptions were made to adapt the chemical kinetics model for TCNL. In this section, we briefly review how some of the key assumptions could experimentally be validated. Specifically, the focus is on the time dependence, polymer motion (glass transition temperature), and y-direction dependence.

To test the time dependence, an experiment must be designed to determine the lower bound time scales for which the static assumption starts to fall apart. The lower bound suggested in this work and other works is about 100 ns; this time scale is on the order of the time required for the air molecules between the cantilever and the substrate to equilibrate. For this experiment, it is important to keep in mind that the heating time scale of the cantilever is about 1 μ s. To remove added complications from this time scale, one solution is to keep the cantilever heated and temporarily bring the tip into contact with the substrate. Two possible ways to introduce this type experiment would be introducing an oscillating tip (in a similar manner to that in tapping mode) or using a system with a capacitive loading instrument [56].

To test how ignoring polymer motion alters the outcome, two experiments need to be employed. The first experiment removes the increased glass transition temperature by reducing or completely removing the cross-linking between the polymer. This type

of experiment could potentially show that there is a minimum concentration of cross-linking below which the glass transition cannot be ignored. The second experiment would remove any concerns of the glass transition by introducing a non polymer based substrate. Some possible substrates include self assembled monolayers (SAMs) [42].

Finally, to test the validity of ignoring the y -dependence, the spacing between the zig-zags shown in Figure 2.3.2 should be varied. Once the spacing exceeds the FWHM, it should become necessary to account for the y -dependence. This type of experiment needs to take into consideration limitations of the metrology. For example, fluorescence signals will be diffraction limited, and this may lead to a blurring or averaging of the signal. This averaging could cause the breakdown to happen at a length scale different from the predictions.

6.4 Applications of Chemical Gradients

The ability to create controlled chemical concentration profiles down to the mesoscopic scales offers a number of new applications [15]. Several applications are discussed in this section, and while some of these studies have been done on the micro-scale or larger, the ability to controllably shrink these phenomena down may offer new results.

6.4.1 Surface Energy Gradients

There have been several studies dedicated to examining how gradients in surface concentrations have induced droplet motion. For example, water has been observed to run "uphill" because of gradient profiles in the hydrophobicity/hydrophilicity of the surface [12]. Inclines up to about 15 have been demonstrated. Some of these works have been done with geometric arrangements in material properties [11], but there has been some work done with chemical concentration gradients [15]. By introducing profiles with linear gradients, motion of water droplets could be controlled [158]. The length scales usually associated with these types of studies are on the order of

centimeters or larger.

TCNL is a well suited candidate to fulfill this niche, since it can reach small length scales and has been demonstrated to achieve controllable profiles. Additionally, with the demonstrated 2-D control, TCNL could introduce chemical gradients that alter droplet motion, and interesting studies could include how colloidal droplets combine.

6.4.2 Biophysical Applications

Chemical gradients have been shown to induce cellular activity and directional growth. For example, surface chemical gradients of fibronectin increase cellular migration, and increasing the magnitude of the gradient increased migration speed [159]. The one drawback to these studies, however, is the inability to extend towards sharp enough gradients to see if cellular migration was bound [160]. Due to the achievable length scales, TCNL could pattern substrates with sharp enough gradients to observe these effects.

Neuronal axon growth shows preference to gradients in the protein laminin [10, 31]. Gradients of laminin are obvious candidates for creating neural networks to study inter-neural responses. TCNL is an interesting candidate for this type of study, since gradients at different length scales and with different magnitudes could be made to see how the axons are affected. Some preliminary work is currently underway in collaboration with several labs.

Polymers exhibit different properties dependent on their grafting densities [161]. Chemical gradients have been used to study the transition from the mushroom regime to polymer brush regime [15, 161]; the transition is estimated to take place around the radius of gyration of the polymer [162]. Due to the small scale TCNL is capable of, it is possible to experimentally measure and vary the length scales down to which this transition occurs; a study of this form could also take into account the effects from solvents.

6.5 *Applications of Topographic Gradients*

Topographic gradients are valuable for a number of different interesting applications and studies. Most of the applications suggested here involve water or another solvents, and for these particular applications, the precursor film is not optimal since it is soluble in water and some organic solvents, such as methanol. To alleviate this issue, we first discuss and demonstrated a technique similar to one used in microcontact printing [20].

6.5.1 **Transfer PPV Patterns to PDMS**

While the work done in chapter four showed the ability to create topographic gradients, the precursor film is not very conducive for some applications since it is easily dissolved in water and some organic solvents (particularly methanol). Moreover, the films were observed to have a short shelf life, presumably because the polymer film undergoes the chemical transformation slowly at room temperature.

To prolong the lifetime of the topographic gradients, a process used in microcontact and nano-contact printing was developed. The steps are shown in Figure 6.5.1. First a substrate is patterned with a desired topographic gradient. Next an uncured elastomeric material (polydimethylsiloxane, PDMS, as labeled in the figure) filled in the mold formed in the precursor film. The sample was placed in a vacuum chamber to remove all air bubbles and then placed in an oven ($\approx 60^\circ\text{C}$) for about an hour (steps not shown). The temperature was kept low to prevent the transformation of the PPV-precursor to PPV. Finally the cured elastomeric material was removed from the sample, leaving an impression of the substrates topographic patterns. It should be noted that the process, just as in microcontact printing, inverts the patterns in the mold.

Figure 6.5.2 shows some preliminary evidence of this process. The initial PPV film is shown in Figure 6.5.2a patterned with an array of squares. After the transfer process

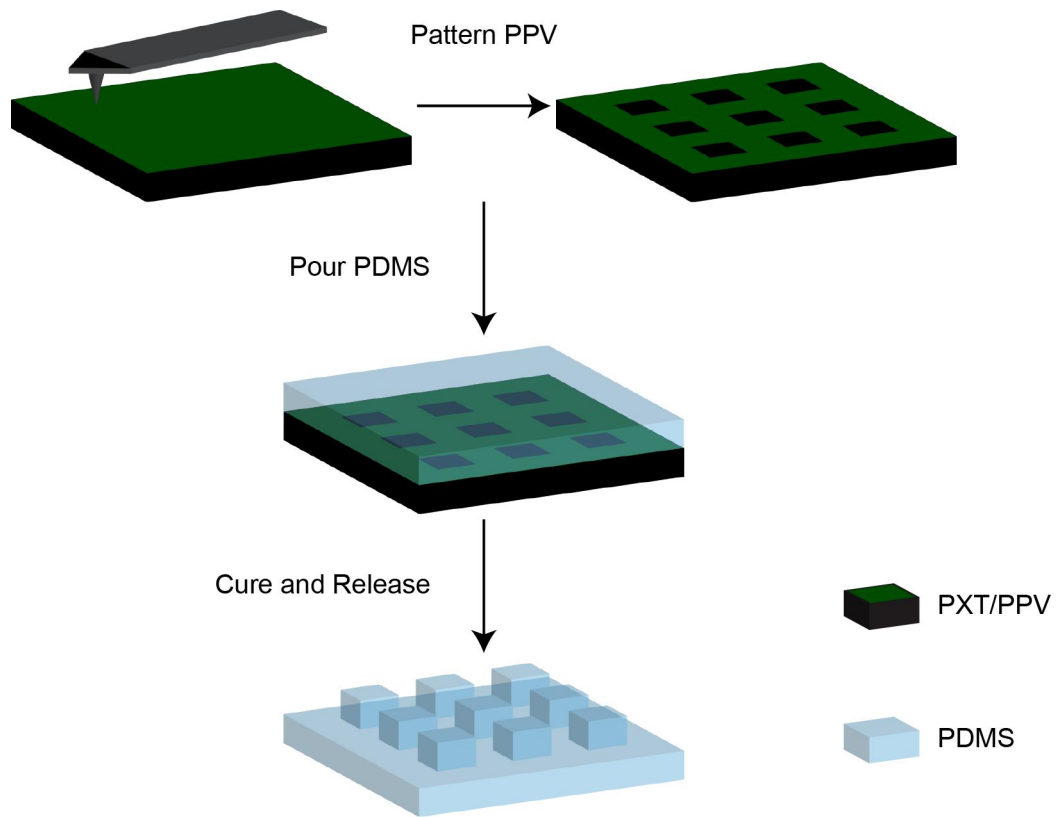


Figure 6.5.1: Schematic showing transfer of PPV topographic pattern to PDMS.

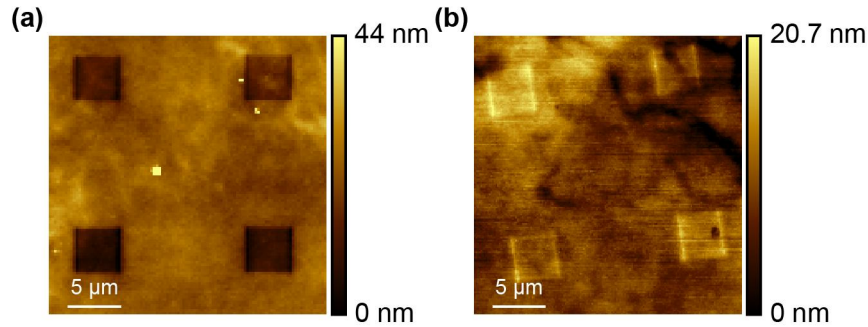


Figure 6.5.2: Experimental evidence showing the transfer of (a) PXT/PPV topographic patterns to (b) PDMS.

is completed, the elastomeric material was imaged with an AFM. The imprinted patterns are shown in Figure 6.5.2b, and as expected, the square pattern is now inverted. This is a proof of principle demonstration, but it shows promise since some interesting features, such as the edges are present. While this technique requires some optimization, this demonstrates the ability to replicate topographic patterns for other applications.

6.5.2 Colloidal Patterning

The ability to strategically place colloids holds promise for a number of fields such as photonic crystals [163, 164]. There are several studies that use topographic variations to site specifically place colloids [165]. In these studies, researchers take a substrate patterned with grooves and pits and incubate the substrate with a colloidal solution [166]. The colloids stick everywhere, but by spinning the surface, colloids not trapped in the grooves or pits fly off. The trapped colloids remain in the forms of the pits and grooves. Interestingly, at different speeds and heights, colloids of different sizes can be trapped. Other interesting applications come from using directed interactions between colloids [167, 168].

6.5.3 Nano-Fluidics

Nano-fluidic devices hold a promise for a variety of fields. Studies on the electrokinetic effects are fascinating since the small scales associated with the nano-channels are approaching the Debye length for the electric double layer [169]. Because of this, nano-fluidic devices have different conductivities than microfluidic devices at similar ionic concentrations [170]. One of the issues, however, with nano-channels is the ability to *affordably* [170] produce 1-D and 2-D nano-channels, but with the ability to replicate topographic patterns, TCNL is formidable candidate for these types of studies and applications.

6.6 *Final Word*

We highlight various improvements and applications for TCNL fabricated gradients. While there remains much to do to optimize the technique, the ability to control various material properties down to nano-scale lengths holds promise for a number of interesting areas.

We set out to develop a systematic approach to control TCNL to alter material transformations down to nano-scale. While the work was demonstrated on two different organic polymer materials, the techniques and systematic approach developed caters to the plethora of materials which are suitable candidates for TCNL. By knowing how material properties vary with a chemical transformation, a chemical kinetics model can be applied to predict and control the substrate reaction, and because of this versatility and compatibility with other materials, TCNL is a unique and powerful lithographic technique.

APPENDIX A

DERIVATION OF EQUATION 4.13

The starting point is the substitution of equation 4.12 into equation 4.10:

$$Pr(z) = 1 - e^{-\frac{k_o \cdot e^{-\frac{z}{\kappa}}}{v}} \quad (\text{A.1})$$

Substituting equation A.1 into the modified body equation 4.3 reveals:

$$Pr_{body} = \frac{N}{N_{tot}} = \frac{\int Pr dz}{\int dz} = \frac{\int Pr(z) dz}{L} = \frac{\int_0^L 1 - e^{-\frac{k_o \cdot e^{-\frac{z}{\kappa}}}{v}} dz}{L} \quad (\text{A.2})$$

where the integral is over the film thickness. Writing out the Taylor expansion for an exponential series:

$$e^x = \sum_{n=0}^{\infty} \frac{x^n}{n!} \quad (\text{A.3})$$

We use this form for equation A.2:

$$Pr_{body} = 1 - \frac{\int_0^L \sum_{n=0}^{\infty} \frac{(-\frac{k_o \cdot e^{-\frac{z}{\kappa}}}{v})^n}{n!} dz}{L} = 1 - \sum_{n=0}^{\infty} \frac{\int_0^L \frac{(-\frac{k_o \cdot e^{-\frac{z}{\kappa}}}{v})^n}{n!} dz}{n!} \quad (\text{A.4})$$

Equation A.4 can be integrated to:

$$Pr_{body} = \frac{\kappa}{L} \left(\sum_{n=1}^{\infty} \frac{(-\frac{k_o \cdot e^{-\frac{z}{\kappa}}}{v})^n}{n \cdot n!} - \sum_{n=1}^{\infty} \frac{(-\frac{k_o}{v})^n}{n \cdot n!} \right) \quad (\text{A.5})$$

The definition of the exponential integral is given as [171]:

$$\text{Ei} = \int_x^{\infty} \frac{e^{-x}}{x} dx = \gamma - \ln|x| - \sum_{n=1}^{\infty} \frac{(-x)^n}{n \cdot n!} \quad (\text{A.6})$$

where gamma is the Euler-Mascheroni constant. Using this form, we can reduce equation A.5 to:

$$Pr = \left(\text{Ei}\left(\frac{k_o}{v} e^{-\frac{L}{\kappa}}\right) + \ln\left(\frac{k_o}{v} e^{-\frac{L}{\kappa}}\right) - \text{Ei}\left(\frac{k_o}{v}\right) - \ln\left(\frac{k_o}{v}\right) \right) \cdot \frac{\kappa}{L} \quad (\text{A.7})$$

Equation A.7 is the same as equation 4.13.

REFERENCES

- [1] Gil, D., Brunner, T. A., Fonseca, C., Seong, N., Streefkerk, B., Wagner, C., and Stavenga, M. Immersion Lithography: New Opportunities for Semiconductor Manufacturing. volume 22, pages 3431–3438. AVS.
- [2] Mendes, P., Yeung, C., and Preece, J. Bio-nanopatterning of Surfaces. *Nanoscale Research Letters*, 2(8):373–384, 2007.
- [3] Frstner, R., Barthlott, W., Neinhuis, C., and Walzel, P. Wetting and Self-Cleaning Properties of Artificial Superhydrophobic Surfaces. *Langmuir*, 21(3):956–961, 2005.
- [4] Allara, D. L. A Perspective on Surfaces and Interfaces. *Nature*, 437(7059):638–639, 2005.
- [5] Hullmann, A. and Meyer, M. Publications and Patents in Nanotechnology. *Scientometrics*, 58(3):507–527, 2003.
- [6] Son, Y. W., Cohen, M. L., and Louie, S. G. Energy Gaps in Graphene Nanoribbons. *Physical Review Letters*, 97(21):216803, 2006.
- [7] Falconnet, D., Pasqui, D., Park, S., Eckert, R., Schiff, H., Gobrecht, J., Barbucci, R., and Textor, M. A Novel Approach to Produce Protein Nanopatterns by Combining Nanoimprint Lithography and Molecular Self-Assembly. *Nano Letters*, 4(10):1909–1914, 2004.
- [8] Xia, Y. and Whitesides, G. M. Soft Lithography. *Annual review of materials science*, 28(1):153–184, 1998.
- [9] Belisle, J. M., Correia, J. P., Wiseman, P. W., Kennedy, T. E., and Costantino, S. Patterning Protein Concentration using Laser-Assisted Adsorption by Photobleaching, LAPAP. *Lab on a Chip*, 8(12):2164–2167, 2008.
- [10] Dertinger, S. K. W., Jiang, X., Li, Z., Murthy, V. N., and Whitesides, G. M. Gradients of Substrate-Bound Laminin Orient Axonal Specification of Neurons. *Proceedings of the National Academy of Sciences*, 99(20):12542–12547, 2002.
- [11] Zhang, J. and Han, Y. Shape-Gradient Composite Surfaces: Water Droplets Move Uphill. *Langmuir*, 23(11):6136–6141, 2007.
- [12] Chaudhury, M. K. and Whitesides, G. M. How To Make Water Run Uphill. *Science*, 256(5063):1539–1541, 1992.
- [13] Lafuma, A. and Quéré, D. Superhydrophobic States. *Nat Mater*, 2(7):457–460, 2003.

- [14] Chu, R. C., Simons, R. E., Ellsworth, M. J., Schmidt, R. R., and Cozzolino, V. Review of Cooling Technologies for Computer Products. *Device and Materials Reliability, IEEE Transactions on*, 4(4):568–585, 2004.
- [15] Morgenthaler, S., Zink, C., and Spencer, N. D. Surface-Chemical and -Morphological Gradients. *Soft Matter*, 4(3):419–434, 2008.
- [16] Zhou, X., Boey, F., Huo, F., Huang, L., and Zhang, H. Chemically Functionalized Surface Patterning. *Small*, 7(16):2273–2289, 2011.
- [17] Bernard, A., Renault, J. P., Michel, B., Bosshard, H. R., and Delamarche, E. Microcontact Printing of Proteins. *Advanced Materials*, 12(14):1067–1070, 2000.
- [18] Rozkiewicz, D. I., Gierlich, J., Burley, G. A., Gutmiedl, K., Carell, T., Ravoo, B. J., and Reinhoudt, D. N. Transfer Printing of DNA by “Click” Chemistry. *ChemBioChem*, 8(16):1997–2002, 2007.
- [19] Mrksich, M. and Whitesides, G. M. Patterning Self-assembled Monolayers Using Microcontact Printing: A New Technology for Biosensors? *Trends in Biotechnology*, 13(6):228–235, 1995.
- [20] Mrksich, M., Dike, L. E., Tien, J., Ingber, D. E., and Whitesides, G. M. Using Microcontact Printing to Pattern the Attachment of Mammalian Cells to Self-Assembled Monolayers of Alkanethiolates on Transparent Films of Gold and Silver. *Experimental Cell Research*, 235(2):305–313, 1997.
- [21] Lange, S. A., Benes, V., Kern, D. P., Hrber, J. K. H., and Bernard, A. Microcontact Printing of DNA Molecules. *Analytical Chemistry*, 76(6):1641–1647, 2004.
- [22] Hui, C. Y., Jagota, A., Lin, Y. Y., and Kramer, E. J. Constraints on Microcontact Printing Imposed by Stamp Deformation. *Langmuir*, 18(4):1394–1407, 2002.
- [23] Li, H. W., Muir, B. V. O., Fichet, G., and Huck, W. T. S. Nanocontact Printing: A Route to sub-50-nm-Scale Chemical and Biological Patterning. *Langmuir*, 19(6):1963–1965, 2003.
- [24] Kraus, T., Stutz, R., Balmer, T. E., Schmid, H., Malaquin, L., Spencer, N. D., and Wolf, H. Printing Chemical Gradients. *Langmuir*, 21(17):7796–7804, 2005.
- [25] Shaw, J. M., Gelorme, J. D., LaBianca, N. C., Conley, W. E., and Holmes, S. J. Negative Photoresists for Optical Lithography. *IBM Journal of Research and Development*, 41(1.2):81–94, 1997.
- [26] Wu, B. and Kumar, A. Extreme Ultraviolet Lithography: A Review. *Journal of Vacuum Science and Technology B: Microelectronics and Nanometer Structures*, 25(6):1743–1761, 2007.

- [27] Switkes, M. and Rothschild, M. Immersion lithography at 157 nm. volume 19, pages 2353–2356. AVS.
- [28] Scrimgeour, J., Kodali, V. K., Kovari, D. T., and Curtis, J. E. Photobleaching-Activated Micropatterning on Self-Assembled Monolayers. *Journal of Physics: Condensed Matter*, 22(19):194103, 2010.
- [29] Holden, M. A. and Cremer, P. S. Light Activated Patterning of Dye-Labeled Molecules on Surfaces. *Journal of the American Chemical Society*, 125(27):8074–8075, 2003.
- [30] Waldbaur, A., Waterkotte, B., Schmitz, K., and Rapp, B. E. Maskless Projection Lithography for the Fast and Flexible Generation of Grayscale Protein Patterns. *Small*, 8(10):1570–1578, 2012.
- [31] Dertinger, S. K. W., Chiu, D. T., Jeon, N. L., and Whitesides, G. M. Generation of Gradients Having Complex Shapes Using Microfluidic Networks. *Analytical Chemistry*, 73(6):1240–1246, 2001.
- [32] Mendes, P. M., Jacke, S., Critchley, K., Plaza, J., Chen, Y., Nikitin, K., Palmer, R. E., Preece, J. A., Evans, S. D., and Fitzmaurice, D. Gold Nanoparticle Patterning of Silicon Wafers Using Chemical E-Beam Lithography. *Langmuir*, 20(9):3766–3768, 2004.
- [33] Zhang, G. J., Tanii, T., Zako, T., Hosaka, T., Miyake, T., Kanari, Y., Funatsu, T., and Ohdomari, I. Nanoscale Patterning of Protein Using Electron Beam Lithography of Organosilane Self-Assembled Monolayers. *Small*, 1(8-9):833–837, 2005.
- [34] Broers, A. N., Hoole, A. C. F., and Ryan, J. M. Electron Beam Lithography-Resolution Limits. *Microelectronic Engineering*, 32(14):131–142, 1996.
- [35] Christman, K. L., Enriquez-Rios, V. D., and Maynard, H. D. Nanopatterning Proteins and Peptides. *Soft Matter*, 2(11):928–939, 2006.
- [36] Vieu, C., Carcenac, F., Ppin, A., Chen, Y., Mejias, M., Lebib, A., Manin-Ferlazzo, L., Couraud, L., and Launois, H. Electron Beam Lithography: Resolution Limits and Applications. *Applied Surface Science*, 164(14):111–117, 2000.
- [37] Fujita, J., Ohnishi, Y., Ochiai, Y., and Matsui, S. Ultrahigh Resolution of Calixarene Negative Resist in Electron Beam Lithography. *Applied Physics Letters*, 68(9):1297–1299, 1996.
- [38] Grigorescu, A. E. and Hagen, C. W. Resists for sub-20-nm Electron Beam Lithography with a Focus on HSQ: State of the Art. *Nanotechnology*, 20(29):292001, 2009.

- [39] Shi, J., Chen, J., and Cremer, P. S. Sub-100 nm Patterning of Supported Bilayers by Nanoshaving Lithography. *Journal of the American Chemical Society*, 130(9):2718–2719, 2008.
- [40] Liu, M., Amro, N. A., Chow, C. S., and Liu, G.-y. Production of Nanostructures of DNA on Surfaces. *Nano Letters*, 2(8):863–867, 2002.
- [41] Tinazli, A., Piehler, J., Beuttler, M., Guckenberger, R., and Tampé, R. Native Protein Nanolithography that can Write, Read and Erase. *Nature Nanotechnology*, 2(4):220–225, 2007.
- [42] Fresco, Z. M., Suez, I., Backer, S. A., and Fréchet, J. M. J. AFM-Induced Amine Deprotection: Triggering Localized Bond Cleavage by Application of Tip/Substrate Voltage Bias for the Surface Self-Assembly of Nanosized Dendritic Objects. *Journal of the American Chemical Society*, 126(27):8374–8375, 2004.
- [43] Maoz, R., Cohen, S. R., and Sagiv, J. Nanoelectrochemical Patterning of Monolayer Surfaces: Toward Spatially Defined Self-Assembly of Nanostructures. *Advanced Materials*, 11(1):55–61, 1999.
- [44] Fuierer, R. R., Carroll, R. L., Feldheim, D. L., and Gorman, C. B. Patterning Mesoscale Gradient Structures with Self-Assembled Monolayers and Scanning Tunneling Microscopy Based Replacement Lithography. *Advanced Materials*, 14(2):154–157, 2002.
- [45] Piner, R. D., Zhu, J., Xu, F., Hong, S., and Mirkin, C. A. “Dip-Pen” Nanolithography. *Science*, 283(5402):661–663, 1999.
- [46] Lee, K. B., Park, S.-J., Mirkin, C. A., Smith, J. C., and Mrksich, M. Protein Nanoarrays Generated By Dip-Pen Nanolithography. *Science*, 295(5560):1702–1705, 2002.
- [47] Ginger, D. S., Zhang, H., and Mirkin, C. A. The Evolution of Dip-Pen Nanolithography. *Angewandte Chemie International Edition*, 43(1):30–45, 2004.
- [48] Mirkin, C. A. The Power of the Pen: Development of Massively Parallel Dip-Pen Nanolithography. *ACS Nano*, 1(2):79–83, 2007.
- [49] Hong, S., Zhu, J., and Mirkin, C. A. Multiple Ink Nanolithography: Toward a Multiple-Pen Nano-Plotter. *Science*, 286(5439):523–525, 1999.
- [50] Salaita, K., Wang, Y., Fragala, J., Vega, R. A., Liu, C., and Mirkin, C. A. Massively Parallel DipPen Nanolithography with 55000-Pen Two-Dimensional Arrays. *Angewandte Chemie*, 118(43):7378–7381, 2006.
- [51] Nelson, B. A. and King, W. P. Temperature Calibration of Heated Silicon Atomic Force Microscope Cantilevers. *Sensors and Actuators A: Physical*, 140(1):51–59, 2007.

- [52] Vettiger, P., Cross, G., Despont, M., Drechsler, U., Durig, U., Gotsmann, B., Haberle, W., Lantz, M. A., Rothuizen, H. E., Stutz, R., and Binnig, G. K. The “Millipede” - Nanotechnology Entering Data Storage. *Nanotechnology, IEEE Transactions on*, 1(1):39–55, 2002.
- [53] Vettiger, P., Despont, M., Drechsler, U., Durig, U., Haberle, W., Lutwyche, M. I., Rothuizen, H. E., Stutz, R., Widmer, R., and Binnig, G. K. The “Millipede”-More than Thousand Tips for Future AFM Storage. *IBM Journal of Research and Development*, 44(3):323–340, 2000.
- [54] Binnig, G., Despont, M., Drechsler, U., Haberle, W., Lutwyche, M., Vettiger, P., Mamin, H. J., Chui, B. W., and Kenny, T. W. Ultrahigh-Density Atomic Force Microscopy Data Storage with Erase Capability. *Applied Physics Letters*, 74(9):1329–1331, 1999.
- [55] Pires, D., Hedrick, J. L., De Silva, A., Frommer, J., Gotsmann, B., Wolf, H., Despont, M., Duerig, U., and Knoll, A. W. Nanoscale Three-Dimensional Patterning of Molecular Resists by Scanning Probes. *Science*, 328(5979):732–735, 2010.
- [56] Knoll, A. W., Pires, D., Coulembier, O., Dubois, P., Hedrick, J. L., Frommer, J., and Duerig, U. Probe-Based 3-D Nanolithography Using Self-Amplified Depolymerization Polymers. *Advanced Materials*, 22(31):3361–3365, 2010.
- [57] Hua, Y., Saxena, S., Henderson, C. L., and King, W. P. Nanoscale Thermal Lithography by Local Polymer Decomposition Using a Heated Atomic Force Microscope Cantilever Tip. *Journal of Micro/Nanolithography, MEMS, and MOEMS*, 6(2):023012–023012, 2007.
- [58] Carroll, K. M., Giordano, A. J., Wang, D., Kodali, V. K., Scrimgeour, J., King, W. P., Marder, S. R., Riedo, E., and Curtis, J. E. Fabricating Nanoscale Chemical Gradients with ThermoChemical NanoLithography. *Langmuir*, 29(27):8675–8682, 2013.
- [59] Fenwick, O., Bozec, L., Credgington, D., Hammiche, A., Lazzerini, G. M., Silberberg, Y. R., and Cacialli, F. Thermochemical Nanopatterning of Organic Semiconductors. *Nat Nano*, 4(10):664–668, 2009.
- [60] Fletcher, P. C., Felts, J. R., Dai, Z., Jacobs, T. D., Zeng, H., Lee, W., Sheehan, P. E., Carlisle, J. A., Carpick, R. W., and King, W. P. Wear-Resistant Diamond Nanoprobe Tips with Integrated Silicon Heater for Tip-Based Nanomanufacturing. *ACS Nano*, 4(6):3338–3344, 2010.
- [61] Nelson, B. A., King, W. P., Laracuenta, A. R., Sheehan, P. E., and Whitman, L. J. Direct Deposition of Continuous Metal Nanostructures by Thermal Dip-Pen Nanolithography. *Applied Physics Letters*, 88(3):033104–3, 2006.

- [62] Sheehan, P. E., Whitman, L. J., King, W. P., and Nelson, B. A. Nanoscale Deposition of Solid Inks via Thermal Dip Pen Nanolithography. *Applied Physics Letters*, 85(9):1589–1591, 2004.
- [63] Lee, W. K., Dai, Z., King, W. P., and Sheehan, P. E. Maskless Nanoscale Writing of Nanoparticle Polymer Composites and Nanoparticle Assemblies Using Thermal Nanoprobes. *Nano Letters*, 10(1):129–133, 2009.
- [64] Wang, D., Kodali, V. K., Underwood, William D., I., Jarvholm, J. E., Okada, T., Jones, S. C., Rumi, M., Dai, Z., King, W. P., Marder, S. R., Curtis, J. E., and Riedo, E. Thermochemical Nanolithography of Multifunctional Nanotemplates for Assembling Nano-Objects. *Advanced Functional Materials*, 19(23):3696–3702, 2009.
- [65] Wei, Z., Wang, D., Kim, S., Kim, S.-Y., Hu, Y., Yakes, M. K., Laracuente, A. R., Dai, Z., Marder, S. R., Berger, C., King, W. P., de Heer, W. A., Sheehan, P. E., and Riedo, E. Nanoscale Tunable Reduction of Graphene Oxide for Graphene Electronics. *Science*, 328(5984):1373–1376, 2010.
- [66] Lee, W.-K., Haydell, M., Robinson, J. T., Laracuente, A. R., Cimpoiasu, E., King, W. P., and Sheehan, P. E. Nanoscale Reduction of Graphene Fluoride via Thermochemical Nanolithography. *ACS Nano*, 7(7):6219–6224, 2013.
- [67] Kim, S., Bastani, Y., Lu, H., King, W. P., Marder, S., Sandhage, K. H., Gruverman, A., Riedo, E., and Bassiri-Gharb, N. Direct Fabrication of Arbitrary-Shaped Ferroelectric Nanostructures on Plastic, Glass, and Silicon Substrates. *Advanced Materials*, 23(33):3786–3790, 2011.
- [68] Szoszkiewicz, R., Okada, T., Jones, S. C., Li, T.-D., King, W. P., Marder, S. R., and Riedo, E. High-Speed, sub-15 nm Feature Size Thermochemical Nanolithography. *Nano Letters*, 7(4):1064–1069, 2007.
- [69] Wang, D. B., Szoszkiewicz, R., Lucas, M., Riedo, E., Okada, T., Jones, S. C., Marder, S. R., Lee, J., and King, W. P. Local Wettability Modification by Thermochemical Nanolithography with Write-Read-Overwrite Capability. *Applied Physics Letters*, 91(24):243104–3, 2007.
- [70] Wang, D., Kim, S., Underwood II, W. D., Giordano, A. J., Henderson, C. L., Dai, Z., King, W. P., Marder, S. R., and Riedo, E. Direct Writing and Characterization of poly(p-phenylene vinylene) Nanostructures. *Applied Physics Letters*, 95(23):233108–3, 2009.
- [71] Gotsmann, B., Duerig, U., Frommer, J., and Hawker, C. J. Exploiting Chemical Switching in a DielsAlder Polymer for Nanoscale Probe Lithography and Data Storage. *Advanced Functional Materials*, 16(11):1499–1505, 2006.
- [72] Paul, P. C., Knoll, A. W., Holzner, F., Despont, M., and Duerig, U. Rapid Turnaround Scanning Probe Nanolithography. *Nanotechnology*, 22(27):275306, 2011.

- [73] Chimmalgi, A., Grigoropoulos, C. P., and Komvopoulos, K. Surface Nanostructuring by nano-/femtosecond Laser-Assisted Scanning Force Microscopy. *Journal of Applied Physics*, 97(10):104319–12, 2005.
- [74] Eigler, D. M. and Schweizer, E. K. Positioning Single Atoms with a Scanning Tunnelling Microscope. *Nature*, 344(6266):524–526, 1990.
- [75] Milner, A. A., Zhang, K., and Prior, Y. Floating Tip Nanolithography. *Nano Letters*, 8(7):2017–2022, 2008.
- [76] Riehn, R., Charas, A., Morgado, J., and Cacialli, F. Near-Field Optical Lithography of a Conjugated Polymer. *Applied Physics Letters*, 82(4):526–528, 2003.
- [77] Arnold, M., Hirschfeld-Warneken, V. C., Lohmuller, T., Heil, P., Blümmel, J., Cavalcanti-Adam, E. A., López-García, M., Walther, P., Kessler, H., Geiger, B., and Spatz, J. P. Induction of Cell Polarization and Migration by a Gradient of Nanoscale Variations in Adhesive Ligand Spacing. *Nano Letters*, 8(7):2063–2069, 2008.
- [78] Spatz, J. P. Nano- and Micropatterning by Organic-Inorganic Templating of Hierarchical Self-Assembled Structures. *Angewandte Chemie International Edition*, 41(18):3359–3362, 2002.
- [79] Zhu, X., Mills, K. L., Peters, P. R., Bahng, J. H., Liu, E. H., Shim, J., Naruse, K., Csete, M. E., Thouless, M. D., and Takayama, S. Fabrication of Reconfigurable Protein Matrices by Cracking. *Nature Materials*, 4(5):403–406, 2005.
- [80] Morgenthaler, S., Lee, S., Zrcher, S., and Spencer, N. D. A Simple, Reproducible Approach to the Preparation of Surface-Chemical Gradients. *Langmuir*, 19(25):10459–10462, 2003.
- [81] Huo, F., Zheng, G., Liao, X., Giam, L. R., Chai, J., Chen, X., Shim, W., and Mirkin, C. A. Beam Pen Lithography. *Nature Nanotechnology*, 5(9):637–640, 2010.
- [82]
- [83] Wu, E. S., Strickler, J. H., Harrell, W. R., and Webb, W. W. Two-Photon Lithography for Microelectronic Application. In *Optical/Laser Microlithography V*, pages 776–782. International Society for Optics and Photonics.
- [84] Ito, T. and Okazaki, S. Pushing the Limits of Lithography. *Nature*, 406(6799):1027–1031, 2000.
- [85] Marder, S. R., Brédas, J.-L., and Perry, J. W. Materials for Multiphoton 3D Microfabrication. *MRS Bulletin*, 32(07):561–565, 2007.
- [86] Maalouf, A., Gadonna, M., and Bosc, D. An Improvement in Standard Photolithography Resolution based on Kirchhoff Diffraction Studies. *Journal of Physics D: Applied Physics*, 42(1):015106, 2009.

- [87] Hulett, J. Deviations from the Arrhenius Equation. *Quarterly Reviews, Chemical Society*, 18(3):227–242, 1964.
- [88] Laidler, K. J. and King, M. C. Development of Transition-State Theory. *The Journal of Physical Chemistry*, 87(15):2657–2664, 1983.
- [89] Laidler, K. J. The Development of the Arrhenius Equation. *Journal of Chemical Education*, 61(6):494, 1984.
- [90] Gardiner, W. C. Temperature Dependence of Bimolecular Gas Reaction Rates. *Accounts of Chemical Research*, 10(9):326–331, 1977.
- [91] Wang, D. *Thermochemical Nanolithography Fabrication and Atomic Force Microscopy Characterization of Functional Nanostructures [electronic resource] / by Debin Wang*. Atlanta, Ga. : Georgia Institute of Technology, 2010., 2010.
- [92] King, W. P. and Goodson, K. E. Thermomechanical Formation of Nanoscale Polymer Indents with a Heated Silicon Tip. *Journal of Heat Transfer*, 129:1600–1604, 2007.
- [93] Lee, J., Beechem, T., Wright, T. L., Nelson, B. A., Graham, S., and King, W. P. Electrical, Thermal, and Mechanical Characterization of Silicon Microcantilever Heaters. *Journal of Microelectromechanical Systems*, 15(6):1644–1655, 2006.
- [94] Chen, G. Ballistic-Diffusive Heat-Conduction Equations. *Physical Review Letters*, 86(11):2297–2300, 2001.
- [95] Nelson, B. A. and King, W. P. Modeling and Simulation of the Interface Temperature Between a Heated Silicon Tip and a Substrate. *Nanoscale and Microscale Thermophysical Engineering*, 12(1):98–115, 2008.
- [96] Cahill, D. G., Ford, W. K., Goodson, K. E., Mahan, G. D., Majumdar, A., Maris, H. J., Merlin, R., and Phillpot, S. R. Nanoscale Thermal Transport. *Journal of Applied Physics*, 93(2):793–818, 2003.
- [97] Duvigneau, J., Schönherr, H., and Vancso, G. J. Nanoscale Thermal AFM of Polymers: Transient Heat Flow Effects. *ACS Nano*, 4(11):6932–6940, 2010.
- [98] Escobar, R. A., Ghai, S. S., Jhon, M. S., and Amon, C. H. Multi-Length and Time Scale Thermal Transport Using the Lattice Boltzmann Method with Application to Electronics Cooling. *International Journal of Heat and Mass Transfer*, 49(12):97–107, 2006.
- [99] King, W. P., Kenny, T. W., Goodson, K. E., Cross, G., Despont, M., Durig, U., Rothuizen, H., Binnig, G. K., and Vettiger, P. Atomic Force Microscope Cantilevers for Combined Thermomechanical Data Writing and Reading. *Applied Physics Letters*, 78(9):1300–1302, 2001.

- [100] Chapuis, P. O., Greffet, J. J., Joulain, K., and Volz, S. Heat Transfer between a Nano-Tip and a Surface. *Nanotechnology*, 17(12):2978, 2006.
- [101] Chui, B. W., Stowe, T. D., Yongho Sungtaek, J., Goodson, K. E., Kenny, T. W., Mamin, H. J., Terris, B. D., Ried, R. P., and Rugar, D. Low-Stiffness Silicon Cantilevers with Integrated Heaters and Piezoresistive Sensors for High-Density AFM Thermomechanical Data Storage. *Journal of Microelectromechanical Systems*, 7(1):69–78, 1998.
- [102] King, W. P. Design Analysis of Heated Atomic Force Microscope Cantilevers for Nanotopography Measurements. *Journal of Micromechanics and Microengineering*, 15(12):2441, 2005.
- [103] Lee, J., Wright, T. L., Abel, M. R., Sunden, E. O., Marchenkov, A., Graham, S., and King, W. P. Thermal Conduction from Microcantilever Heaters in Partial Vacuum. *Journal of Applied Physics*, 101(1):014906–6, 2007.
- [104] Nafday, O. A., Weeks, B. L., King, W. P., and Lee, J. Inducing Nanoscale Morphology Changes of Pentaerythritol Tetranitrate Using a Heated Atomic Force Microscope Cantilever. *Journal of Energetic Materials*, 27(1):1–16, 2008.
- [105] Ravi, T. S., Marcus, R. B., and Liu, D. Oxidation Sharpening of Silicon Tips. *Journal of Vacuum Science & Technology B: Microelectronics and Nanometer Structures*, 9(6):2733–2737, 1991.
- [106] Lee, B., Prater, C. B., and King, W. P. Lorentz Force Actuation of a Heated Atomic Force Microscope Cantilever. *Nanotechnology*, 23(5):055709, 2012.
- [107] Sernelius, B. E. Temperature-Dependent Resistivity of Heavily Doped Silicon and Germanium. *Physical Review B*, 41(5):3060–3068, 1990.
- [108] Chui, B. W., Asheghi, M., Ju, Y., Goodson, K. E., Kenny, T. W., and Mamin, H. J. Intrinsic-Carrier Thermal Runaway in Silicon Microcantilevers. *Microscale Thermophysical Engineering*, 3(3):217–228, 1999.
- [109] Lantz, M. A., Gotsmann, B., Durig, U. T., Vettiger, P., Nakayama, Y., Shimizu, T., and Tokumoto, H. Carbon Nanotube Tips for Thermomechanical Data Storage. *Applied Physics Letters*, 83(6):1266–1268, 2003.
- [110] Underwood, William David, I. *A Thin Film Polymer System for the Patterning of Amines through Thermochemical Nanolithography [electronic resource] / by William David Underwood*. Atlanta, Ga. : Georgia Institute of Technology, 2009., 2009.
- [111] King, W. P., Kenny, T. W., and Goodson, K. E. Comparison of Thermal and Piezoresistive Sensing Approaches for Atomic Force Microscopy Topography Measurements. *Applied Physics Letters*, 85(11):2086–2088, 2004.

- [112] McCafferty, E. and Wightman, J. P. Determination of the Concentration of Surface Hydroxyl Groups on Metal Oxide Films by a Quantitative XPS Method. *Surface and Interface Analysis*, 26(8):549–564, 1998.
- [113] Leggett, G. J., Brewer, N. J., and Chong, K. S. L. Friction Force Microscopy: Towards Quantitative Analysis of Molecular Organisation with Nanometre Spatial Resolution. *Physical Chemistry Chemical Physics*, 7(6):1107–1120, 2005.
- [114] Jares-Erijman, E. A. and Jovin, T. M. FRET Imaging. *Nat Biotech*, 21(11):1387–1395, 2003.
- [115] Stabley, D. R., Jurchenko, C., Marshall, S. S., and Salaita, K. S. Visualizing Mechanical Tension across Membrane Receptors with a Fluorescent Sensor. *Nat Meth*, 9(1):64–67, 2012.
- [116] Waters, J. C. Accuracy and Precision in Quantitative Fluorescence Microscopy. *The Journal of Cell Biology*, 185(7):1135–1148, 2009.
- [117] Doyle, C. D. Kinetic Analysis of Thermogravimetric Data. *Journal of Applied Polymer Science*, 5(15):285–292, 1961.
- [118] Freeman, E. S. and Carroll, B. The Application of Thermoanalytical Techniques to Reaction Kinetics: The Thermogravimetric Evaluation of the Kinetics of the Decomposition of Calcium Oxalate Monohydrate. *The Journal of Physical Chemistry*, 62(4):394–397, 1958.
- [119] Zsako, J. Kinetic Analysis of Thermogravimetric Data. *The Journal of Physical Chemistry*, 72(7):2406–2411, 1968.
- [120] Kim, S., Mundra, M. K., Roth, C. B., and Torkelson, J. M. Suppression of the Tg-Nanoconfinement Effect in Thin Poly(vinyl acetate) Films by Sorbed Water. *Macromolecules*, 43(11):5158–5161, 2010.
- [121] Kim, S., Roth, C. B., and Torkelson, J. M. Effect of Nanoscale Confinement on the Glass Transition Temperature of Free-Standing Polymer Films: Novel, Self-Referencing Fluorescence Method. *Journal of Polymer Science Part B: Polymer Physics*, 46(24):2754–2764, 2008.
- [122] Riedo, E., Lévy, F., and Brune, H. Kinetics of Capillary Condensation in Nanoscopic Sliding Friction. *Physical Review Letters*, 88(18):185505, 2002.
- [123] Shaw, T., Trolier-McKinstry, S., and McIntyre, P. The Properties of Ferroelectric Films at Small Dimensions. *Annual review of materials science*, 30(1):263–298, 2000.
- [124] Li, S., Eastman, J. A., Li, Z., Foster, C. M., Newnham, R. E., and Cross, L. E. Size Effects in Nanostructured Ferroelectrics. *Physics Letters A*, 212(6):341–346, 1996.

- [125] Burroughes, J. H., Bradley, D. D. C., Brown, A. R., Marks, R. N., Mackay, K., Friend, R. H., Burns, P. L., and Holmes, A. B. Light-Emitting Diodes Based on Conjugated Polymers. *Nature*, 347(6293):539–541, 1990.
- [126] Olver, F. W. J. Uniform, Exponentially Improved, Asymptotic Expansions for the Generalized Exponential Integral. *SIAM Journal on Mathematical Analysis*, 22(5):1460–1474, 1991.
- [127] Senum, G. I. and Yang, R. T. Rational Approximations of the Integral of the Arrhenius Function. *Journal of thermal analysis*, 11(3):445–447, 1977.
- [128] Cacialli, F., Riehn, R., Downes, A., Latini, G., Charas, A., and Morgado, J. Fabrication of Conjugated Polymers Nanostructures via Direct Near-Field Optical Lithography. *Ultramicroscopy*, 100(34):449–455, 2004.
- [129] Pelletier, M. J. Quantitative Analysis Using Raman Spectrometry. *Applied Spectroscopy*, 57(1):20A–42A, 2003.
- [130] Rickard, D., Giordani, S., Blau, W. J., and Coleman, J. N. Quantifying the Contributions of Inner-Filter, Re-Absorption and Aggregation Effects in the Photoluminescence of High-Concentration Conjugated Polymer Solutions. *Journal of Luminescence*, 128(1):31–40, 2008.
- [131] Schermelleh, L., Heintzmann, R., and Leonhardt, H. A Guide to Super-Resolution Fluorescence Microscopy. *The Journal of Cell Biology*, 190(2):165–175, 2010.
- [132] Gell, C., Berndt, M., Enderlein, J., and Diez, S. TIRF Microscopy Evanescent Field Calibration Using Tilted Fluorescent Microtubules. *Journal of Microscopy*, 234(1):38–46, 2009.
- [133] Wéry, J., Dulieu, B., Baïtoul, M., Paniez, P., Froyer, G., and Lefrant, S. Thermal Conversion of PPV Precursor: Characterization at Different Stages of the Process. *Synthetic Metals*, 101(13):194–195, 1999.
- [134] Fang, S. J., Haplepete, S., Chen, W., Helms, C. R., and Edwards, H. Analyzing Atomic Force Microscopy Images Using Spectral Methods. *Journal of Applied Physics*, 82(12):5891–5898, 1997.
- [135] Li, G., Xi, N., Yu, M., and Fung, W. K. 3D Nanomanipulation Using Atomic Force Microscopy. In *Robotics and Automation, 2003. Proceedings. ICRA '03. IEEE International Conference on*, volume 3, pages 3642–3647 vol.3.
- [136] Huang, B., Bates, M., and Zhuang, X. Super Resolution Fluorescence Microscopy. *Annual review of biochemistry*, 78:993, 2009.
- [137] Hell, S. Increasing the Resolution of Far-Field Fluorescence Light Microscopy by Point-Spread-Function Engineering. *Topics in fluorescence spectroscopy*, pages 361–426, 2002.

- [138] Glassbrenner, C. J. and Slack, G. A. Thermal Conductivity of Silicon and Germanium from 3 K to the Melting Point. *Physical Review*, 134(4A):A1058–A1069, 1964.
- [139] Tran, H., Killops, K. L., and Campos, L. M. Advancements and Challenges of Patterning Biomolecules with sub-50 nm Features. *Soft Matter*, 9(29):6578–6586, 2013.
- [140] Minne, S. C., Yaralioglu, G., Manalis, S. R., Adams, J. D., Zesch, J., Atalar, A., and Quate, C. F. Automated Parallel High-Speed Atomic Force Microscopy. *Applied Physics Letters*, 72(18):2340–2342, 1998.
- [141] Barrettino, D., Hafizovic, S., Volden, T., Sedivy, J., Kirstein, K. U., and Hierlemann, A. CMOS Monolithic Mechatronic Microsystem for Surface Imaging and Force Response Studies. *Solid-State Circuits, IEEE Journal of*, 40(4):951–959, 2005.
- [142] Sulchek, T., Grow, R. J., Yaralioglu, G. G., Minne, S. C., Quate, C. F., Manalis, S. R., Kiraz, A., Aydine, A., and Atalar, A. Parallel Atomic Force Microscopy with Optical Interferometric Detection. *Applied Physics Letters*, 78(12):1787–1789, 2001.
- [143] Hafizovic, S., Barrettino, D., Volden, T., Sedivy, J., Kirstein, K.-U., Brand, O., and Hierlemann, A. Single-Chip Mechatronic Microsystem for Surface Imaging and Force Response Studies. *Proceedings of the National Academy of Sciences of the United States of America*, 101(49):17011–17015, 2004.
- [144] Minne, S. C., Adams, J. D., Yaralioglu, G., Manalis, S. R., Atalar, A., and Quate, C. F. Centimeter Scale Atomic Force Microscope Imaging and Lithography. *Applied Physics Letters*, 73(12):1742–1744, 1998.
- [145] Bullen, D., Xuefeng, W., Zou, J., Seunghun, H., Chung, S.-W., Ryu, K., Zhifang, F., Mirkin, C., and Chang, L. Micromachined Arrayed Dip Pen Nanolithography Probes for sub-100 nm Direct Chemistry Patterning. In *Micro Electro Mechanical Systems, 2003. MEMS-03 Kyoto. IEEE The Sixteenth Annual International Conference on*, pages 4–7.
- [146] Kim, H. J., Dai, Z., and King, W. P. Thermal Crosstalk in Heated Microcantilever Arrays. *Journal of Micromechanics and Microengineering*, 23(2):025001, 2013.
- [147] King, W. P., Kenny, T. W., Goodson, K. E., Cross, G. L. W., Despont, M., Durig, U. T., Rothuizen, H., Binnig, G., and Vettiger, P. Design of Atomic Force Microscope Cantilevers for Combined Thermomechanical Writing and Thermal Reading in Array Operation. *Microelectromechanical Systems, Journal of*, 11(6):765–774, 2002.

- [148] Cappella, B. and Dietler, G. Force-Distance Curves by Atomic Force Microscopy. *Surface Science Reports*, 34(13):1–104, 1999.
- [149] Kovalev, A., Shulha, H., Lemieux, M., Myshkin, N., and Tsukruk, V. V. Nanomechanical Probing of Layered Nanoscale Polymer Films With Atomic Force Microscopy. *Journal of Materials Research*, 19(03):716–728, 2004.
- [150] Somnath, S. and King, W. P. Heated Atomic Force Cantilever Closed Loop Temperature Control and Application to High Speed Nanotopography Imaging. *Sensors and Actuators A: Physical*, 192(0):27–33, 2013.
- [151] Paul, P., Knoll, A. W., Holzner, F., and Duerig, U. Field Stitching in Thermal Probe Lithography by Means of Surface Roughness Correlation. *Nanotechnology*, 23(38):385307, 2012.
- [152] Holzner, F., Kuemin, C., Paul, P., Hedrick, J. L., Wolf, H., Spencer, N. D., Duerig, U., and Knoll, A. W. Directed Placement of Gold Nanorods Using a Removable Template for Guided Assembly. *Nano Letters*, 11(9):3957–3962, 2011.
- [153] Fryer, D. S., Nealey, P. F., and de Pablo, J. J. Thermal Probe Measurements of the Glass Transition Temperature for Ultrathin Polymer Films as a Function of Thickness. *Macromolecules*, 33(17):6439–6447, 2000.
- [154] Lee, J. and King, W. P. Liquid Operation of Silicon Microcantilever Heaters. *Sensors Journal, IEEE*, 8(11):1805–1806, 2008.
- [155] Zhang, K., Fu, Q., Pan, N., Yu, X., Liu, J., Luo, Y., Wang, X., Yang, J., and Hou, J. Direct Writing of Electronic Devices on Graphene Oxide by Catalytic Scanning Probe Lithography. *Nat Commun*, 3, 2012.
- [156] Liu, M., Amro, N. A., and Liu, G. Nanografting for Surface Physical Chemistry. *Annu. Rev. Phys. Chem.*, 59:367–386, 2008.
- [157] Rosa, L. G. and Liang, J. Atomic Force Microscope Nanolithography: Dip-Pen, Nanoshaving, Nanografting, Tapping Mode, Electrochemical and Thermal Nanolithography. *Journal of Physics: Condensed Matter*, 21(48):483001, 2009.
- [158] Suda, H. and Yamada, S. Force Measurements for the Movement of a Water Drop on a Surface with a Surface Tension Gradient. *Langmuir*, 19(3):529–531, 2002.
- [159] Smith, J. T., Tomfohr, J. K., Wells, M. C., Beebe, T. P., Kepler, T. B., and Reichert, W. M. Measurement of Cell Migration on Surface-Bound Fibronectin Gradients. *Langmuir*, 20(19):8279–8286, 2004.
- [160] Smith, J. T., Elkin, J. T., and Reichert, W. M. Directed Cell Migration on Fibronectin Gradients: Effect of Gradient Slope. *Experimental Cell Research*, 312(13):2424–2432, 2006.

- [161] Wu, T., Efimenko, K., and Genzer, J. Combinatorial Study of the Mushroom-to-Brush Crossover in Surface Anchored Polyacrylamide. *Journal of the American Chemical Society*, 124(32):9394–9395, 2002.
- [162] Moh, L. C. H., Losego, M. D., and Braun, P. V. Solvent Quality Effects on Scaling Behavior of Poly(methyl methacrylate) Brushes in the Moderate- and High-Density Regimes. *Langmuir*, 27(7):3698–3702, 2011.
- [163] Vlasov, Y. A., Bo, X.-Z., Sturm, J. C., and Norris, D. J. On-Chip Natural Assembly of Silicon Photonic Bandgap Crystals. *Nature*, 414(6861):289–293, 2001.
- [164] Lee, I., Zheng, H., Rubner, M. F., and Hammond, P. T. Controlled Cluster Size in Patterned Particle Arrays via Directed Adsorption on Confined Surfaces. *Advanced Materials*, 14(8):572–577, 2002.
- [165] Dziomkina, N. V. and Vancso, G. J. Colloidal Crystal Assembly on Topologically Patterned Templates. *Soft Matter*, 1(4):265–279, 2005.
- [166] Varghese, B., Cheong, F. C., Sindhu, S., Yu, T., Lim, C. T., Valiyaveetil, S., and Sow, C. H. Size Selective Assembly of Colloidal Particles on a Template by Directed Self-Assembly Technique. *Langmuir*, 22(19):8248–8252, 2006.
- [167] Zhang, C., Macfarlane, R. J., Young, K. L., Choi, C. H. J., Hao, L., Auyeung, E., Liu, G., Zhou, X., and Mirkin, C. A. A General Approach to DNA-Programmable Atom Equivalents. *Nat Mater*, 12(8):741–746, 2013.
- [168] Wang, Y., Wang, Y., Breed, D. R., Manoharan, V. N., Feng, L., Hollingsworth, A. D., Weck, M., and Pine, D. J. Colloids with Valence and Specific Directional Bonding. *Nature*, 491(7422):51–55, 2012.
- [169] Schoch, R. B., Han, J., and Renaud, P. Transport Phenomena in Nanofluidics. *Reviews of Modern Physics*, 80(3):839–883, 2008.
- [170] Abgrall, P. and Nguyen, N. T. Nanofluidic Devices and Their Applications. *Analytical Chemistry*, 80(7):2326–2341, 2008.
- [171] Weber, H. J., Harris, F. E., and Arfken, G. B. *Essential Mathematical Methods for Physicists, ISE*. Access Online via Elsevier, 2003.

VITA

Keith M. Carroll grew up in the greater Philadelphia area. He attended Loyola University Chicago and graduated Summa Cum Laude in 2007. He then attended Georgia Institute of Technology; during his tenure at Georgia Institute of Technology, he was awarded three fellowships: the Presidential, COPE, and the Bonnie B. and Charles K Rice Jr. Fellowship. In 2011, he married the love of his life, Jessica, whom he met at Loyola. Many have agreed this was his best decision.